Mehmet Furkan Baltacıoğlu

Ph.D. Thesis

AGU 2024

THE EFFECT OF HYDROGEN ON THE MECHANICAL PROPERTIES OF MATERIALS

Ph.D. THESIS
SUBMITTED TO THE DEPARTMENT OF MATERIALS SCIENCE
AND MECHANICAL ENGINEERING
AND THE GRADUATE SCHOOL OF ENGINEERING AND SCIENCE
OF ABDULLAH GUL UNIVERSITY
IN PARTIAL FULFILLMENT OF THE REQUIREMENTS
FOR THE DEGREE OF
PHD

By
Mehmet Furkan Baltacıoğlu
December 2024

THE EFFECT OF HYDROGEN ON THE MECHANICAL PROPERTIES OF MATERIALS

A THESIS
SUBMITTED TO THE DEPARTMENT OF MATERIALS SCIENCE AND MECHANICAL ENGINEERING
AND THE GRADUATE SCHOOL OF ENGINEERING AND SCIENCE OF ABDULLAH GUL UNIVERSITY
IN PARTIAL FULFILLMENT OF THE REQUIREMENTS
FOR THE DEGREE OF
PHD

By
Mehmet Furkan Baltacıoğlu
December 2024

SCIENTIFIC ETHICS COMPLIANCE

I hereby declare that all information in this document has been obtained in accordance with academic rules and ethical conduct. I also declare that, as required by these rules and conduct, I have fully cited and referenced all materials and results that are not original to this work.

Name-Surname: Mehmet Furkan Baltacıoğlu
Signature:

REGULATORY COMPLIANCE

Ph.D. thesis titled The Effect of Hydrogen on the Mechanical Properties of Materials has been prepared in accordance with the Thesis Writing Guidelines of the Abdullah Gül University, Graduate School of Engineering & Science.

Prepared By	Advisor
Mehmet Furkan Baltacıoğlu	Assoc. Prof. Dr. Burak Bal
Signature	Signature

Head of the Materials Science and Mechanical Engineering Program
Assist. Prof. Dr. Zeliha Soran Erdem
Signature

ACCEPTANCE AND APPROVAL

Ph.D. thesis titled The Effect of Hydrogen on the Mechanical Properties of Materials and prepared by Mehmet Furkan Baltacıoğlu has been accepted by the jury in the Materials Science and Mechanical Engineering Graduate Program at Abdullah Gül University, Graduate School of Engineering & Science.

18/12/2024

(Thesis Defense Exam Date)

JURY:

Advisor: Assoc. Prof. Dr. Burak Bal

Member: Assoc. Prof. Dr. İsmail Alper İşoğlu

Member: Assoc. Prof. Dr. Murat Aydın

Member: Assoc. Prof. Dr. Umut Çalışkan

Member: Assist. Prof. Dr. Çağatay Yılmaz

APPROVAL:

The acceptance of this Ph.D. thesis has been approved by the decision of the Abdullah Gül University, Graduate School of Engineering & Science, Executive Board dated ….. /….. / …….. and numbered ……..……. .

…….. /…….. / ……..

(Date)

Graduate School Dean
Prof. İrfan ALAN

ABSTRACT

THE EFFECT OF HYDROGEN ON THE MECHANICAL PROPERTIES OF MATERIALS

Mehmet Furkan Baltacıoğlu
Ph.D. in Materials Science and Mechanical Engineering
Advisor: Assoc. Prof. Dr. Burak Bal
December 2024

This study examines the hydrogen effect on the mechanical properties of aluminum alloys and body centered cubic iron under different loading conditions and strain rates. First, the hydrogen susceptibility of Al 7075 was evaluated under quasi-static and medium strain rates using tensile tests. According to the results, at greater strain rates, hydrogen embrittlement is more dominant compared to quasi-static strain rates. The hydrogen embrittlement mechanism is shifting from hydrogen-enhanced localized plasticity (HELP) at slower rates to a coexistence of HELP and hydrogen-enhanced decohesion (HEDE) at medium rates. In a parallel investigation, the hydrogen susceptibility of Al 5083 was evaluated under ballistic tests through experimental and numerical methods. According to the results, the dominance of HEDE is increasing on HELP at greater deformation rates. Finite element methods were utilized and combined with the Johnson-Cook model, and this process confirmed the experimental outcome also this step offered a predictive model for hydrogen-charged conditions in ballistic applications. Lastly, using molecular dynamics simulations, edge dislocation mobility in body centered iron was evaluated in a wide range of temperature, hydrogen concentration and stress levels to investigate the hydrogen susceptibility. Resulting from the study, phenomenological mobility laws were offered. Collectively, these studies advance the understanding of the hydrogen effect on metals under varying mechanical conditions, providing crucial insights for engineering applications where hydrogen exposure is a factor.

Keywords: Hydrogen Embrittlement, Aluminum Alloys, Iron, Mechanical Testing, Molecular Dynamics.

ÖZET

MALZEMELERİN MEKANİK ÖZELLİKLERİ ÜZERİNDE HİDROJENİN ETKİSİ

Mehmet Furkan Baltacıoğlu
Malzeme Bilimi ve Makine Mühendisliği Doktora Programı
Tez Danışmanı: Doç. Dr. Burak Bal
Aralık-2024

Bu çalışmada, hidrojenin farklı mekanik yükleme koşulları ve gerinim hızları altında alüminyum alaşımları ve hacim merkezli kübik (HMK) demir üzerindeki etkisini incelemektedir. İlk olarak, Al 7075'in hidrojen duyarlılığı, yavaş ve orta gerinim hızlarında yapılan çekme testleri ile değerlendirilmiştir. Sonuçlara göre, daha yüksek gerinim hızlarında hidrojen gevrekliği, yavaş gerinim hızlarına göre daha baskındır. Hidrojen gevrekliği mekanizması, düşük hızlarda hidrojenle desteklenen lokalize plastisite (HELP) iken, orta hızlarda HELP ve hidrojenle desteklenen ayrışmanın (HEDE) bir arada bulunması yönünde değişiklik göstermektedir. İkinci çalışmada, Al 5083'ün hidrojen duyarlılığı, balistik testler altında deneysel ve sayısal yöntemler kullanılarak incelenmiştir. Sonuçlara göre, artan deformasyon hızlarında HEDE'nin HELP üzerindeki baskınlığı artmaktadır. Sonlu elemanlar yöntemi, Johnson-Cook modeli ile birleştirilerek deneysel sonuçları doğrulamış ve balistik uygulamalarda hidrojenle yüklenmiş koşullar için öngörücü bir model sunmuştur. Son olarak, moleküler dinamik simülasyonları kullanılarak, hacim merkezli demirdeki kenar dislokasyon hareketliliği, geniş bir sıcaklık, hidrojen konsantrasyonu ve gerilme seviyesi aralığında değerlendirilmiş ve hidrojen duyarlılığı araştırılmıştır. Çalışmadan elde edilen bulgular sonucunda fenomenolojik hareketlilik yasaları önerilmiştir. Bu çalışmalar, hidrojenin metaller üzerindeki etkisini değişen mekanik koşullar altında anlamaya katkıda bulunarak, hidrojen maruziyetinin söz konusu olduğu mühendislik uygulamaları için önemli çıktılar sunmaktadır.

Anahtar kelimeler: Hidrojen Gevrekliği, Aluminyum Alaşımları, Demir, Mekanik Testler, Moleküler Dinamik.

Acknowledgements

I would like to express my heartfelt gratitude to my academic advisor, Assoc. Prof. Dr. Burak Bal, for his unwavering support, guidance, and generous sharing of knowledge throughout my journey, regardless of the time or circumstances. He has not only motivated me academically but also made me feel a valued member of a significant academic network. Working alongside him has been a truly enjoyable experience, and his contributions to my development are invaluable.

I also extend my sincere thanks to my doctoral monitoring committee members, Assoc. Prof. Dr. Alper İşoğlu and Assist. Prof. Dr. Çağatay Yılmaz, for their constant motivation and significant contributions to my work, they always motivated me and they are members of my thesis defense jury. I am grateful as well to Prof. Dr. J. Christian Schoen, Assoc. Prof. Dr. Murat Aydın, Assist. Prof. Dr. Mazofori Farzin, Dr. Barış Çetin for our collaborative efforts, continuous support, encouragement, and genuine assistance, and to Mehmet Fazıl Kapçı, with whom I had the pleasure of working closely. Also, I extend my appreciation to Assoc. Prof. Dr. Umut Çalışkan and Assoc. Prof. Dr. Murat Aydın for being jury members of my thesis defense.

I would like acknowledge the support by TUBITAK and AGU BAP, whom I am sincerely grateful to fund my study. This study was supported by TUBITAK Grant Number: 122M754 and AGU BAP Project No: 174.

Finally, I would like to thank my family—my mother, father, and sister—for their invaluable support, encouragement, and motivation throughout this process. I love you all.

TABLE OF CONTENTS

LIST OF FIGURES

LIST OF TABLES

LIST OF ABBREVIATIONS

AIDE	Adsorption-Induced Dislocation Emission
BCC	Body Centered Cubic
DC	Direct Current
DHF	Decohesive Hydrogen Fracture
DSA	Dynamic Strain Aging
DXA	Dislocation Extraction Algorithm
EAM	Embedded Atom Method
EDX	X-Ray Diffraction
FCC	Face Centered Cubic
FEA	Finite Element Analysis
G	Glissile Dislocation
GA	Genetic Algorithm
HAM	Hydrogen Changed Micro-Fracture Mode
HDMC	Hydrogen Assisted Micro Void Coalescence
HE	Hydrogen Embrittlement
HEDE	Hydrogen Enhanced Decohesion Mechanism
HELP	Hydrogen Enhanced Local Plasticity
HEMP	Hydrogen Enhanced Macroscopic Ductility
J-C	Johnson-Cook
KMC	Kinetic Monte Carlo
MD	Molecular Dynamics
MF	Mixed Fracture
MVC	Microvoid Coalescence
NVE	Number of Atoms, Volume and Energy Constant
PPS	Periodic-Periodic-Shrink
S	Sessile Dislocation
SEM	Scanning Electron Microscopy
UTS	Ultimate Tensile Strength
XRD	X-Ray Spectroscopy

To my family

Chapter 1

Introduction

In recent years, there has been a significant increase in hydrogen production and demand for hydrogen energy [1]. Consequently, the importance of hydrogen storage and transportation systems has grown. Due to its status as the smallest atom, hydrogen diffuses very easily. This poses risks not only for transportation and storage systems but also during manufacturing processes and usage, where hydrogen can diffuse into materials [2,3]. As a result, the effects of hydrogen can be significant across various applications. When hydrogen diffuses into metallic materials, it can affect their ductility, fatigue life, strength and this phenomenon known in the literature as hydrogen embrittlement [2,4–7]. Decreased ductility, fatigue life and strength can lead to unexpected failures, making the study of this phenomenon crucial across multiple scales, environments, time scales, materials, and deformation conditions [3,8–11].

Various HE mechanisms have been proposed in the literature [4]. Some of these are hydrogen enhanced decohesion mechanism (HEDE), hydrogen enhanced local plasticity (HELP), adsorption-induced dislocation emission (AIDE), hydrogen enhanced macroscopic ductility (HEMP), hydrogen changed micro-fracture mode (HAM), decohesive hydrogen fracture (DHF), mixed fracture (MF), hydrogen assisted micro void coalescence (HDMC) [4]. HEDE mechanism explains hydrogen-induced fracture by describing how hydrogen atoms decrease the cohesive strength at a crack tip, leading to decohesion and fracture at reduced stress levels due to the diffusion of hydrogen and the weakening of interatomic bonds [4]. The HELP mechanism explains how the presence of hydrogen near a crack tip increases dislocation mobility, causing local plastic deformation at low stress levels and being influenced by hydrogen concentration, microstructure, and stress intensity [4]. AIDE mechanism integrates HELP and HEDE mechanisms, where

hydrogen atoms accumulate near high stress concentration regions like defects [4]. In this mechanism, HEDE weakens the interatomic bonding and HELP introduces microvoids by emitting dislocations near crack tip and causing crack growth [4]. HEMP mechanism describes how high concentrations of hydrogen in steel reduce its yield strength through hydrogen diffusion and solid solution softening [4]. According to HAM, the fracture changes from ductile to brittle due to shear fracture resulting from high hydrogen concentration at regions with dislocations [4]. The DHF mechanism highlights that fracture begins in a ductile mode, but hydrogen or the reduced cohesion caused by hydrogen transitions the fracture to a brittle mode [4]. According to MF, fracture surfaces often show a mixed fracture mechanism, where both brittle fisheye features and ductile microvoid coalescence coexist, indicating a combination of these fracture modes [4]. HDMC involves ductile MVC mechanisms affected by hydrogen, leading to void nucleation, growth, and coalescence, resulting in zig-zag crack propagation, shear dimples, and some brittle intergranular fractures [4]. Many different mechanisms for HE are discussed in literature, but the actual mechanism of HE is not yet understood [3,10,11].

To better understanding of HE, in the second chapter, hydrogen embrittlement in Al 7075 was studied under quasi-static and medium strain rates. Hence, strain rate sensitivity of material under hydrogen effect was investigated. In the third chapter, the effect of hydrogen on the ballistic performance of Al 5083 H131 was investigated through experiments and simulations. Finite element analysis, integrated with the Johnson-Cook model, aligned well with experimental findings, providing a predictive model for hydrogen-charged conditions in ballistic applications. In the fourth chapter, molecular dynamics simulations were used to examine hydrogen effect on the mobility of edge dislocations in BCC iron, showing that hydrogen significantly slows dislocation movement due to pinning. The study proposes mobility laws that account for stress, temperature, and hydrogen concentration. Following these three studies, the hydrogen embrittlement phenomenon has been comprehensively investigated both experimentally and computationally. By examining various deformation rates, loading conditions, and materials, this research provides a more detailed understanding of hydrogen embrittlement across different scenarios, offering critical insights for its effects in engineering applications.

Chapter 2

The Effect of Strain Rate on the Hydrogen Embrittlement Susceptibility of Aluminum 7075 [3]*

*This study has been published on Journal of Engineering Materials and Technology and the content has been reprinted with permission.

Abstract

The effects of changing strain rate regime from quasi-static to medium on hydrogen susceptibility of aluminum (Al) 7075 were investigated by means of tensile tests. Strain rates were selected as 10^{-3} s^{-1} and 1 s^{-1} and tensile tests were conducted on both hydrogen uncharged and hydrogen charged specimens at room temperature. Electrochemical hydrogen charging method was utilized and diffusion length of hydrogen inside Al 7075 was modeled. Material characterizations were carried out by X-ray diffraction (XRD) and energy dispersive X-Ray spectroscopy (EDX) and microstructural observations of hydrogen uncharged and hydrogen charged specimens were performed by scanning electron microscope (SEM). As opposed to previous studies hydrogen embrittlement was more pronounced at high strain rate case. Moreover, hydrogen enhanced localized plasticity (HELP) was the more dominant hydrogen embrittlement mechanism at slower strain rate, but coexistence of hydrogen enhanced localized plasticity and hydrogen enhanced decohesion was observed at a medium strain rate. Overall, the current findings shed light on the complicated hydrogen embrittlement behavior of Al 7075 and constitute an efficient guideline for the usage of Al 7075 that can be subject to different strain rate loadings in service.

2.1 Introduction

Aluminum (Al) alloys can be used in several sectors including transportation, electrical, biomedical, aerospace and military [12]. As a series of Al alloy, Al 7000 series has satisfying machinability, good corrosion resistance, reasonable ductility, low weight and high strength character [13–16]. Al 7075 is a subcategory of the Al 7000 series and its primary alloying element is zinc [17]. Al 7075 also contains Cu, Mn, Mg, Fe, Cr, Ti, Si and Al as remaining [18]. Due to its high mechanical performance, Al 7075 can be used in hydrogen related infrastructures, such as hydrogen storage [19,20]. At room temperature, Al has faced-centered cubic (FCC) crystal structure [14]. The FCC structure of the material makes the diffusion rate lower compared to the body-centered cubic structure and hence, Al 7075 is a good candidate material to be used in hydrogen effected usage areas [9]. In particular, the hydrogen diffusivity of Al 7075 is 4.4 x 10^{-12} m^2/s at 318 K [17]. However, it was also reported that, Al 7075 has hydrogen embrittlement (HE)

susceptibility [9,17]. Hence, the HE character of the material needs to be tested under different scenarios to analyze the material in detail.

Mechanical properties of the material, ductility, tensile strength and fatigue strength are highly affected by the presence of hydrogen in material during deformation [2,4–6]. This phenomenon is called as HE [2,21]. To talk about HE, hydrogen should be present in the material. There are several ways that hydrogen can diffuse into the material. The hydrogen can diffuse into the material during casting, manufacturing operations, cathodic charging, and in-usage [2]. There are several proposed HE mechanisms in literature, including HEDE (hydrogen enhanced decohesion mechanism), HELP (hydrogen enhanced localized plasticity), AIDE (adsorption-induced dislocation emission), HEMP (hydrogen enhanced macroscopic ductility), HAM (hydrogen changed micro-fracture mode), DHF (decohesive hydrogen fracture), MF (Mixed fracture), HDMC (hydrogen assisted micro void coalescence), to understand the nature of HE [4]. Also, the synergistic action of HE mechanisms, HELP+HEDE, HELP dominated and HEDE dominated, are explained in literature [9,22–26]. HEDE mechanism can be present as the hydrogen content is locally high enough and in this type of HE mechanism, internal attraction forces are lowered with the presence of hydrogen [22]. In particular, according to HELP mechanism, hydrogen shields the stress field of dislocations and enhances dislocation mobility, whereas HEDE states that hydrogen reduces the binding energy of atoms and promotes embrittlement [22,23,27–29] and the synergistic action of HELP and HEDE was reported before for Al 7xxx series [9,23]. The dominance of each HE mechanism during deformation depends on several parameters, such as hydrogen content, charging methods, microstructure and loading scenarios [9,22–26]. However, the exact mechanism of HE is not clear yet [8,9].

The effect of hydrogen on the tensile properties, fatigue life, crack growth characteristic, and impact response of Al 7075 was investigated before as well as the humidity, pre-staining and charging time susceptibilities of Al 7075 to HE [19,30–36]. In particular, most of the studies were conducted at slow strain rate as it allows sufficient time for hydrogen-dislocation interactions, but there are also other studies that were carried out at moderate and high strain rates at different temperatures [9]. Corresponding microstructural observations revealed the effects of hydrogen on the microstructure. Earlier studies showed that the mechanical properties of Al 7075 are sensitive to strain rate, known as strain rate sensitivity [37]. Therefore, HE behavior of Al 7075 at different strain rates should also be clarified since during operation Al 7075 can be subject to

different strain rates. However, despite the many works on the HE of Al alloys, there are only a few of studies focusing on the effects of strain rate on HE susceptibility of Al 7075 alloy [38]. In this study, strain rate range is limited to quasi-static strain rate ($1x10^{-4}$ s^{-1} to $1x10^{-6}$ s^{-1}). However, as it was discussed before, Al 7075 can be subject to medium strain rate loadings and hydrogen affects the mechanical response of Al 7075 at medium strain rates, too [9]. On the contrary, to the authors' knowledge, there is no study that reveals the effect of strain rate sensitivity on HE susceptibility of Al 7075 at large strain rate range, including quasi-static and medium strain rate ranges.

In this study, mechanical character of Al 7075 was investigated under two different strain rates, 1 s^{-1} and 10^{-3} s^{-1} by means of tensile tests. Materials were charged with hydrogen before each test. Material characterization was carried out using X-ray spectroscopy (EDX) and X-ray diffraction (XRD) and fracture surfaces of the specimens were investigated by scanning electron microscope (SEM). The effect of hydrogen on mechanical response of Al 7075 was observed at different strain rates. In addition, Kocks-Mecking curves were constructed to explore the effect of hydrogen on the work hardening rate in different strain rate regimes. Finally, a 1-D diffusion model was used concurrently with the SEM data aiming to compute the hydrogen diffusion constants (D and D_0) of Al 7075. To be able to discard any possible effects of hydrogen transportation during the plastic deformation process, the diffusion model is constructed for the tensile test data of 1 s^{-1}. In this view, hydrogen induced dimensions were calculated with proper image processing approach as designated in the related sections. The computed diffusion constants, which are major parameters in hydrogen diffusion coupled finite element analysis models, are quite in line with the existing literature data.

2.2 Experimental Procedure

2.3 Material

2.3.1 As received material

The chemical composition of the investigated material, Aluminum 7075-T651, is presented in Table 2.1. T651 heat treatment process involves solution heat treatment, stress relief by stretching, air cooling and artificial aging at 394K for 24h [39]. Zeiss Gemini 300 which is equipped with EDX module was used to make the EDX analysis

(Table 2.1). The XRD measurements were carried out with a Bruker D8Discover setup, operating at 40 kV and 40 mA using copper anode Cu-Kα source (wavelength = 1.5406 Å). Figure 2.1a shows the XRD data of the as-delivered, H-uncharged+undeformed, and H-Charged+deformed specimens. XRD data were collected over a range of 0 to 90 deg in 2θ and no strong texture was observed. According to XRD results, neither hydrogen charging nor deformation changed any crystallographic plane. The initial microstructure was also observed using SEM equipped with an EDX and the corresponding results are given in Figure 2.1.

Table 2.1 The content of the material i.e., EDX result of the material

Zn	Mg	Cu	Ti	Si	Al
4.83	3.21	1.89	0.65	0.39	Balance

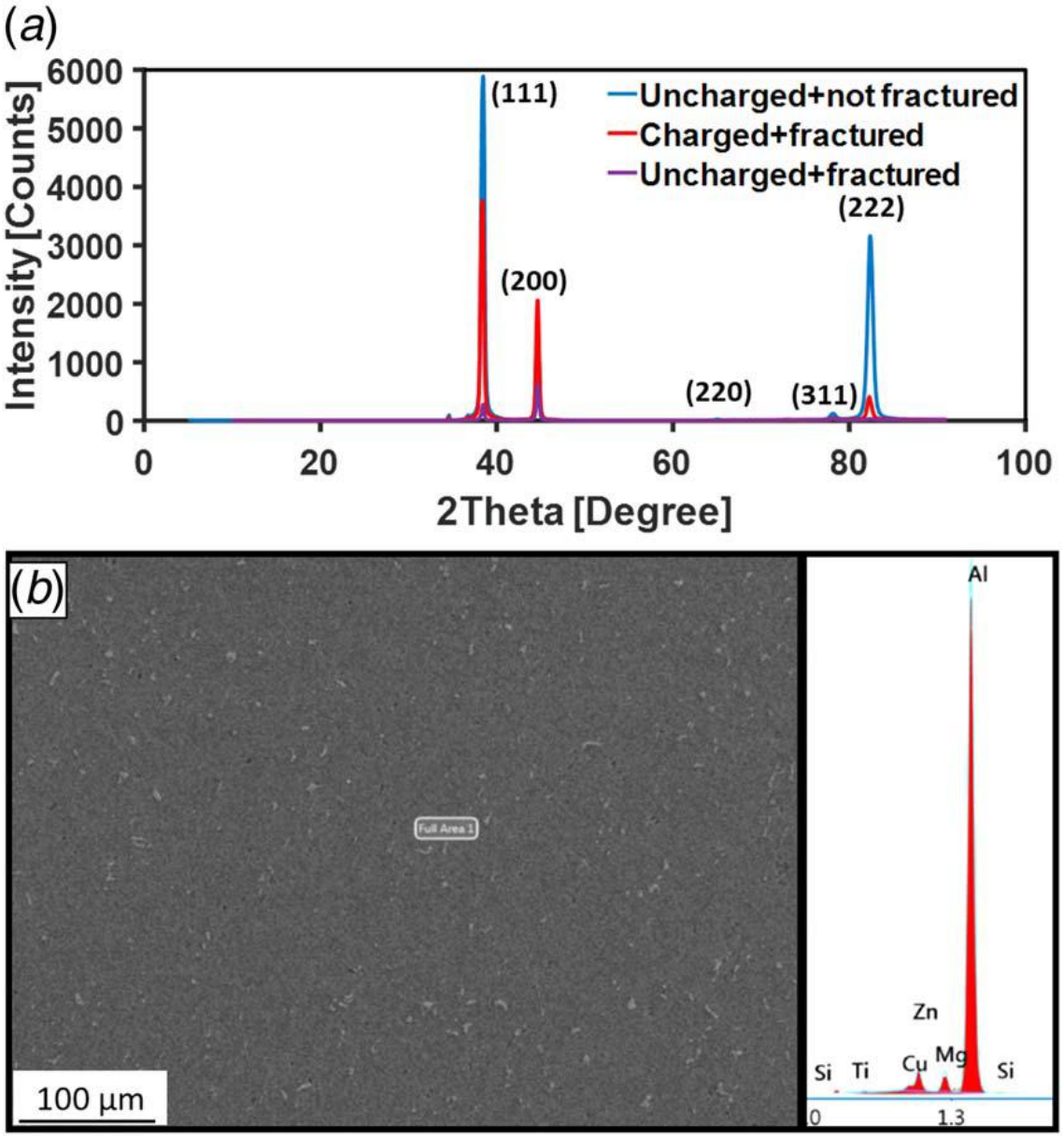

Figure 2.1 XRD and EDX characterization of the material. a) presents the XRD result of material in three different conditions. b) shows the area where EDX analysis was performed and the corresponding EDX analysis of the as-received material.

2.3.2 Hydrogen charging, tensile tests, and associated microstructural characterization

Cylindrical tensile test specimens with a diameter of 16 mm and gauge length of 66 mm were prepared by electro-discharge machining. The technical drawing of the specimens is presented in Figure 2.2 Prior to hydrogen charging, the test specimens were mechanically grinded and chemically polished using standard grinding and polishing equipment to remove all the stress concentration sources as well as micro cracks, and then etched. Specimens were charged with hydrogen by using an electrochemical process

before tensile testing. For this purpose, %3 NaCl and 3g/l ammonium thiocyanate (NH_4SCN) aqueous solution at room temperature was used [40]. This solution was changed every 12 h and the specimen surfaces were polished to remove contamination layer during the charging process. During the process, the test specimens are plugged into cathode. A platinum (Pt) wire having nearly 3 mm^2 surface area was used as the auxiliary (counter) electrode. The specimens were charged in the aqueous solution for 24h at a current density of 50A/m^2. DC power supply was used to charge materials with hydrogen. The power supply was operated in constant current mode, in this manner, the same current is ensured to pass through the material continuously.

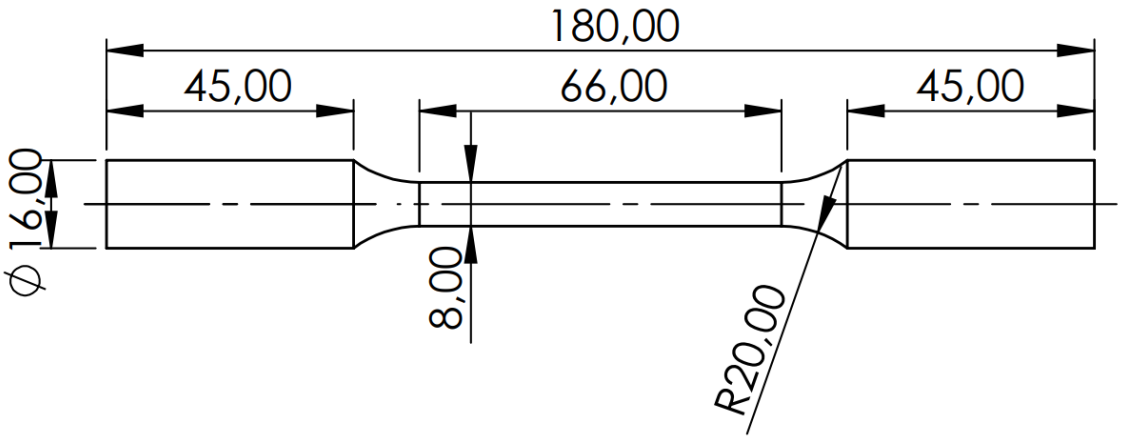

Figure 2.2 Specimen dimensions for tensile testing (unit: mm)

The tensile tests of the study were performed using Instron tensile testing setup. Tensile tests were conducted at two different strain rates, 1 s^{-1} and 1^{-3} s^{-1}, with and without hydrogen. Both of these strain rates can provide sufficient time for hydrogen-dislocation interactions. To ensure the reliability of the results, the hydrogen charged specimens were immediately placed into the tensile setup as when hydrogen charged materials are kept in environment where the hydrogen concentration is lower than the material, the hydrogen content of the material decreases with time. All the tests are performed 3 times at room temperature to ensure the consistency of the results. The fracture surfaces of the specimens after tensile testing were analyzed using SEM (model: Zeiss Gemini 300) and the effect of hydrogen on the microstructure was examined.

2.4 Results and Discussion

Figure 2.3 shows the engineering stress – engineering strain behavior of hydrogen-uncharged and hydrogen-charged Al 7075 specimens with the corresponding tensile properties at room temperature and quasi-static and medium strain rates. Even before hydrogen charging, increasing strain rate reduced the strength and ductility of the specimen which is a clear sign of negative strain rate sensitivity, and it is well discussed for Al alloys in literature [41,42]. In particular, initial strength of pure matrix, solid solution hardening, forest hardening, precipitation hardening, and dynamic strain aging (DSA) are the main components of total strength of Al alloys. Generally, DSA, due to solute-dislocation interactions, is the main strengthening mechanism at the strain rate from 10^{-4} s^{-1} to 10^{2} s^{-1} [41]. Low strain rates promote sufficient time for solute-dislocation interactions and solute atoms pin more dislocation and cause additional hardening. However, the effect of DSA on the overall hardening is suppressed as the strain rate and associated dislocation velocity increases. Therefore, DSA and associated negative strain rate sensitivity are observed for this strain rate range and this result agrees well with literature [41–43]. Hydrogen charging also deteriorates the ductility of Al 7075 alloy at both strain rates. In particular, the elongation values at failure decrease from 0.1303 to 0.1063 (18.4%) at low strain rate and 0.1042 to 0.0764 (26.6%) at high strain rate due to HE. Therefore, HE is slightly more pronounced at high strain rate as opposed to previous observations [44–46]. The effect of strain rate on HE susceptibility of different materials has been studied previously and common observation was HE is much more pronounced at low strain rates as it allows sufficient time for dislocation – hydrogen interactions. However, the effect of strain rate on HE susceptibility of Al 7075 at large strain rate range, which also triggers negative strain rate sensitivity, has not been conducted yet. Djukic et al. discuss the effects of different material, microstructural, and environmental related factors on HE susceptibility and the synergistic action of HE mechanisms [22]. In the same paper, the critical concentration of both diffusible and trapped hydrogen contents, that separates the HELP dominancy and HEDE dominancy, was discussed well [22]. That critical value and corresponding HE mechanisms are affected by the material, hydrogen content and the deformation conditions [22]. In the current study, hydrogen charging procedure remains constant for all specimens. Hence, the current results and the HE mechanism changes can be attributed to strain rate. The main reason why HE is now more dominant at high strain rate for Al 7075, can be attributed to the fact that increase in

dislocation density at high strain rate is way greater than the one at low strain rate. Therefore, this abrupt increase in dislocation density might cause decrease in the dislocation velocity after hydrogen charging and trigger more dislocation – hydrogen interaction. However, at low strain rate, the rate of dislocation density increase could be low which results in slight enhancement of dislocation velocity. In addition, hydrogen can also shield the stress field of dislocation and enhance dislocation velocity at the both strain rate. The schematic explanation of the mechanism is illustrated in Figure 2.3b. Once there is a transition from region 1 to region 2, dislocation density increases abruptly and results in decrease in dislocation velocity (Figure 2.3b). Strain rate dependency of dislocation plasticity has been discussed before and presented results correspond well with described model [47]. Hydrogen did not affect the yield stress of the material considerably as the solute solution hardening contribution to overall hardening is one of the least dominant mechanisms in Al 7075. Atomic hydrogen also decreased the ultimate tensile strength (UTS) of the material from 653 MPa to 631 MPa and 623 MPa to 607 MPa at low strain rate and high strain rate, respectively. The detrimental effect of hydrogen on UTS has been clearly discussed before and our results agree well with literature [8,17,48]. Also, Figure 2.3c shows the work hardening rate of the tested material. Figure 2.3c corresponds well with the existing discussions. In low strain rate regime, HE has no significant effect on the hardening behavior of Al 7075 whereas it led to reasonable ductility loss. As shown in Figure 2.3c, in low strain rate regime the work hardening rates show nearly the same tendency for the H-charged and H-uncharged conditions. On the contrary, the working hardening rate differs at high strain rate regime. This fact was addressed through the adiabatic heating phenomena by the authors. This finding is a general response for most of the metallic material's and was previously documented by numerous researchers [49–51]. Moreover, the H-uncharged specimen exhibits quite low work hardening rate, in addition, the overall plastic response can even be approximated as perfect plastic behavior. However, the H-charged specimen at high strain rate has a distinguishing character from the H-uncharged one. In our view, this can be interpreted as the supplementary interaction of hydrogen with the dislocations. In that case, the effect of adiabatic heating was revenged by the hydrogen induced dislocation motions which results in a high work hardening rate similar to the outputs of quasi-static regime tests.

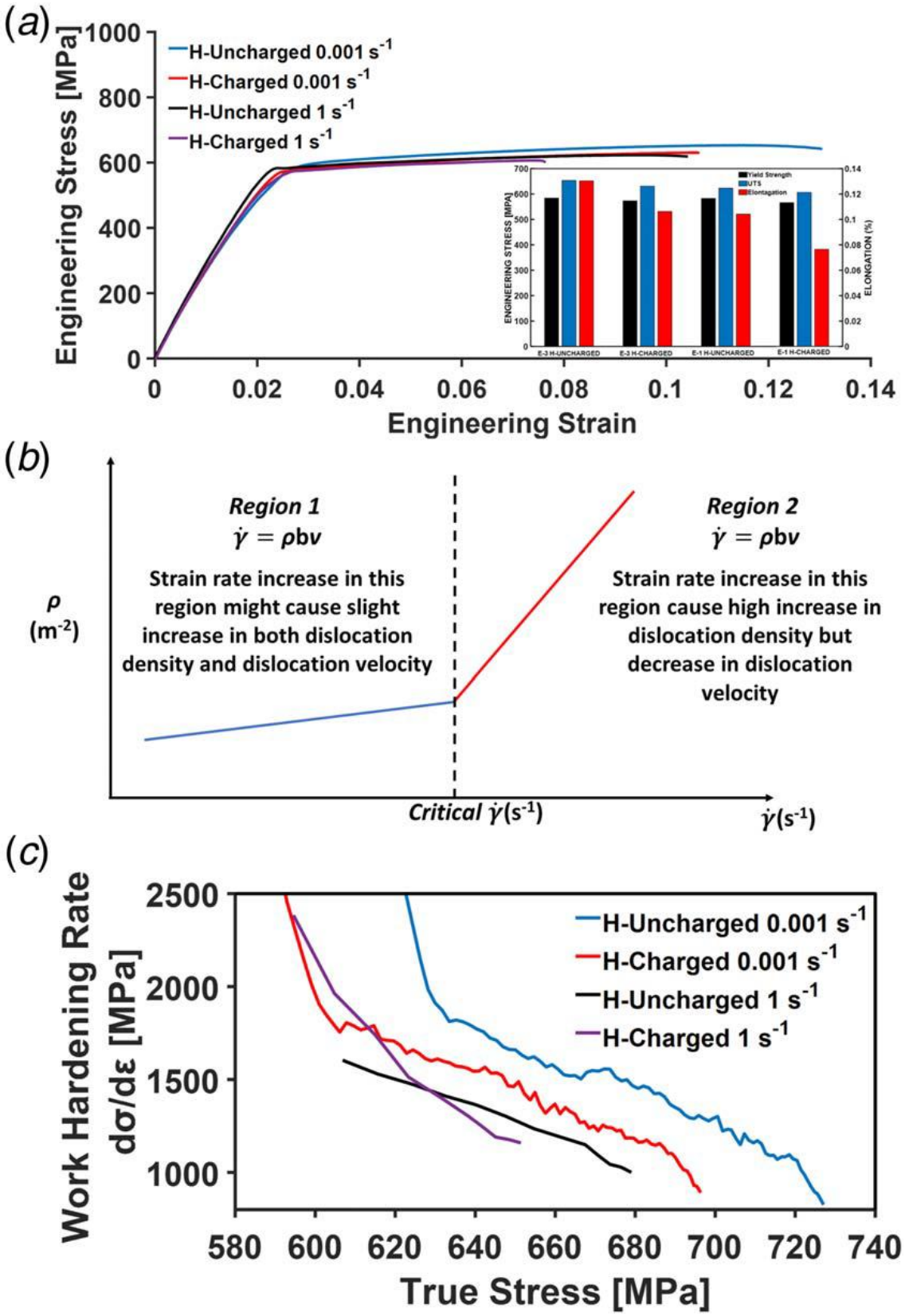

Figure 2.3 a) Tensile test result of the Al 7075 with and without hydrogen charging at different strain rates, b) Proposed HE mechanism with dislocation mechanisms, c) Work hardening behavior of Al 7075 under different strain rates with and without hydrogen charging.

Figure 2.4 shows the photographs of fractured specimens after tensile tests and Figure 2.4a and Figure 2.4b show the macroscopic crack path of fractured H-uncharged specimens at slow and high strain rates, respectively. It can clearly be seen that crack was propagated almost 45 deg to the tensile direction at low strain rate but more zig-zag type crack propagation pattern was observed at higher strain rate which is an indication of increased brittleness with strain rate. This is expected behavior since as the strain rate increases the generation rate of dislocations also increases and once the strain localization cannot be accommodated plastically and there is not enough time for dislocation movement sudden failure occurs. In Figure 2.4c and Figure 2.4d, the deformed H-charged specimens are presented. When compared to their hydrogen free counterparts, they exhibit more brittle fracture surface due to HE. The reason for changing of the fracture path from 45 deg, indication of shear failure, to flat surface are hydrogen decreases the critical resolved shear stress for void coalescence and accelerate failure (hydrogen effect) and the fracture happens in a short time due to strain location (strain rate effect). Following SEM micrographs express both effects more clearly.

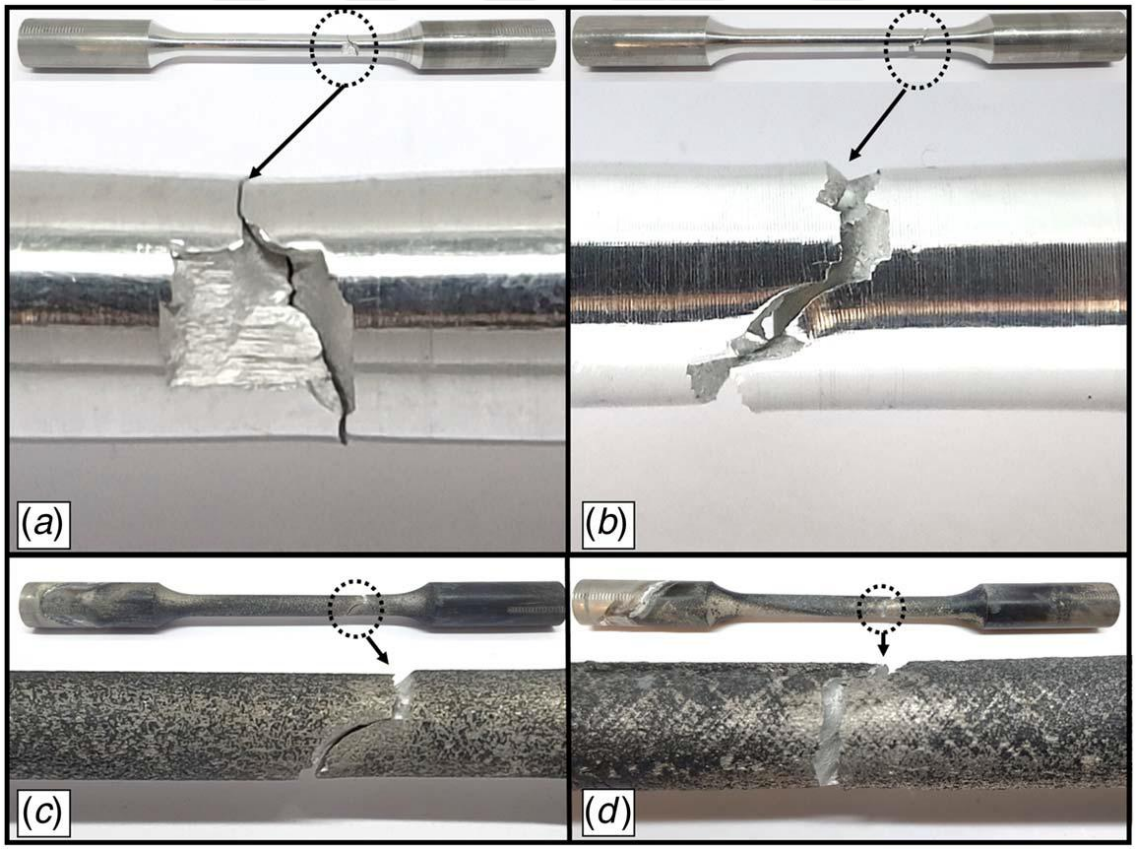

Figure 2.4 Photographs of the fractured specimens. a) and b) belongs to H-uncharged specimens which tested with 10^{-3} s^{-1} and 1 s^{-1} strain rates respectively. c) and d) belongs to the H-charged specimens which tested with 10^{-3} s^{-1} and 1 s^{-1} strain rates respectively.

Figure 2.5 shows the fracture surface SEM images of H-uncharged specimens. In particular, Figure 2.5a and Figure 2.5b belong to the specimens fractured at an initial strain rate of 10^{-3} s^{-1}. The fracture surface of Al 7075 at lower strain rate was made up of fine dimples, an indication of ductile fracture [44]. In addition, inclusions were also observed in some dimples, suggesting that inclusions act as the initiation sites of microvoid coalescence (MVC). It was reported for Al 7075 that inclusions can be either Fe-based or Si-based which were underlined as Fe-bearing and Si-bearing inclusions [52]. Based on the chemical composition presented in Table 2.1, the inclusions observed inside dimples were Si-based. These results correspond well with previously published results of Al 7075 alloy [52]. Around the inclusions, the stress concentration increases, the voids are developing and fracture can initiate from these regions [53]. Figure 2.5c and Figure 2.5d show the fracture surface of hydrogen uncharged Al 7075 at higher strain rate and it can be observed that the volume fraction of dimples decreases with strain rate. In addition, deep crack was also observed on the fracture surface, indicating the loss of ductility over lower strain rate case. These micrographs strengthen the discussion made for Figure 2.4 and aggress well with literature [38,54].

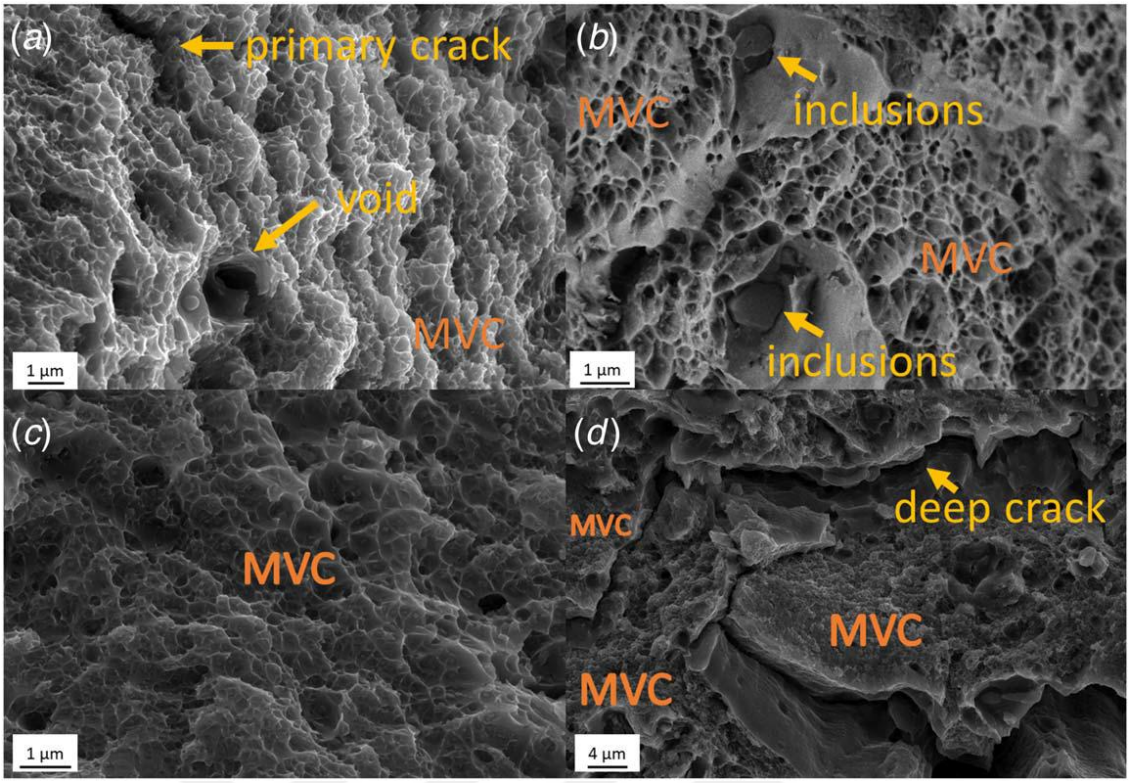

Figure 2.5 Fracture surface of hydrogen uncharged specimens. a) 10^{-3} s^{-1} strain rate, b) magnified SEM micrograph at 10^{-3} s^{-1} strain rate, c) 1 s^{-1} strain rate, d) magnified SEM micrograph at 1 s^{-1} strain rate.

Figure 2.6 shows the fracture surfaces of hydrogen charged and fractured specimens. Figure 2.6a and Figure 2.6b show the SEM micrographs of hydrogen charged and fractured specimens at an initial strain rate of 10 $^{-3}$ s^{-1}. It was observed that deep primary cracks and secondary crack, voids as well as nano-sized dimples contribute to the fracture mechanism of Al 7075 at lower strain rate. Thus, hydrogen changed the fracture mode from ductile to mixed mode (ductile+brittle). Mixed mode fracture was reported for the hydrogen charged specimens that are tested at slow strain rate [17,36,38]. The fraction of ductile to brittle fracture features present the ratio of HELP and HEDE mechanism modes [22]. The dominancy shifts from HEDE to HELP as the MVC increases and brittle features decreases [22]. As more ductile features were present on the fracture surface and we observed several dimples, HELP was more dominant HE mechanism at low strain rate. However, HE is more pronounced at higher strain rate according to tensile tests and SEM micrographs also prove this observation. These observations aggress well with the literature [22] . Figure 2.6c and Figure 2.6d show the SEM micrographs of hydrogen charged and fractured specimens at an initial strain rate of 1 s^{-1}. Increasing strain rate increased volume fraction of primary and secondary cracks

whereas less MVC was observed at higher strain rate. Deeper cracks can be attributed to the decrease in cohesive energy associated with HEDE mechanism [22]. In addition, decreased dislocation velocity explained in the discussion of Figure 2.3b also provided more time for hydrogen – dislocation interactions and promote HE.

Since there are also ductile features (MVC) on the fracture surface at the existence of hydrogen (Figure 2.6d), HELP mechanism is also active [22]. Thus, coexistence of HELP+HEDE is present at higher strain rate. Coexistence of both HELP and HEDE mechanisms at the same time scale was also reported before and consistent with the current results [9,22].

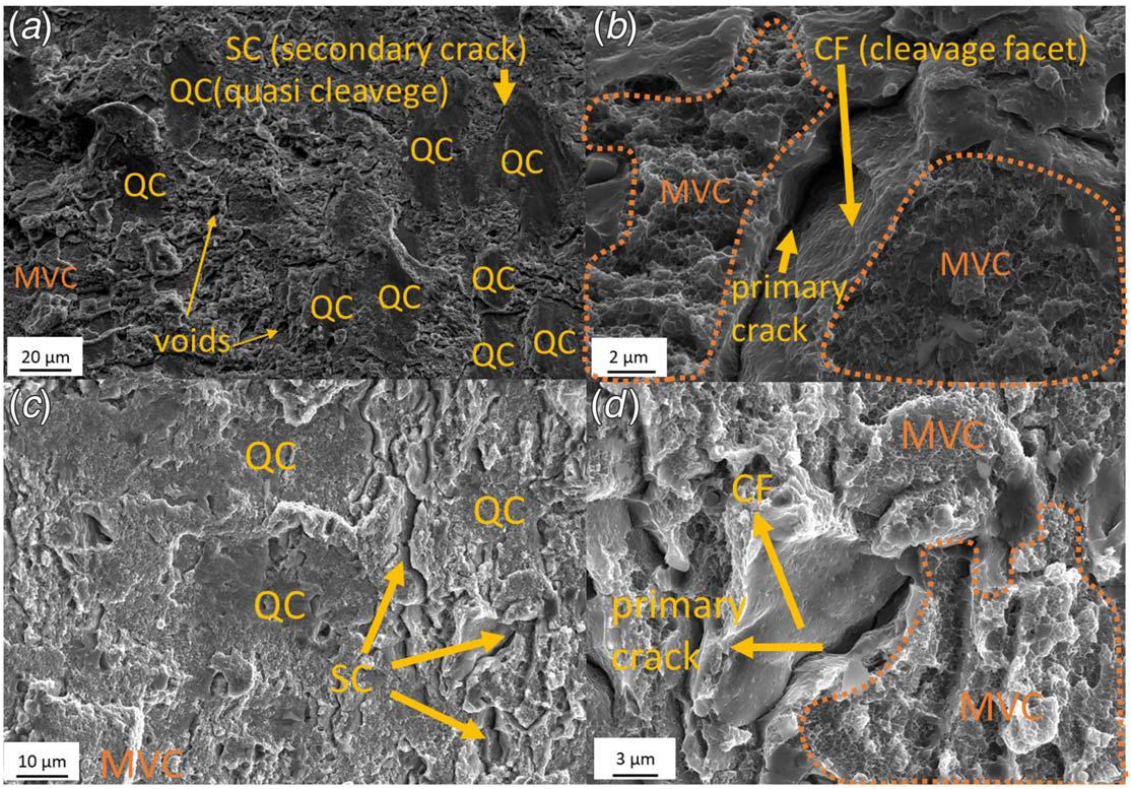

Figure 2.6 Fracture surface of hydrogen charged specimens. a) 10^{-3} s^{-1} strain rate, b) magnified SEM micrograph at 10^{-3} s^{-1} strain rate, c) 1 s^{-1} strain rate, d) magnified SEM micrograph at 1 s^{-1} strain rate.

Figure 2.7 shows the diffusion length of the hydrogen in Al 7075. These SEM micrographs belong to fracture of hydrogen charged specimen and greater strain rate. Both of the images belong to the same specimen and without annotations, they are same. The annotations represent two different transition scenarios. The dashed line seperates ductile ductile region (hydrogen unaffected) from brittle region (hydrogen affected). Fick's first law was utilized to compute the hydrogen diffusion constants (D and D_0) of

Al 7075. The hydrogen diffused depth is calculated using Solidworks 2021 by importing the SEM images with transition line. According to the results, the hydrogen is diffused 2.20 mm and 2.43 mm into the material as it is shown in Figure 2.7a and Figure 2.7b, respectively. In that depth, the concentration of the hydrogen is very small that is close to zero. With the help of this knowledge, diffusion coefficient (D) and pre-exponential factor (D_0) are calculated using the following equation.

$$\frac{C_x - C_0}{C_S - C_0} = 1 - \mathrm{erf}\left(\frac{x}{2\sqrt{Dt}}\right) \text{ where } D = D_0 * \exp\left(\frac{-Q_d}{RT}\right)$$

where Q_d is activation energy and was taken as 16.4 kJ/mol for Al 7075 T6 [55].

The resulting D value is $1{,}79*10^{-12}$ m^2/s and $2{,}18*10^{-12}$ m^2/s for 2.20 mm and 2.43 mm in depth, respectively. Likewise, D_0 in our study was calculated as $1.5038*10^{-9}$ m^2/s for 2.20 mm depth and $1.8446*10^{-9}$ m^2/s for 2.43mm depth for 24 charging time. Calculated D and D_0 values are consistent with literature [17,56].

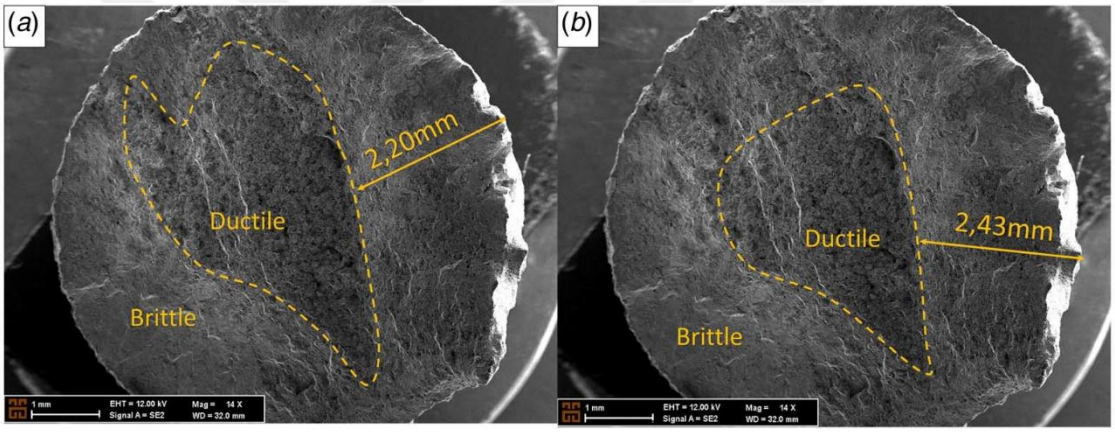

Figure 2.7 SEM micrographs showing the diffusion length of hydrogen.

2.5 Conclusion

In this study, the effect of strain rate on HE susceptibility of Al 7075 alloys was investigated at large strain rate range, including quasi-static and medium strain rate ranges. The chemical composition of the material was analyzed using EDX. To investigate the strain rate sensitivity in large strain rate range, tensile tests were conducted on both hydrogen uncharged and hydrogen charged samples at 1 s^{-1} and^{-3} 1 s^{-1} strain rates, and fracture surfaces were investigated using SEM. All tests were repeated three times to ensure the consistency of the results. It was observed that, Al 7075 exhibits negative strain rate sensitivity due to DSA at these strain rates. In particular, DSA was the dominant hardening mechanism at lower strain but its effect became less dominant as the strain rate

increased to medium strain rate range. In addition, HE was more pronounced at higher strain rate as opposed to previous studies on strain rate effect on HE. This conclusion can be attributed to the fact that, increase in dislocation density after critical strain rate (Figure 2.3) is way greater than the one at lower strain rates. Therefore, a sharp increase in dislocation density after critical strain rate causes decrease in the dislocation velocity after hydrogen charging and promotes more time for dislocation – hydrogen interactions, leading to more HE. SEM micrographs were taken from fractured surfaces and fraction features were discussed. SEM micrographs also suggest that hydrogen induced damage was more pronounced at higher strain rate. Specifically, HELP was more dominant HE mechanism at quasi-static strain rate but coexistence of HELP+HEDE was observed at medium strain rate. After the investigation of fracture surface, the hydrogen diffusion coefficient was calculated using computer-aided design applications. According to the result, the diffusion coefficient is consistent with literature.

Acknowledgement

B. Bal acknowledges the financial support by AGU-BAP Project No. 174 and the Scientific and Technological Research Council of Turkey (TUBITAK) BIDEB-2219 Postdoctoral Research Program under Project No. 1059B192000774.

Chapter 3

Hydrogen Susceptibility of Al 5083 Under Ultra High Strain Rate Ballistic Loading [57]*

*This study has been published on Materials Testing Journal and the content has been reprinted with permission.

Abstract

The effect of hydrogen on the ballistic performance of aluminum (Al) 5083H131 was examined both experimentally and numerically in this study. Ballistics tests were conducted at a 30° obliquity in accordance with the ballistic test standard MIL-DTL-46027 K. The strike velocities of projectiles were ranged from 240 m s^{-1} to 500 m s^{-1} level in the room temperature. Electrochemical hydrogen charging method was utilized to introduce hydrogen into material. Chemical composition of material was analyzed using energy dispersive X-ray analysis (EDX). Instant camera pictures were captured using high-speed camera to compare H-uncharged and H-charged specimen ballistics tests. The volume loss in partially penetrated specimens were assessed using the 3D laser scanning method. Microstructural examinations were conducted utilizing scanning electron microscopy (SEM). It was observed that with the increased deformation rate, the dominance of the HEDE mechanism over HELP became evident. Furthermore, the experimental findings were corroborated through numerical methods employing finite element analysis (FEM) along with the Johnson-Cook plasticity model and failure criteria. Inverse optimization technique was employed to implement and fine-tune the Johnson-Cook parameters for H-charged conditions. Upon comparing the experimental and numerical outcomes, a high degree of consistency was observed, indicating the effective performance of the model.

3.1 Introduction

Owing to their exceptional mechanical properties, such as high strength, lightweight, workability, significant ductility, and reasonable corrosion and wear resistance, aluminum (Al) alloys are highly suitable for a wide range of applications in industries such as aerospace, automotive, and marine [58–60]. These mechanical properties can be further enhanced by alloying, which serves as the primary method of Al alloy subcategorization. For instance, in the Al 5XXX series, the primary alloying element that constitutes solute solution hardening is magnesium (Mg) [60–62]. As a member of the Al 5XXX series of alloys, Al 5083 is composed of various elements, including magnesium (Mg), manganese (Mn), iron (Fe), silicon (Si), chromium (Cr), zinc

(Zn), titanium (Ti), copper (Cu), and Al as the balance element [63]. The main strengthening mechanisms of this alloy are solute-solution hardening, precipitation hardening, grain-boundary hardening, and strain hardening [64,65]. Mg-Al clusters provide impressive strengthening based on Hume-Rothery rules and corrosion resistance. In addition, the crystal structure of Al 5083 is face-centered cubic (FCC) at room temperature [14]. This crystal structure provides a low hydrogen diffusion coefficient ($7x10^{-13}$ m^2 s^{-1}) compared to body-centered cubic (BCC) crystal structure due to its greater atomic packing factor [66–68]. Therefore, Al 5083 can used in hydrogen embrittlement (HE) resilient infrastructures in several areas, such as gas storage, pipelines, or space applications [67,69]. Yet, it was also reported that Al 5083 is also vulnerable to HE, as discussed in previous studies [67,68,70]. Therefore, the HE susceptibility of Al 5083 should be investigated in detail.

Manufacturing processes and usage conditions, particularly those involving chemical reactivity, high temperatures, and elevated pressures, entail a risk of hydrogen diffusion [2,3]. Hydrogen in metallic materials has a pronounced impact on their ductility, strength, fracture toughness, and fatigue behavior [2,4–7]. This adverse effect, called HE, can lead to catastrophic failure [2,3,21,71–74]. The literature discusses HE's atomic/micro/macro mechanisms. HEDE (hydrogen-enhanced decohesion mechanism), HELP (hydrogen enhanced localized plasticity), HEMP (hydrogen enhanced macroscopic ductility), AIDE (adsorption-induced dislocation emission), HDMC (hydrogen assisted micro void coalescence), DHF (decohesive hydrogen fracture), MF (Mixed fracture), HAM (hydrogen changed micro-fracture mode) are some of the HE mechanisms [3,4]. The coexistence of different HE mechanisms is also acknowledged in the literature [75]. According to HEDE, hydrogen within the lattice reduces the cohesive strength of the metal bonding [76]. As per the HELP model, the hydrogen atoms next to the crack tip lead to local plasticization by causing a decrease in the energy required to initiate dislocation movement [75]. Despite many proposed mechanisms included in the literature, research still goes on to reveal HE [3,8,9,11,68].

The HE mechanisms and nature are affected by a combination of material, environmental, and mechanical factors. For instance, as the strength of a material increases, its susceptibility to HE also increases [77]. The effects of strain rate [3], strength [77], grain size [78], dislocation density [79], and temperature [80] on various metallic materials have been studied intensively. It is commonly accepted that materials are more susceptible to HE at slower strain rates as it provides more time for hydrogen-

dislocation interactions [45,81]. However, in our previous study, we studied the effect of impact loading of Al 7075 alloy, and it has been concluded that HE can also be active at greater strain rates [9]. In particular, if the dislocation speed is significantly low (at approximately 0.01 m s^{-1}), dragging the hydrogen cloud by the dislocation core promotes HE [82]. However, once the dislocation speed is way greater than the speed of hydrogen, pinning-depinning-detrapping events correspond to the nature of HE [82]. The Al 5083 is used in the military, particularly in constructing vehicle hulls and as an armor plate [83,84], so its HE susceptibility at ultra-high strain rates should be investigated. In literature, several ballistic test studies have been conducted on hydrogen storage materials without hydrogen charging [85–88]. On the contrary, to the best of the authors' knowledge, no study reveals the effect of ultra-high strain rate loading on HE susceptibility of Al 5083.

In addition to experimental contributions, there is a significant attempt to utilize numerical methods to characterize the ballistic behavior of materials. Among these numerical techniques, the finite element method (FEM) is particularly prominent due to its capability to effectively model complex geometries, boundary conditions, and material responses. Various empirical constitutive theories have been employed within the framework of FEM to simulate the rate-dependent deformation behavior of materials [89–92]. However, the challenge of calibrating material constants for certain cases significantly restricts their practical utility in numerical simulations. The Johnson-Cook (J-C) model provides a versatile setting that effectively describes materials' rate-dependent flow and failure behavior in ballistic testing simulations. The J-C model offers simplicity compared to more complex rate-dependent plasticity models without sacrificing accuracy, greatly facilitating the calibration process by reducing the number of parameters required. The J-C model has been extensively employed in multiple studies to simulate the ballistic behavior of various materials [93–96]. In particular, Rai et al. [97] apply the J-C plasticity model and its failure criterion to investigate the ballistic impact on an AA5083-H116 aluminum plate. Børvik et al. [98] utilize the J-C model to evaluate the ballistic perforation resistance of AA5083-H116 aluminum plates, highlighting the crucial consideration of thermal softening and presenting an alternative approach to determine material constants. Hence, these studies demonstrate that the J-C plasticity model, coupled with its failure criterion, can serve as a potent tool for modelling the ballistic behavior of AL 5083 H131, especially when dealing with the challenges posed by the complex process of hydrogen susceptibility.

The first aim of this study is to identify the effect of hydrogen on the mechanical response of Al 5083 by applying ballistics tests and to investigate the underlying HE mechanisms under ultra-high strain rate loading. For these purposes, energy-dispersive X-ray (EDX) spectroscopy analysis was employed to examine the chemical composition of received material. Prior to the tests, an electrochemical charging procedure was utilized to introduce hydrogen to H-uncharged specimens. The ballistic response of Al 5083 was examined across a range of projectile strike velocities, spanning from 235 m s^{-1} to 502 m s^{-1}. A high-speed camera was employed to capture ballistics tests and calculate the residual velocities of projectiles. Following the ballistics tests, the microstructure was evaluated using scanning electron microscopy (SEM) and 3D laser scanning images. The second aim of this study is to employ the Johnson-Cook (J-C) plasticity model to characterize the material's ballistic behavior and failure of Al 5083-H131 in the presence of hydrogen susceptibility. Furthermore, an ad-hoc inverse optimization-based approach has been developed to efficiently calibrate the material parameters for the hydrogen-susceptible material. Finally, the experimental results obtained from finite element analysis (FEA) are compared with experimental data to demonstrate the predictive capability of the proposed modelling approach.

3.2 Experimental and theoretical approach

3.2.1 Material

Ballistics test plate specimens were fabricated from Al 5083-H131, possessing dimensions of 100 mm × 100 mm × 10 mm. Aluminum is an FCC material, and dislocation movements occur at very low stress levels and do not require thermal activation [14,99]. Therefore, we can observe dislocation-hydrogen interactions and the effects of hydrogen on ballistic performance even at high strain rates. In BCC materials, however, since dislocations are thermally activated, they may not be activated even at very high strain rates [99]. As a result, dislocation-hydrogen interactions may not occur, and the effects of hydrogen may not be observed. The designation of H131 temper signifies that the material has undergone a degree of strain hardening, which falls below the threshold necessary for attaining a controlled H13 temper [100]. An EDX analysis was conducted utilizing the Zeiss Gemini 300 instrument to determine the material's elemental composition. The composition data obtained is presented in Table 3.1, while

the region on the surface from which the EDX data were collected is shown in Figure 3.1. The content corresponds well with the data found in the existing literature [63]. The deviation from Standard EN 573 can be accepted considering the potential for variation in surface content and potential errors associated with the EDX analysis.

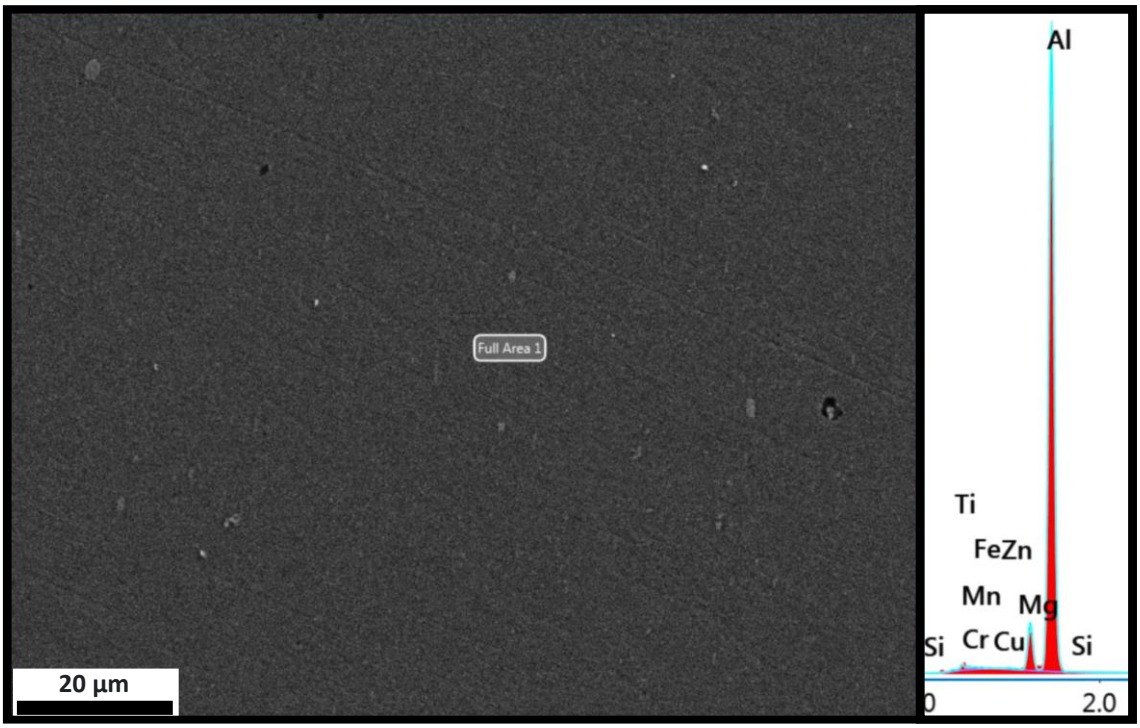

Figure 3.1 The region where EDX analysis was conducted and the corresponding EDX analysis graph results of the as-received material.

Table 3.1 EDX analysis result of the region that is presented in Figure 3.1 (wt.%)

Mg	Mn	Cr	Ti	Zn	Fe	Si	Cu	Al
5.46	2.01	1.14	0.77	0.18	0.13	0.09	0.05	Balance

3.2.2 Electrochemical charging

Al 5083 specimens were charged with hydrogen using an electrochemical process before ballistics testing. During the electrochemical charging process, an aqueous solution containing 3 g L^{-1} NH_4SCN (ammonium thiocyanate) and 3% NaCl was used [40]. A direct current (DC) power supply performs the charging process. The power supply was operated in a constant current mode, thus ensuring a consistent current flow and reducing possible variations due to surface resistance differences during the charging process. A current density of 50 A m^{-2} was applied to the specimens during the charging process. A Platinum (Pt) counter electrode, which acts as an anode in the charging setup,

was used as a counter electrode, and the specimens were connected to the charging system as a cathode. Hydrogen cations (H+) diffuse into the cathode specimen during this procedure. The charging time was determined using Fick's law Equation (3.1).

$$\frac{C_x - C_0}{C_S - C_0} = 1 - \mathrm{erf}\left(\frac{x}{2\sqrt{Dt}}\right) \tag{3.1}$$

This equation's diffusion coefficient (D) was 7 x 10^{-13} m^2 s^{-1} [66–68]. A depth versus concentration graph was generated for various time intervals using this diffusion coefficient, as shown in Figure 3.2. The charging time was 72 hours to exceed subsurfaces and reach lattice sites.

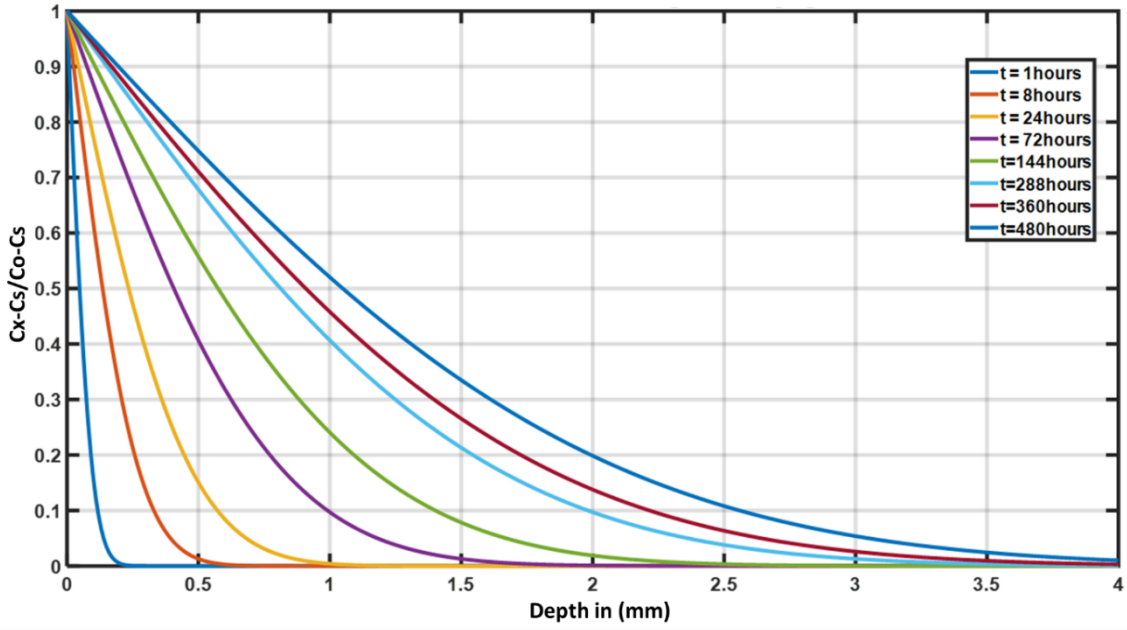

Figure 3.2 Variation of hydrogen concentration over time at different depths.

3.2.3 Ballistics tests

Ballistics experiments were performed at Erciyes University using a single stage gas gun test configuration. This setup achieved acceleration by moving the projectiles with compressed helium. It is possible to adjust the projectile's velocity by adjusting the applied pressure. The varying velocities of projectiles have different penetration potentials due to the different kinetic energies associated with each speed. To assess their performance in ballistics tests, both the H-uncharged specimens and H-charged specimens were independently subjected to testing. Figure 3.3 shows the position of the fixed specimen in the target chamber. Two optical sensors are positioned between this chamber and the point of projectile propulsion to precisely measure the velocity of the

projectiles. The Photran high-speed camera, in conjunction with the black-white distance paper placed inside the chamber, was used to measure the residual velocity. Throughout the testing process, a constant obliquity angle of 30° was used for the ballistics tests [101], as visually shown in Figure 3.3. The fragment-simulation projectile has the standard of MIL-DTL-46593B [102]. By standard, the projectile material is 4340H steel with a Rockwell hardness of HRC 30±1 and a caliber of 0.30.

Figure 3.3 Ballistic test chamber

3.2.4 3D Laser scanning of the deformed surfaces

Since gas gun tests typically provide qualitative results such as complete or partial penetration, 3D laser scan studies were also conducted to investigate the damaged surfaces. The objective was to extract quantitative results that can be correlated with the effect of hydrogen content on ballistic performance. More particularly, the main objective of this scanning effort is to observe and compare any possible topological difference between the H-uncharged and H-charged specimens. For that purpose, a specifically designed and manufactured laser scanner was used, which is present at Psaron-HTI company. In general, a laser scanner can be termed a device that uses a laser beam to scan an object or environment and generates a 3D model or map of the studied area. In other

words, a laser scanner projects a laser beam onto the object's surface or environment and measures the distance between the scanner and the inspected surface. If this projected distance can be measured with a high axial resolution and proper stitching algorithms, it can be feasible to create a 3D model or map of the scanned area [103]. The laser scanner device is depicted in Figure 3.4, which functions as a line scanner. It emits a laser beam from the laser source and focuses it into a narrow line using the lens or optical system. As the beam is directed across the surface, it interacts with the surface and reflects to the detector. The detector measures the time the laser beam travels from the laser source to the surface and back. The distance from the source to the surface is calculated using the speed of light and estimated time.

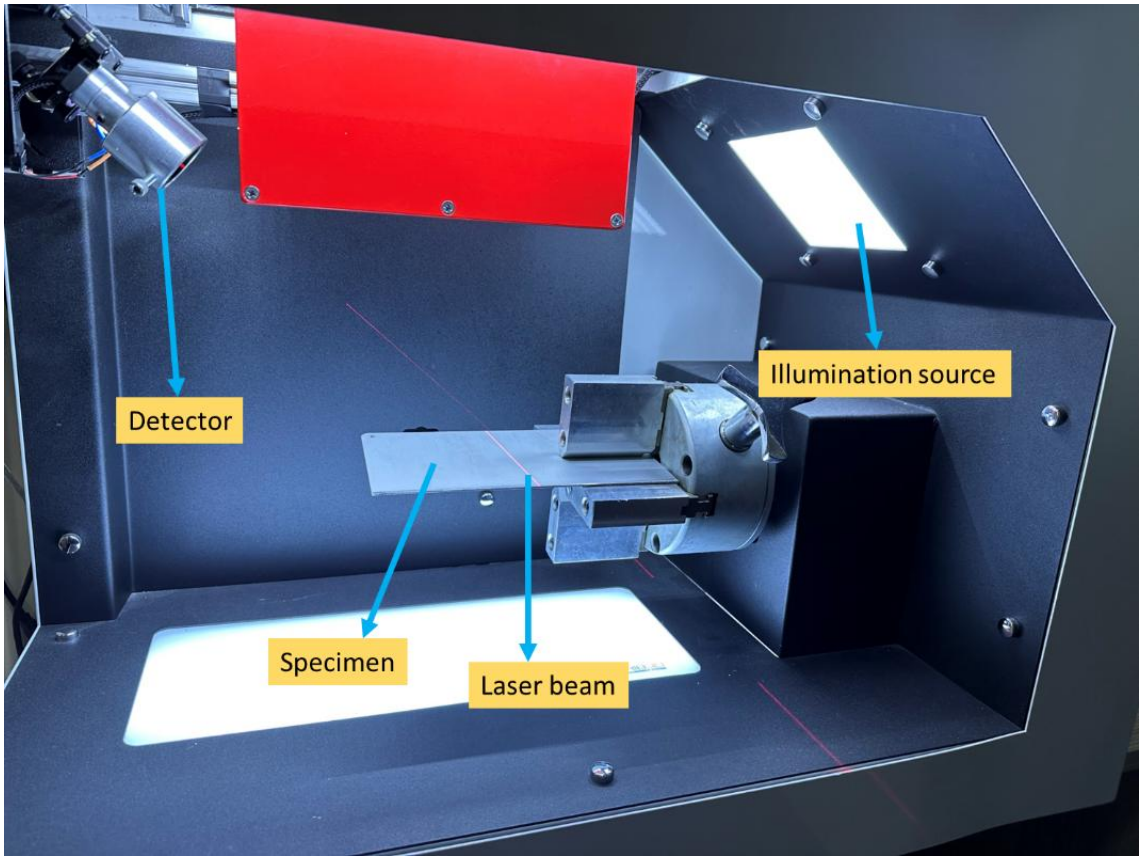

Figure 3.4 Laser scanner device

3.2.5 Mathematical modelling

3.2.5.1 Johnson-Cook plasticity model

The Johnson-Cook plasticity model [104] is employed to characterize the flow behavior of Al 5083 in ballistic test simulations. This constitutive model incorporates

three key aspects: strain rate sensitivity, isotropic strain hardening, and thermal softening. These components are represented in a paired manner, as described Equation (3.2) below:

$$\bar{\sigma} = \left[A + B\left(\bar{\varepsilon}_p\right)^n\right]\left[1 + C\ln\left(\frac{\dot{\bar{\varepsilon}}_p}{\dot{\varepsilon}_0}\right)\right]\left[1 - \left(\frac{T - T_r}{T_m - T_r}\right)^m\right] \tag{3.2}$$

with $\bar{\sigma}$: flow stress at nonzero strain rate, $\dot{\bar{\varepsilon}}_p$: equivalent plastic strain rate, $\dot{\varepsilon}_0$: refence strain rate measured at or below the transition temperature, T: current temperature, T_r: transition temperature, T_m: melting temperature, and A, B, n, C and m: material constants measured at or below the transition temperature.

The values of the material constants can be determined by fitting the constitutive equations to the true stress-strain curves obtained from experimental data at various strain rates and temperatures.

3.2.5.2 Johnson-Cook Dynamic Failure

The fracture criterion initially proposed by Hancock and Mackenzie [105] has been expanded by Johnson and Cook [104] to incorporate additional factors such as stress triaxiality, temperature, strain rate, and strain path, making the failure strain sensitive to these parameters. According to the model, damage accumulates within the material elements as plastic straining occurs. A damage variable, denoted as D, is used to quantify the extent of damage, ranging from 0 (indicating no damage) to 1 (representing the complete failure of the material). Failure is deemed to have taken place when the value of D reaches 1. D, the damage variable, is defined as:

$$D = \sum\left[\frac{\Delta\bar{\varepsilon}_p}{\bar{\varepsilon}_p^f}\right] \tag{3.3}$$

with $\Delta\bar{\varepsilon}_p$: increment of equivalent plastic strain and the summation encompasses all increments in the analysis, $\bar{\varepsilon}_p^f$: strain at failure which is a function of the strain ratio $\dot{\bar{\varepsilon}}_p/\dot{\varepsilon}_0$ and the stress triaxiality ratio, σ_m/σ_{eq}, σ_m: Mean stress or hydrostatic stress, and σ_{eq}: Von Mises stress.

The strain at failure can be expressed in a separable form as follows:

$$\bar{\varepsilon}_p^f = \left[d_1 + d_2\, exp\left(d_3\,\frac{\sigma_m}{\sigma_{eq}}\right)\right]\left[1 + d_4\, ln\left(\frac{\dot{\bar{\varepsilon}}_p}{\dot{\varepsilon}_0}\right)\right]\left[1 + d_5\left(\frac{T - T_r}{T_m - T_r}\right)\right] \tag{3.4}$$

with d_1 to d_5: failure parameters are represented by and these measurements are taken at or below the transition temperature and $\dot{\varepsilon}_0$: reference strain rate.

3.2.5.3 Parameter identification

The finite element simulations of the ballistic test experiment require identifying two sets of Johnson-Cook parameters for both H-uncharged and H-charged specimens. The parameters for the H-uncharged specimen are derived from a previous study conducted by Rai et al. [106] based on the similarity of the materials. For the determination of Johnson-Cook parameters of H-charged specimens, however, an inverse optimization-based approach has been employed in view of a scarcity of experimental data. This approach can offer an alternative way to identify the material parameters under H-charging conditions accurately. It is worth noting that the inverse parameter identification technique has been widely used in various contexts [107–111].

The optimization problem is formulated by adopting the average squared difference between the simulated and experimental residual velocities as the objective function. This objective function effectively captures the overall deviation between the experimental and simulated data, making it a suitable choice for optimization. Bochkaryova et al. [112] concluded that although the hydrogenated form of the alloy exhibits reduced ductility compared to the original alloy, the plastic flow behavior remains mainly unchanged. Inspired by the study of Bochkaryova et al. [112], the optimization process focuses on adjusting parameters d_1 to d_5 to minimize the objective function. These parameters have been selected based on their relevance and influence on the simulation results, as they characterize the material's damage evolution and fracture behavior. The objective function, therefore, for this optimization problem can be written as

$$f(d_1, d_2, d_3, d_4, d_5) = \frac{1}{N}\sum\left[R_{exp} - R_{sim}\right]^2 \tag{3.5}$$

with$f(d_1, d_2, d_3, d_4, d_5)$: objective function that computes the average squared difference between the experimental residual velocities, R_{exp} and R_{sim}: simulated residual velocities obtained using the parameters d_1 to d_5, N: total number of data points.

It is also important to note that the scale variation in the parameters d_1 to d_5 is relatively small and falls within a manageable range. As a result, normalization may not be necessary in this case, leading to a simplified optimization process and enhancing the predictions' reliability.

The proposed optimization problem also incorporates constraints on the parameters d_1 to d_5 values. These constraints ensure that the optimization process remains within acceptable bounds and help preserve the physical relevance, leading to more reliable and meaningful results. The constraints can be based on physical limitations or prior

knowledge regarding the parameters. Here, the allowable range for the variation of the damage parameters reported by Bal and coworkers [113] for Fe-16Mn-0.6Ce-2.15Al TWIP steel is used as the reference. Given the similarity in the face-centered cubic (FCC) crystal structure of the material under investigation and Fe-16Mn-0.6Ce-2.15Al TWIP steel, it is hypothesized that the range of change for the parameters d_1, d_2, d_3, d_4 and d_5 would be approximately equal to 18%, 14%, 65%, 58%, and 14% respectively.

The genetic algorithm (GA) is the optimization algorithm for optimizing the damage parameters to minimize the average squared difference between the experimental and simulated residual velocities. The GA is a highly effective metaheuristic method due to its ability to explore parameter spaces and generate diverse solutions over multiple generations. Compared with other methods, it has better handled complex and nonlinear problems in large search areas. To derive the optimized values for the parameters d_1 to d_5. The proposed genetic algorithm consists of four main steps. The first step is fitness evaluation, which uses residual velocities from finite element simulations to assess each solution's objective function. This process measures how well each solution set aligns with the desired values and identifies solutions that better fit the experimental data. The second step is selection, where the population probability is allocated to individuals based on their fitness level. The roulette wheel selection procedure selects suitable individuals for the next generation, ensuring that individuals with higher fitness levels are more likely to be propagated, consequently improving the population's overall fitness. In the third step, crossover, a one-point crossover technique combines genetic information from selected parent solutions and generates offspring solutions. This process enables the exploration of different combinations of genetic material, facilitating the introduction of diverse genetic traits into the population. Finally, in the mutation stage, a uniform mutation technique is used to introduce random changes to the parameter values of individual solutions. This step aids in maintaining genetic diversity within the population and avoiding premature convergence to suboptimal solutions by presenting small random changes.

Through the iterative processes of fitness evaluation, selection, crossover, and mutation, the genetic algorithm converges toward high-quality solutions that minimize the difference between the simulated and experimental residual velocities. The optimization problem has been implemented in a Python code integrated with the Abaqus/Explicit solver. This interface will allow for seamless interaction between the optimization algorithm and a finite element simulation. While communicating with

Abaqus to simulate the necessary simulations, a Python code is responsible for parameter adjustments, fitness evaluations, and generation updates. The Python code retrieves the simulation residual velocities' results and then uses them to determine the objective function in each generation. In this way, the proposed setting ensures the exact and effective appraisal of objective functions by directly obtaining simulated velocities from finite element simulations.

The convergence of the optimization process is shown in Figure 3.5a, which provides information on the best values for d_1, d_2, d_3, d_4 and d_5 over iterations. The plots reveal that these parameters are refined to minimize the objective function. The plateau area represents parameter stability, d_1 at 0.0222, d_2 at 0.241, d_3 at -0.524, d_4 at 0.077, and d_5 at 14.6, signifying the successful identification of optimal parameter values. In addition, plateau areas suggest that these stable parameter values remain relatively the same during subsequent iterations. Figure 3.5f illustrates the convergence and improvement of the optimization process through the variation of the objective function. The decreasing trend of the aim function over iterations shows an increasing correlation between simulated and experimental data—the plateau areas in the plot point to a satisfactory solution, indicating little scope for improvement. Figure 3.5f also confirms the effectiveness of the optimization algorithm for determining optimal parameter values, which improves simulation accuracy Table 3.2 summarizes material constants, including JC parameters for the H-uncharged and charged Al 5083 plate.

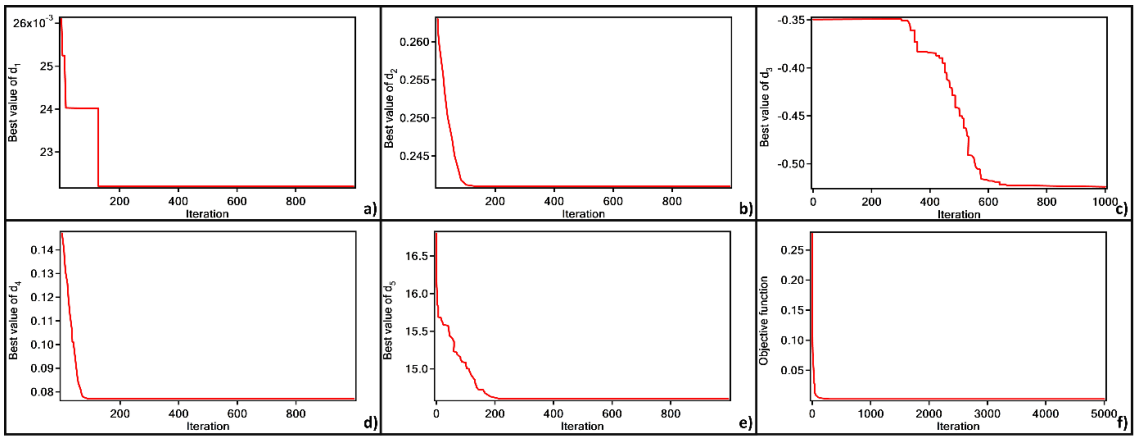

Figure 3.5 Optimization progress and objective function variation, a) to e) best values versus iterations, f) objective function versus iterations.

Table 3.2 Summary of material constants for H-uncharged and charged Al 5083 plate.

	E (GPa)	ρ (kg.m^{-3})	ν	A (MPa)	B (MPa)	n	C	m	d_1	d_2	d_3	d_4	d_5
H-uncharged [106]	70	2660	0.33	167	596	0.551	0.001	0.859	0.0261	0.263	-0.349	0.147	16.8
H-charged	70	2660	0.33	167	596	0.551	0.001	0.859	0.0222	0.241	-0.524	0.077	14.6

3.3 Results and discussion

Ballistics tests were carried out at different strike velocities, ranging from 235 m s^{-1} to 506 m s^{-1}. During ballistics tests, it was tried to determine the critical velocity at which the H-uncharged specimen remained unpierced by the projectile and the H-charged specimen was pierced by the projectile. All of the experiments were carried out at room temperature. According to the ballistics test results, at velocities below 440 m s^{-1}, a full penetration of projectile was not observed on both H-uncharged and H-charged specimens. However, at the critical velocity of 440 m s^{-1}, H-uncharged specimen could withstand the given energy, whereas, H-uncharged specimen experienced full penetration, causing the projectile to pierce the plate and residual from the rear with a residual velocity of 40.17 m s^{-1}. Further tests were carried out after the critical velocity of 440 m s^{-1}. The related strike velocities for H-uncharged specimens are 458 m s^{-1}, 498,7 m s^{-1}, and 498 m s^{-1}, while those for H-charged 457 m s^{-1}, 502 m s^{-1}, and 508 m s^{-1} for H-charged specimens. Similar results were observed with the result of 440 m s^{-1} velocity threshold. Although both H-charged and H-uncharged specimens were pierced at approximately 457 m s^{-1}, notable differences in projectile residual velocities were observed. The H-charged specimen exhibited a residual velocity of 86.33 m s^{-1}, while the residual velocity for the H-uncharged specimen was 38.75 m s^{-1}. The next phase involved conducting tests at about 500 m s^{-1}. The H-charged specimen exhibited a residual velocity of 175.49 m s^{-1}, while the H-uncharged specimen exhibited a residual velocity of 77 m s^{-1}. These test results served to confirm the findings obtained in previous tests. Therefore, it was concluded that atomic hydrogen altered the ballistic performance of Al 5083 by decreasing its ductility. A transition from ductile to brittle fracture behavior in Al 5083 has previously been reported in the presence of hydrogen [68], but this is the first study that suggest HE can also be pronounced under ballistic loading. After completing the ballistics tests, the absorbed energy calculations are used to analyze and discuss the ductility values according to the input and output velocities in the ballistic studies [114,115]. The absorbed energy can be calculated with the strike and residual velocities using the Equation (3.6) below [114].

$$\frac{1}{2}mV^2 \tag{3.6}$$

The H-uncharged specimen was pierced at a strike velocity of 458 m s^{-1}, resulting in a residual velocity of 38.75 m s^{-1}. Considering the 0.00285 kg projectile weight, the

absorbed impact energy was calculated as 296.77 J. The absorbed impact energy for the H-charged specimen, with a strike velocity of 457 m s^{-1} and a residual velocity of 86.33 m s^{-1}, is 286,99 J. Compared to the H-uncharged specimen, the H-charged specimen exhibited a lower absorbed energy of 9,78 J, representing a decrease of approximately 3,3%. Another strike velocity where the effect of hydrogen was investigated is around 500 m s^{-1}. For the H-uncharged specimen with a strike velocity of 498 m s^{-1} and residual velocity of 77 m s^{-1}, the absorbed impact energy is 344.96 J. On the other hand, for the H-charged specimen with a strike velocity of 506 m s^{-1} and residual velocity of 175,49 m s^{-1}, the absorbed impact energy is 320.97 J. At approximately 500 m s^{-1}, the presence of hydrogen leads to a reduction of 23.99 J in the absorbed impact energy. This decrease corresponds to a reduction of roughly 7% compared to the H-uncharged specimen. At both strike velocities, approximately 458 m s^{-1} and 500 m s^{-1}, the H-charged specimens exhibited lower energy absorption values than their respective H-uncharged counterparts. These consistent test results demonstrate a reliable pattern or trend in our gathered data. It was reported that hydrogen does not change the ultimate tensile strength of Al 5083. However, it does impact ductility by decreasing it noticeably [68]. Indeed, based on the test results, it can be concluded that the decrease in absorbed energy absorption is directly attributed to the decreased ductility caused by the presence of hydrogen. This is because the energy that can be absorbed until the fracture or toughness is correlated with the material's ductility. Due to the hydrogen sensitivity of Al 5083, as ductility decreases, the energy that can be absorbed up to fracture also decreases accordingly [68]. Moreover, the percentage decrease in energy absorption is more pronounced at higher speeds. This indicates that HEDE may be more pronounced at more incredible speeds, which has more dominant character than HELP [22], as it will also be discussed using SEM investigations using Figure 3.9 under the microstructural analysis title.

Figure 3.6 presents the instant test moments for both H-uncharged and H-charged specimens, subjected to projectile strike velocities of 506 m s^{-1} and 498 m s^{-1}, respectively. The images were taken using a high-speed camera. The projectile, fractured specimen, and fragments are clearly visible in these images. The projectiles are highlighted in red, primary fractured parts are in yellow, and smaller fractured pieces are indicated with white arrows. According to the figures, the difference in fragment ratio between the two cases is evident and highly pronounced. The H-charged specimen exhibits a greater extent of fragmented failure when compared to the H-uncharged specimen. It is known that an increase in strike velocity triggers a transition in failure mode from dishing to plugging,

accompanied by a greater quantity of fragments compared to lower velocities [88,116]. During the ballistics test, if the target material is unable to absorb the energy, a portion of the energy is transferred through the formation of fragments [88,116]. Considering both HE and increase in deformation rate tend to decrease ductility and result in sudden fracture, our findings correspond well with this phenomenon [3].

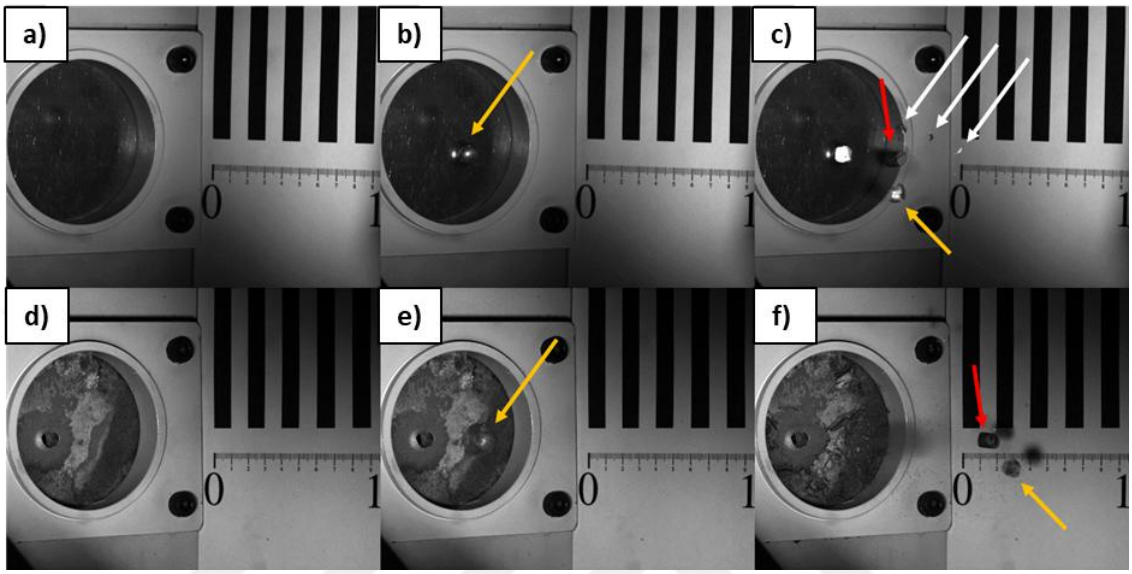

Figure 3.6 Ballistics test photographs are captured from the video taken during the test, a) to c) ballistics test of the H-uncharged specimen to which the projectile struck with 506 $m \cdot s^{-1}$, d) to f) Ballistics test of the H-charged specimen to which the projectile struck with 498 $m\ s^{-1}$.

Figure 3.7 presents all the fully penetrated test specimens after the fracture. Failure mode can change according to the shape and kinetic energy of the projectile, specimen material, and dimensions [84]. Some of these failure modes are petalling, that takes place especially in thin materials, ductile hole enlargement, bulging, spalling, fragmentation, shear plugging, and cracking [117]. The shape of the projectile influences the fracture mode [84,88]. Specifically, flat-shaped projectiles tend to induce "shear plugging" [88]. On the other hand, when it comes to “ductile hole enlargement,” it is typically associated with ogival projectiles [88,117]. "Ductile hole enlargement" exhibits a higher degree of plastic deformation due to its more significant fracture strain, resulting in increased energy absorption [88]. Conversely, "shear plugging" leads to less plastic deformation of the target material, which is considered less desirable [88]. In our study, the projectile's kinetic energy was changed by modifying velocity, and the hydrogen effect was investigated by charging hydrogen. Due to the nonflat and nonoblique shape of the MIL-DTL-46593B standard projectile with a caliber of 0.30 used in our study, it is anticipated

that a semi-mode of ductile hole enlargement and shear plugging type of fracture may occur after full penetration. Accordingly, based on Figure 3.7, it is observed that both the H-uncharged and H-charged specimens displayed a deformation pattern characterized by partial ductile hole enlargement coupled with shear plugging deformation. However, the percentage of ductile hole enlargement in the H-uncharged specimens was notably higher compared to the H-charged counterparts. This corresponds well with the kinetical energy calculations presented under the previous title. Moreover, an increase in strike velocity resulted in a partial change from ductile hole enlargement to shear plugging even in the same group of specimens because of the decreased ductility at greater deformation velocities. The effect of hydrogen and the velocity can also be concluded from Figure 3.8. According to the 3D laser scanning results, penetration of projectiles was increased with increasing velocity as expected. The other critical result is increased plastic deformation near the strike area on the H-uncharged specimens. The depth difference in the deformed region is 1.94 mm for panel (a), 2.91 mm for panel (c), 2.64 mm for panel (b), and 3.20 mm for panel (d) in Figure 3.8. Therefore, it can be deduced that increased speed led to a deeper deformed region, while H-charging resulted in a less profound fracture. This indicates that reduced ductility influenced the depth of the deformation negatively [88,116].

In addition to the depth difference, volume loss was also assessed through 3D analysis. Specifically, in H-charged specimens (Figure 3.8 a and b), the volume loss measured 49.73 mm^3 and 58.47 mm^3, respectively, whereas in H-uncharged specimens (Figure 3.8c-d), the volume loss was 28.36 mm^3 and 36.61 mm^3. These findings indicate that as ductility decreases in H-charged specimens compared to H-uncharged specimens, the material is less capable of storing energy through plastic deformation. Consequently, a more significant amount of material is lost through disintegration. In contrast, H-uncharged material retains energy due to its higher ductility, leading to a lower volume loss. These findings corroborate existing literature, demonstrating that materials with higher brittleness tend to exhibit more fragmented fractures, while more ductile materials can absorb more energy through plastic deformation [88,116]. Hence, Figure 3.7 and Figure 3.8 results parallel with each other. In other terms, full penetration and partial penetration results strengthen each other.

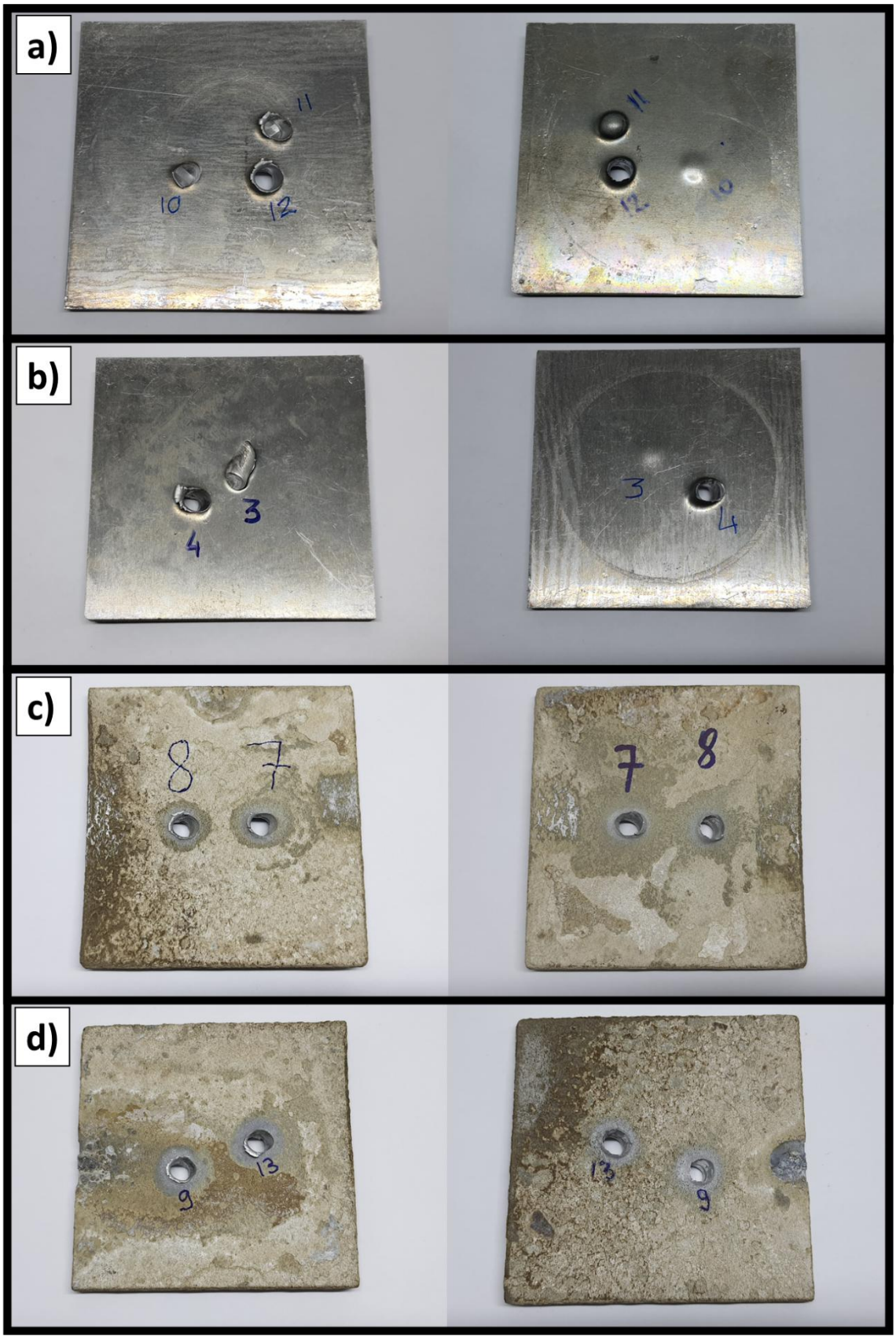

Figure 3.7 Fully penetrated test specimens, a) and b) H-uncharged specimens and c) and d) H-charged specimens.

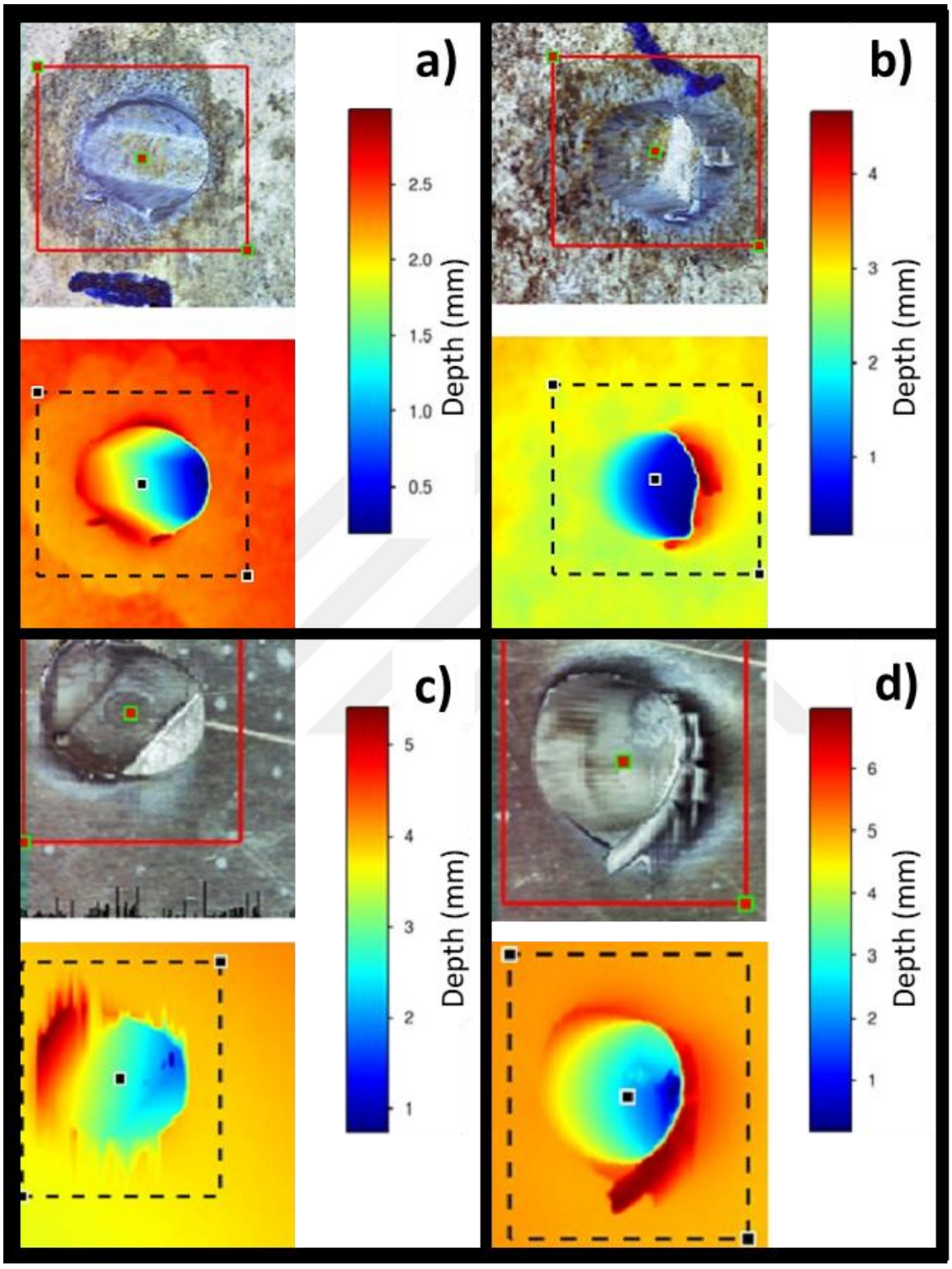

Figure 3.8 3D laser scanning images, a) and b) H-charged specimens with strike velocity of 254 m s^{-1} and 291 m s^{-1} , respectively, and c) and d) H-uncharged specimens with strike velocity of 235 m s^{-1} and 301 m s^{-1} , respectively.

After the ballistics tests, a topological examination of fracture surfaces was conducted through SEM to discern potential active HE mechanisms. In Figure 3.9, related SEM images are presented. For this investigation, specimens subjected to ballistics tests at projectile strike velocities of approximately 440 m s^{-1} and 500 m s^{-1} were selected for both H-charged and H-uncharged specimens. In Figure 3.9, panels a-c, panels d-f, panels g-i, panels j-l illustrate H-uncharged at 458 m s^{-1}, H-uncharged at 498 m s^{-1}, H-charged at 457 m s^{-1}, and H-charged at 506 m s^{-1}, respectively. Based on microstructural observations, it was noted that at lower inlet velocities, the H-uncharged specimen exhibited a ductile fracture mode, as seen in panels a-c with some discernible voids, and no cracks were observed. The voids are less evident than regular tensile tests due to the combined effect of tension, compression, and shear during projectile passage during deformation [118]. A significant portion of the material displays deformation traces in lines parallel with the projectile path. Moreover, in panel panels a-c, projectile particles draw attention; similar residues were reported before [119]. Conversely, an increase in projectile strike velocity led to the emergence of surface cracks. This serves as an indication of more brittle fracture characteristics [9]. The reason is that when the stress concentration exceeds the capacity for plastic deformation through microstructural mechanisms, the crack initiates and extends [9]. Furthermore, there are fewer projectile residues on the surface compared to the slower velocity; this can be attributed to the reduced contact time of the projectile with the surface. Compared to the H-uncharged specimen, the H-charged specimen displayed a notably more brittle fracture behavior, as evidenced by surface cracks at the 440 m s^{-1} inlet velocity level. This conclusion is drawn from comparing panels "a-c" and "g-i". The cracks on the surface are evident compared to the H-uncharged specimen. For the H-charged specimens, the increase in velocity resulted in a more brittle fracture, as presented in panels j-l like H-uncharged specimens. However, it is noteworthy that the escalation in brittle features on the surface is significantly more pronounced than the H-uncharged counterparts. This result arises from an increased portion of the surface exhibiting cracks. Hence, when contrasted with lower velocities at higher speeds, the influence of the HEDE mechanism becomes more prominent [22]. Furthermore, compared to the specimens charged with hydrogen, those uncharged exhibit fewer cracks in the region of deformation traces, appearing as lines from the projectile's passage. This difference can be attributed to the reduced deformability of the H-charged specimens.

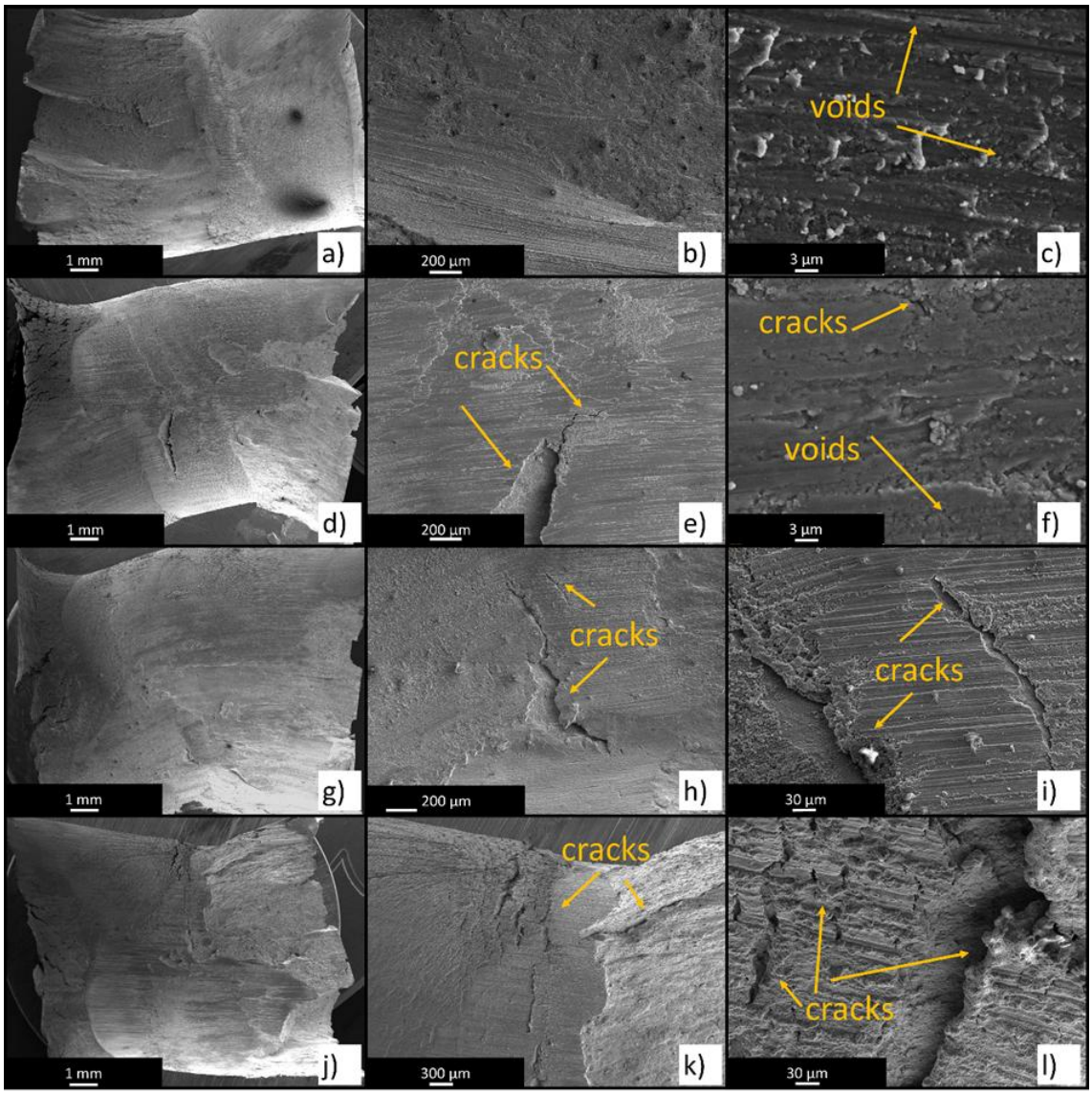

Figure 3.9 SEM images of fracture surfaces, a)-c) and d)-f) belongs to H-uncharged specimens with strike velocity of 458 m s^{-1} and 498 m s^{-1}, respectively and g)-i) and j)-l) belong to H-charged specimens with strike velocities of 457 m s^{-1} and 506 m s^{-1}, respectively.

The finite element model for ballistic test simulation comprises a projectile and a plate. The projectile is modelled as a discrete rigid body to optimize computational efficiency, assuming a rigid response. On the other hand, the plate is modelled as a deformable body meshed using the Abaqus reduced-integration continuum three-dimensional brick (C3D8R) element. A mesh refinement study has been conducted on the plate to determine the most efficient element size that balances solution accuracy and computational time. An unstructured discretization with a suitable partitioning technique has been employed to achieve a finer mesh in the areas where the projectile strikes.

A predefined velocity field has been applied on the rigid projectile, allowing for the computation of residual velocity based on energy balance. A concentrated mass of 2.85 gr has been assigned to the rigid projectile body, and translational constraints in the x, y, and z directions have been enforced on the plate's lateral faces. It is worth noting that the plate has been inclined at a 30° angle with respect to the projectile trajectory to accurately replicate the real ballistic test conditions.

A series of finite element simulations are performed to evaluate the predictive capabilities of the finite element model and the optimization-based parameter identification procedure. The simulation results are compared to the experimental data obtained from the ballistic test experiment in Figure 3.10. The analysis shows that the finite element simulations can accurately replicate ballistic test results under various impact velocities based on a strong agreement between simulated and experimental data. Factors like model assumptions, boundary conditions, and experimental variability may explain the slight differences observed when simulation velocities were compared with experimental velocity.

Figure 3.10 compares the simulated and experimental data for the H-charged plate and demonstrates a close match across the entire range of impact velocities. The results reveal that the developed finite element model can accurately simulate the ballistic test on the H-charged plate with various impact velocities. The good correlation between the simulation and experimental data for the H-charged plate further signifies the effectiveness of the optimization-based inverse approach in identifying the Johnson-Cook damage parameters. This approach may provide a reliable alternative for the parameter identification of materials and minimize the reliance on expensive and time-consuming experimental tests, making it an efficient and economical solution. Although further validations for various test conditions and loading scenarios would enhance the versatility of the proposed inverse parameter identification setting, it is outside the scope of the current study and can be considered as future work.

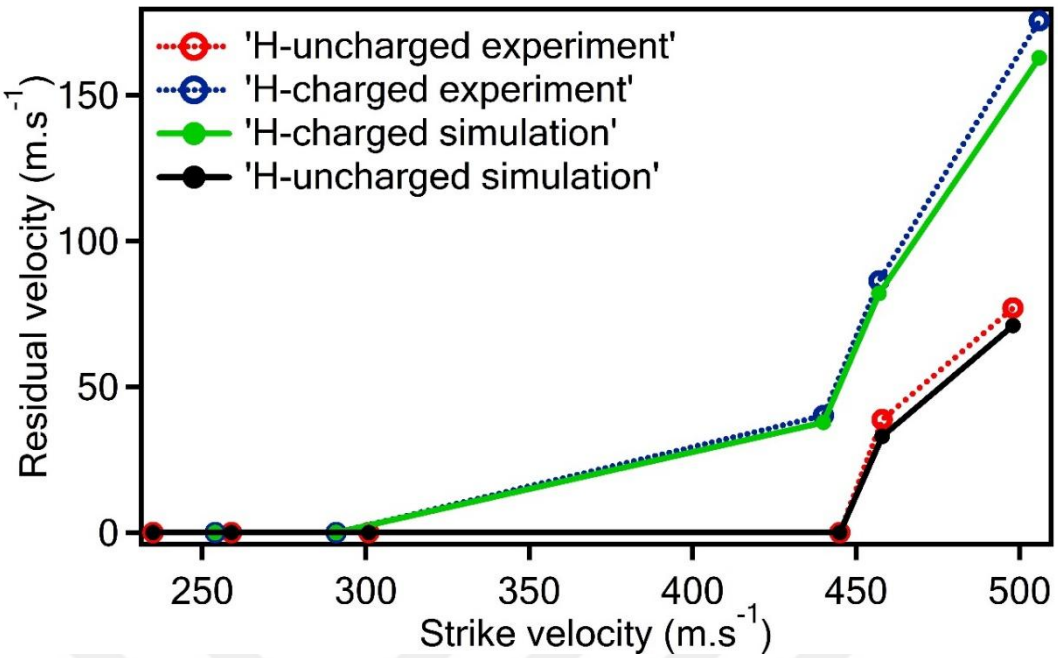

Figure 3.10 Projectile strike versus residual velocity graph of ballistics tests.

To provide valuable insight into the distribution and extent of material damage, further investigations are carried out by demonstrating the contour of damage variable D in the H-uncharged and charged plates at various velocities. The damage variable D, as a function of plastic deformation, quantifies progressive material degradation on a scale of 0-1. Damage variable D can be crucial for determining the onset and accumulation of damage during plastic deformation, which results in material softening, reduced strength, or potential failure. This variable is particularly significant in capturing degradation behavior under high strain rates, accounting for the influence of strain rate and stress triaxiality on the material's resistance to deformation before failure. Figure 3.11a-f illustrate the spatial distribution and severity of material damage in the H-uncharged and H-charged plates at different velocities, enabling an assessment of structural integrity and identification of vulnerable regions.

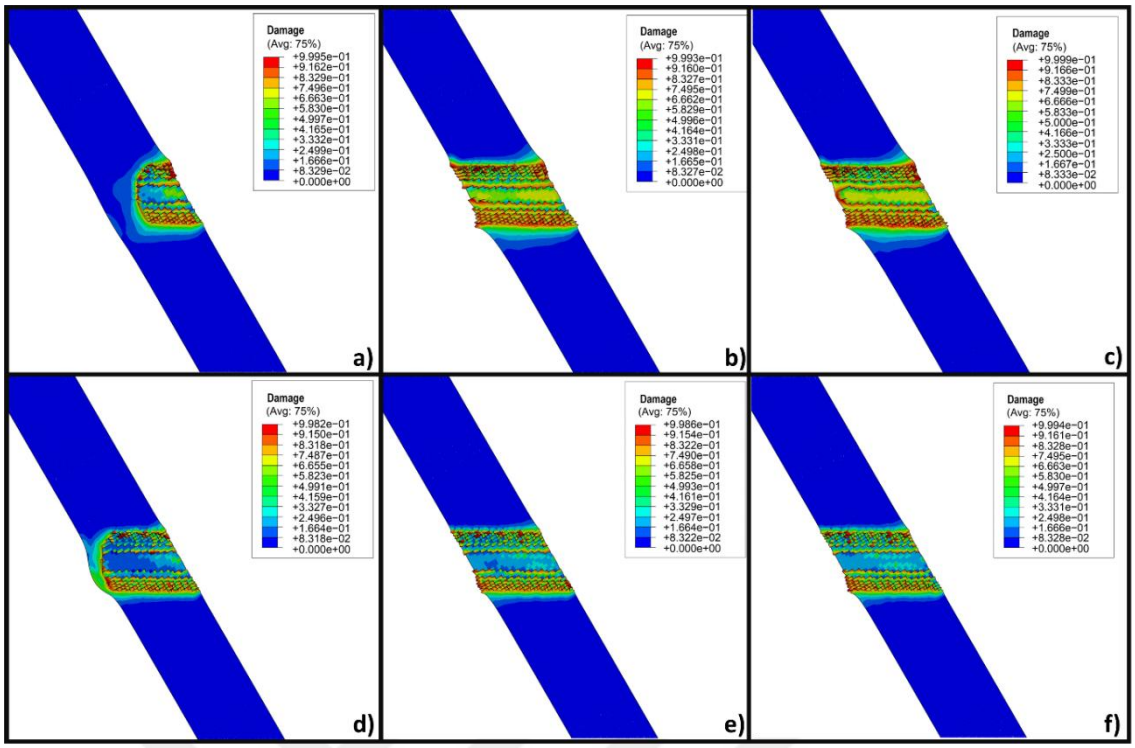

Figure 3.11 Damage contour at midplane section for H-uncharged plate at impact velocities of a) 445 m s^{-1}, b) 458 m s^{-1}, and c) 498 m s^{-1}, and H-charged plate at impact velocities of d) 291 m s^{-1}, e) 440 m s^{-1}, and f) 506 m s^{-1}.

3.4 Conclusions

This study conducted an extensive investigation into the susceptibility of Al 5083 to HE under ballistics tests. The experimental phase involved an electrochemical hydrogen charging process introducing hydrogen into the material. H-uncharged and H-charged materials were subjected to standardized ballistics testing according to MIL-DTL-46593B. Subsequently, the fracture and penetration surfaces were analyzed using SEM and 3D laser scanning techniques. From the work presented herein, the following conclusions can be drawn:

- HE can be pronounced at an ultra-high strain rate.
- According to the 3D laser scanning results, partially penetrated H-charged specimens exhibited more volume loss, attributed to their lower ductility. Additionally, the instant camera results showed more fragmentation on H-charged specimens after full penetration. These consistent results are attributed to HE.
- As the ballistic speed increases, the dominant HE mechanism shifts from HELP to HEDE.
- A numerical model has been introduced, utilizing the Johnson-Cook plasticity model alongside its failure criteria, to simulate the ballistic behavior and failure of AL 5083

H131 in the presence of hydrogen susceptibility. An efficient inverse optimization-based approach has been developed to calibrate the material parameters for the hydrogen-susceptible material. Based on a comparative study, it has been concluded that this modeling framework enables an accurate prediction of the ballistic behavior of both H-uncharged and H-charged AL 5083 H131.

Research Funding

B. Bal acknowledges the financial support by the Scientific and Technological Research Council of Turkey (TUBITAK) BIDEB-2219 Postdoctoral Research Program under Project No. 1059B192000774.

Chapter 4

A Phenomenological Hydrogen Induced Edge Dislocation Mobility Law for BCC Fe Obtained by Molecular Dynamics [120]*

*This study has been published on International Journal of Hydrogen Energy and the content has been reprinted under permissions of journal.

Abstract

Investigating the interaction between hydrogen and dislocations is essential for understanding the origin of hydrogen-related fractures, specifically hydrogen embrittlement (HE). This study investigates the effect of hydrogen on the mobility of ½<111>{110} and ½<111>{112} edge dislocations in body-centered cubic (BCC) iron (Fe). Specifically, molecular dynamics (MD) simulations are conducted at various stress levels and temperatures for hydrogen-free and hydrogen-containing lattices. The results show that hydrogen significantly reduces dislocation velocities due to the pinning effect. Based on the results of MD simulations, phenomenological mobility laws for both types of dislocations as a function of stress, temperature and hydrogen concentration are proposed. Current findings provide a comprehensive model for predicting dislocation behavior in hydrogen-containing BCC lattices, thus enhancing the understanding of HE. Additionally, the mobility laws can be utilized in dislocation dynamics simulations to investigate hydrogen-dislocation interactions on a larger scale, aiding in the design of HE-resilient materials for industrial applications.

4.1 Introduction

Hydrogen embrittlement (HE) is a phenomenon where the presence of hydrogen in metallic materials leads to unexpected failures [121]. HE remains a persistent issue affecting a wide range of industrial applications, ranging from cars, aviation, oil & gas storage and transportation systems, to high-strength materials for infrastructure applications [113,122–127]. The reason is that HE leads to a deterioration of the mechanical properties of metals, both during their manufacturing and while in use [2,128]. From a variety of sources in the environment, and due to the easy absorption of hydrogen into the crystal lattice of most metals, the prevention of HE constitutes a great challenge to the materials scientist and engineer [129]. It is well-known that the degree of HE is sensitive to a variety of mechanical, environmental and material related factors [2,4–6], with sometimes rather complex outcomes and dependencies. For instance, when decreasing the strain rate one would expect that the effect of foreign atoms like hydrogen on the properties of the material should be weaker, but such a decrease also allows more time for hydrogen-dislocation interactions to take place, and thus often increases the effective susceptibility of the material to HE [40,130,131]. In addition, the susceptibility

of HE usually grows with the mechanical strength of a material, often in a roughly linearly fashion [132]. The effect of these 3 main factors, material, mechanical, environmental on the HE susceptibility of different materials is well-studied [2–4]. However, these studies mostly focus on the changes in the mechanical properties on a macroscopic level. In order to better understand the underlying atomic and mesoscopic mechanisms of HE, it is necessary to work on different time and length scales.

There are various experimental and numerical studies in literature that aim to understand the nature of HE at the atomic scale, and as a result of these studies, different mechanisms of HE have been proposed [4,133]. Among these mechanisms, hydrogen enhanced localized plasticity (HELP) and hydrogen enhanced decohesion (HEDE) have become the most widely accepted HE mechanisms by the researchers [22–26,130]. HELP states that hydrogen shields the elastic stress field of dislocations and thus increases the mobility of dislocations and cause localized plasticity [4,134]. In contrast, HEDE suggests that hydrogen within the lattice reduces the cohesive strength of the metal-metal and therefore promotes crack growth finally resulting in mechanical [4]. For many years, the formation mechanism of HE has been debated, and it has generally been assumed that intergranular fracture in systems that do not form hydrides is due to HEDE [4,135]. However, based on subsequent experimental observations, it has been argued that dislocation plasticity and, therefore, HELP plays a much more significant role as an HE mechanism [136]. In the last decade, it has been demonstrated that both of these mechanisms can be activated individually or simultaneously under different conditions [22–26,130]. Despite these extensive studies, the exact mechanism of HE still remains unclear [137]. Thus, to understand the nature of HE, interactions between hydrogen and dislocations at both atomic and mesoscopic scales need to be further analyzed, ideally on the quantum mechanical level.

Employing ab initio simulations performed at the atomic level, various problems have been investigated in the past, such as the segregation of hydrogen to interfacial regions [138], hydrogen-vacancy interactions [139], diffusion of hydrogen in different metal phases [140], and the thermodynamics of hydrogen solubility [141]. However, due to the limited number of atoms that can be studied on the ab initio level, dislocation-hydrogen interactions cannot be observed on relevant time scales, and thus this type of modelling is limited in its explanatory power regarding the atomic mechanisms underlying HE. Molecular dynamics (MD) studies using empirical, semi-empirical or effective potentials have been conducted to examine the atomic origin of HE. These

include the investigation of processes such as hydrogen diffusion and localization within the lattice, and of the effects of hydrogen on macroscopic mechanical properties, microstructure, surface energy and dislocation velocity [133]. From various studies, also showing controversial results, it was observed that presence of hydrogen decreased the velocity of edge dislocations; however, once the dislocation speed is decreased hydrogen can also enhance the dislocation's velocity and promote the HELP mechanism [133,142,143]. Similarly, a high hydrogen concentration impedes kink-pair nucleation and migration and decreases the velocity of a screw dislocation, while a low concentration of hydrogen promotes kink-pair nucleation and migration and therefore enhances the mobility of screw dislocations [144]. However, to the best of the authors' knowledge, no study reveals the effect of hydrogen on the mobility laws of dislocations. Since the dislocation mobility plays a crucial role in dictating various aspects of plastic deformation, knowing the precise impact of hydrogen on dislocation mobility is of utmost significance in comprehending the nature of HE [133].

Slip takes place within face-centered cubic (FCC) metals on close-packed {111} planes and <110> directions [145]. Low lattice resistance of FCC and planar core structure of edge dislocation results in dislocation glide being regulated solely by the applied shear stress [99]. This suggests that, the mobility laws for FCC systems should adhere to Schmid's law [99]. In contrast, dislocations experience a great amount of lattice resistance in body centered cubic (BCC) metals [99]. In BCC metals, slip mostly occurs on {110} and {112} planes and <111> directions [145]. When the dislocation velocity is much smaller than the shear wave speed, interaction of phonons with dislocations is the dominant activation mechanism of edge dislocations [146]. Therefore, in BCC crystal systems edge dislocations still move very rapidly via phonon drag, and thermally activated motion of screw dislocations dominates the plastic deformation [99,146]. In the literature, ½<111>{110} and ½<111>{112} edge dislocation mobility laws in BCC systems have been studied [146–148] and phenomenological dislocation mobility laws for BCC have been proposed for both edge and screw dislocations [99]. In these studies, three main effects were observed: 1) The mobility laws assume that the velocity of dislocation is linearly proportional to the applied stress [99]. In the supersonic region, the dislocation velocity becomes equal to the speed of sound, as relativistic effects and dissipation mechanisms are neglected [99], 2) The drag coefficient of the mobility laws depends only on the type of dislocation and the temperature [99,146]. Finally, 3) the motion of the ½<111>{110} type of edge dislocation is very fast, and the nucleation of

kinks is a-thermal [146]. Therefore, this type does not contribute to plastic flow to any large degree [146]. On the other hand, ½<111>{112} dislocations exhibit both phonon drag and thermally activated regimes, and thus contribute noticeably to the plasticity of materials [146]. As a consequence, screw dislocations are the dominant dislocation type for plastic flow [146]. However, when hydrogen diffuses into the lattice, it tends to concentrate around edge dislocations and decrease their elastic energy [149]. This might make the system more likely to promote plastic deformations over screw dislocations [149]. To clarify this issue and in order to understand the atomic origin of HE in BCC structures, MD simulations of hydrogen-free and hydrogen-containing lattices are needed. Furthermore, the effect of hydrogen on the drag has to be analyzed, such that the laws that govern the corresponding hydrogen enhanced mobility can be developed. Up to now, there is only one study in literature addressing this issue [150]. In that study, hydrogen enhanced mobility law of screw dislocation has been proposed [150]. However, that investigation did not involve any MD simulations; instead Kinetic Monte Carlo (KMC) simulation were performed and only screw dislocations were studied. To our knowledge, there is currently no existing literature that explores the mobility law of edge dislocations under the influence of hydrogen.

In the present study, the effects of hydrogen on the mobility laws of edge dislocations have been investigated for ½<111>{110} and ½<111>{112} dislocations in α-Fe. For this purpose, MD simulations of length 1 ns were conducted for lattices both without and with hydrogen. The simulations for ½<111>{110} dislocations were carried out using 4 different hydrogen concentrations (%0 H/Fe, %0.1 H/Fe, %0.25 H/Fe and %0.5 H/Fe) and 5 different temperatures (50 K, 100 K, 200 K, 300 K and 400 K); in addition, for pure iron (%0 H/Fe), simulations at a temperature of 500 K were performed. On the other hand, the simulations for ½<111>{112} dislocations were conducted at 5 different temperature values (100 K, 200 K, 300 K, 400 K and 500 K) for (%0 H/Fe, %0.1 H/Fe, %0.25 H/Fe and %0.5 H/Fe) hydrogen concentration values. The effect of hydrogen on the measured stress and displacement as function of time and velocity-stress relationship for both hydrogen-free and hydrogen-containing lattices have been investigated. It was observed that hydrogen impeded the movement of dislocations. Furthermore, a formula for the effect of hydrogen on the drag coefficient has been developed, and corresponding closed-form laws for the hydrogen enhanced mobility have been obtained. These mobility laws then can be used for discrete dislocation dynamics simulation in order to investigate hydrogen-dislocation interactions at micro scale.

4.2 Method

The MD simulations were performed using the LAMMPS (Large-scale Atomic/Molecular Massively Parallel Simulator) code. The simulations employed the embedded atom method (EAM) potential presented by M. Wen [151]. The potential effectively defines the interatomic potentials of H-H and Fe-H in the α-Fe structure, encompassing H-dislocation interactions and other defects [151]. This potential yields more reliable results than the Mendelev potential [152] for the simulation of hydrogen rich cells since it captures the repulsive effect of H-H interactions below 0.45 Å, that cannot be accounted for by the Mendelev potential. The hydrogen concentrations were selected as %0 H/Fe, %0.1 H/Fe, %0.25 H/Fe, and %0.5 H/Fe and the effects of the hydrogen concentration on the mobility of ½<111>{110} and ½<111>{112} edge dislocations were investigated under shear loading. The cell dimensions were specified as 29.6 nm × 20.2 nm × 28.3 nm. These dimensions were chosen for the following reasons: 1) The X-axis was long enough to allow activation of the kink-nucleation mechanisms, 2) the length of the Y-axis was chosen to minimize the image forces along the glide plane, 3) the length of the Z-axis was chosen to ensure the distribution of mechanical work done during dislocation slip, indirect heat production without the periodic boundary conditions being met, and 4) to be compatible with the literature [146] as far as similar calculations have been performed. Within this simulation cell, about 1.5 million Fe atoms were employed for the pure case (%0 H/Fe). All simulations were conducted using PPS (Periodic-Periodic-Shrink) boundary conditions in the x, y, and z axes. Along the x and y axes, periodic boundary conditions were applied to facilitate dislocation motion, while along the z-axis, a shrink-wrapped boundary condition was employed to maintain atoms at their specified positions. The simulations were conducted using the NVE (number of atoms, volume, and energy constant) ensemble and Langevin thermostat was employed to control the temperature within the region delineated by two layers in Figure 4.1. In particular, whole MD simulation consists of many short pieces of NVE-type parts, between these one periodically adjusts both the volume and temperature, in order to keep the pressure and temperature at or close to the prescribed values. The configuration efficiently conserved enthalpy during the simulation, as given by H=E+pV. Figure 4.1 illustrates the x, y, z axes, the initial position of the dislocation, the glide plane, the fixed atom layer, and the volume where the shear force was applied. In this configuration, hydrogen atoms were initially randomly placed but only up to a certain

distance (7,1 nm) to the endpoints along the z-axis, in order to prevent hydrogen accumulation in these regions. Supplementary Figures 1 and 2 illustrate the effect of relaxation time on hydrogen distribution. The results indicate that longer waiting does not alter the hydrogen distribution, with a random distribution of hydrogen atoms consistently observed. Supplementary Figures 3 through 16 illustrate that the distribution of hydrogen, both before and after relaxation, does not concentrate at the dislocation core and remains random at various hydrogen concentrations and temperatures. Additionally, during the motion of dislocation, hydrogen distribution is random as indicated in Supplementary Figures 17 through 19. As far as the placement of the hydrogen atoms in the x and y directions was concerned, no restrictions were employed. Thus, the (x,y,z) coordinates of the hydrogen atoms could take on random values within the lengths of Lx, Ly, Lz/2, and the allowed region where hydrogen was added constitutes half of the total cell volume. Of course, during the subsequent simulations, the hydrogen atoms moved into the previously hydrogen empty region of the simulation cell. The simulation cells underwent minimization before load applications, with a defined output time step of 0.2 ps. The systems were minimized until reaching equilibration temperatures of 50 K, 100 K, 200 K, 300 K, 400 K, and 500 K for all simulations. As depicted in Figure 4.1, the simulation cell comprises three distinct regions. The first one, presented in blue, is where shear stress was applied. The shear stress is applied in the x-axis direction. The black region represents the fixed atom layers. The glide plane is presented in green, and the dislocation exhibits motion on this plane in the x-direction and the edge dislocation takes place in y axis. All atoms in the uncolored regions are free to move in response to the shear stress. The dislocations have a planar core structure. The simulations were conducted for a duration of 1 ns with a timestep of 1 fs. This time step is widely reported in the literature [153–162]. Subsequent to the MD simulations, the systems were visualized using OVITO software [163], and the dislocation's mobility was analyzed using the Dislocation Extraction Algorithm (DXA) [164]. Moreover, atomic stress calculations were conducted via the virial stress theorem.

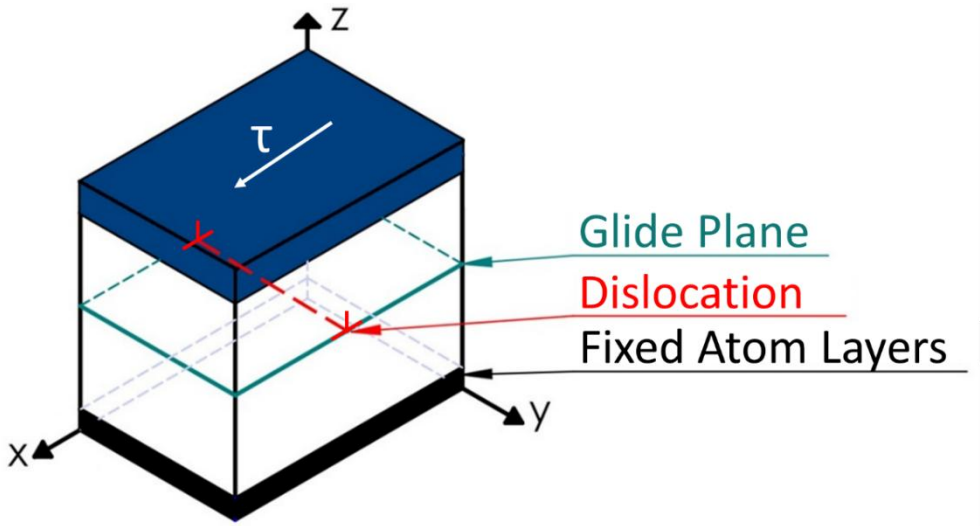

Figure 4.1 Representative schematic of Simulation Cell. (unit: nm).

4.3 Results and Discussion

4.3.1 Edge Dislocation Mobility on (110) Plane

Figure 4.2 displays stress vs. time graphs of simulations at 100K temperature, encompassing pure iron, %0.1 H/Fe concentration, %0.25 H/Fe concentration, and %0.5 H/Fe concentration on (110) plane. All the simulations were conducted stress-controlled to minimize the stress fluctuations inside the simulation cell [165]. Additionally, stress-controlled simulations give dislocation velocities that are not bound to a specific strain rate, as the velocity calculations in these circumstances are unaffected by the size of the simulation box utilized. Notably, there is an increase in stress values until 0.5 ns. This increment is attributed to the fact that the stress was gradually raised from 0 MPa to the desired stress value during this period. Subsequently, between 0.5 ns and 1 ns, the stress values stabilize in comparison to the initial stages. The applied stress values from the upper part of the cell were higher than the corresponding graphic stress values, except for the stresses where dislocation motions could not be observed. Due to friction and the loss of energy caused by atom motion in the system, some of this stress value is consumed, resulting in a decrease in the observed stress values in the graphs. Another result is that periodic fluctuations in stress values in hydrogen-free simulations start at lower stress levels compared to those in hydrogen-containing simulations. The reason behind this is that we could not observe any sustained motion under fluctuating stress values, but just some vibration-like motion of the dislocation. Starting from fluctuated stresses, the

dislocation starts its motion. After the motion becomes stable, the stress also becomes stable; hence, the region of lower stress shortly before stable dislocation movement was considered as the transition region. The result can be interpreted in the following way: if the stress value is just large enough for initiating the motion of the dislocation, stress fluctuations become dominant, but if the stress value is greater than this value, the stress fluctuations decrease and the movement of the dislocation becomes smooth. Moreover, due to the dislocation pinning effect of hydrogen [133], the transition occurs at greater stresses with the addition of hydrogen to pure iron and our results agree well with literature [166,167]. This clearly shows the effect of hydrogen on the system dynamics. Figure 4.2 presents simulations at 100 K, while the results for other temperatures can be accessed in Supplementary Figures 20 through 23.

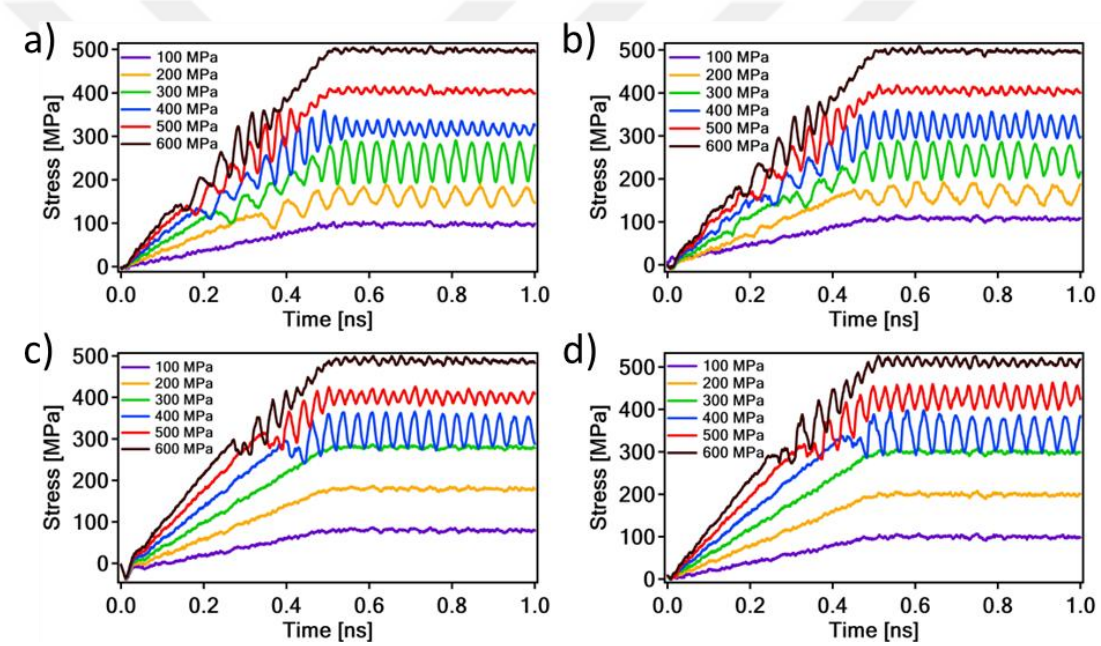

Figure 4.2 Stress vs time graphs of 100K temperature for (110) plane. Here, a) shows the pure iron case (%0 H/Fe), b) shows %0.1 H/Fe concentration, c) shows %0.25 H/Fe concentration d) shows %0.5 H/Fe concentration

Figure 4.3 shows the dislocation core displacement vs time graphs of the hydrogen free lattice at temperatures at 50K, 100K, 200K, 300K, 400K and 500K temperatures. It can be observed that increasing stress values resulted in greater displacement. It had been previously reported that the migration of an edge dislocation on (111) plane occurs without any kink formation and alteration of the core structure in the absence of hydrogen [168]. In addition, the motion of an edge dislocation is not thermally activated; instead, phonon drag is the main mechanism of the edge dislocation glide [146]. Therefore, dislocations could move at low stress values in the absence of hydrogen, and our results

correspond well with previous studies in the literature [146]. At low applied stress values, the lattice resistance could affect the dislocation motion (Fig 3d-f at 100 MPa) but at higher stress values the lattice resistance is mostly insignificant and the displacement vs time relation becomes linear. Therefore, dislocation velocities at each temperature and applied stress can be extracted from linear fits to the second half of the displacement vs time curves. Figure 4.3 presents simulations of hydrogen-free cases at different temperatures and stress values, while the results for hydrogen-containing lattices can be accessed in the Supplementary Figures 24 through 26.

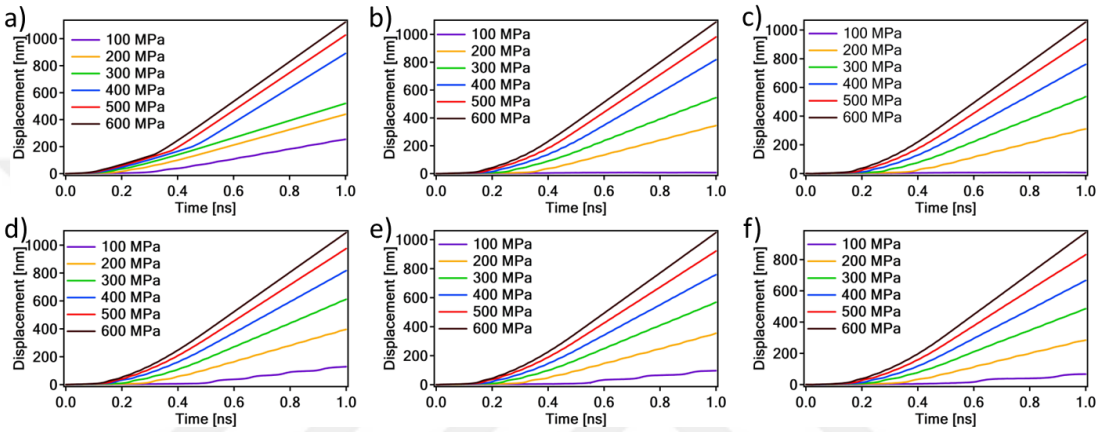

Figure 4.3 Displacement vs time graphs of pure iron simulations. Here, starting from a) to f), graphs show the simulation results of 50K, 100K, 200K, 300K, 400K, 500K correspondingly.

Figure 4.4a. presents the velocity of dislocation in the hydrogen-free lattice as a function of the applied stress at different temperatures, where, in general, the velocities increase monotonically with applied stress. It can be observed from Figure 4.4a that the velocity of an edge dislocation increases in an approximately linear fashion with the applied stress and monotonically decreases with temperature. This behavior is attributed to phonon drag dynamics, and our results are consistent with those in the existing literature [146,165]. In particular, for a velocity of dislocation small compared to the speed of sound in a metal lattice, phonon-dislocation interactions provide a drag force that is approximately nearly proportional to the dislocation speed [99]. At higher temperatures, phonons can interact more effectively with defects such as dislocations within the crystal structure [169–171]. This increased interaction can hinder dislocation mobility, thereby decreasing overall dislocation mobility in the material [169–171]. Figure 4.4b through 4f show the effect of hydrogen on the dislocation velocity in hydrogen-free and hydrogen-containing lattices at 50K, 100K, 200K, 300K and 500K. At

all temperatures, the velocity of dislocation is linearly proportional to the applied stress and the pure iron systems exhibit higher dislocation velocity values compared to the simulations with non-zero hydrogen concentration. It has been previously reported that dislocation velocity increases at higher stress values [146]. In addition, an increasing hydrogen content resulted in a lower dislocation velocity at all temperatures. Table 4.1 summarizes whether the dislocation is glissile (mobile) or sessile (immobile) at a given temperature and applied stress. These results clearly indicate the pinning effect of hydrogen. Specifically, if the speed of dislocation is higher than the hydrogen diffusion rate, hydrogen atoms/clusters act as a barrier to the motion of dislocation and decrease its mobility [172]. If the speed of dislocation is comparable to the hydrogen diffusion rate, hydrogen atoms/clusters can be swept at the core of the dislocation [172]. During this synchronized motion of dislocation with hydrogen, hydrogen can shield the stress field of dislocation and increase its mobility (HELP mechanism). For the transition speeds, one can observe the pinning of the dislocation by hydrogen, depinning and being caught up by hydrogen again [172]. In our simulations, the speed of dislocation is always greater than the hydrogen diffusion rate; therefore, the pinning effect of hydrogen was observed, and our results correspond well with the literature [133,142,173]. Even at higher temperatures, the effect of hydrogen on the dislocation mobility is dominant. For instance, the dislocation motion could be activated at 200 MPa for all hydrogen concentrations at 50K, while 300 MPa, 600 MPa and 1000 MPa were required to activate the edge dislocation core at 400K for 0.1% H/Fe, 0.25% H/Fe and 0.5% H/Fe hydrogen concentrations, respectively. Therefore, increasing both the hydrogen concentration and the temperature increases the critical stress level required to mobilize the edge dislocation core for a motion.

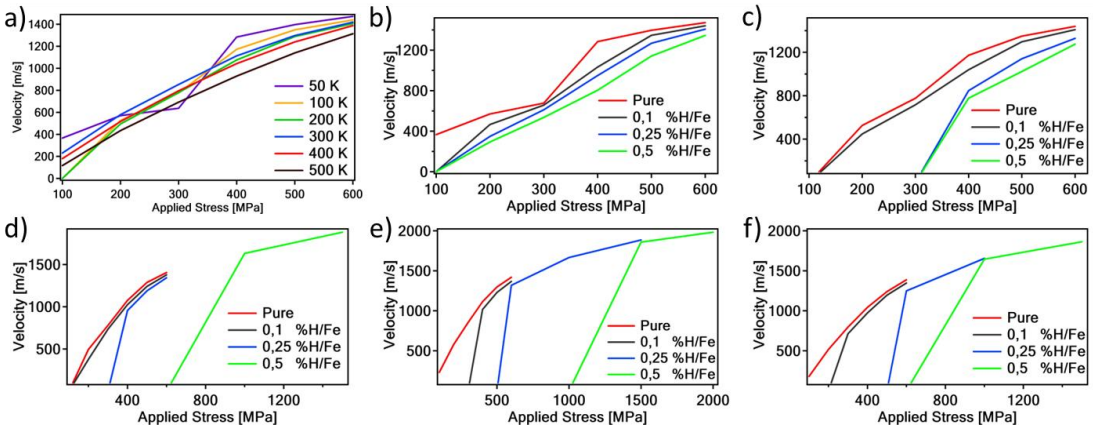

Figure 4.4 Stress vs dislocation velocity graphs of a) Pure iron cell simulation results at different temperatures, b) Hydrogen-induced lattice at 50K, c) Hydrogen-induced lattice at 100K, d) Hydrogen-induced lattice at 200K, e) Hydrogen-induced lattice at 300K, f) Hydrogen-induced lattice at 400K temperature.

Table 4.1 Effect of hydrogen on the dislocation mobility. g: glissile dislocation, s: sessile dislocation, N/A: Not available.

	100 MPa					**200 MPa**				
H/Fe (%)	**50 K**	**100 K**	**200 K**	**300 K**	**400 K**	**50 K**	**100 K**	**200 K**	**300 K**	**400 K**
0	g	s	s	g	g	g	g	g	g	g
0.1	s	s	s	s	s	g	g	g	s	s
0.25	s	s	s	s	s	g	s	s	s	s
0.5	s	s	s	s	s	g	s	s	s	s
	300 MPa					**400 MPa**				
H/Fe (%)	**50 K**	**100 K**	**200 K**	**300 K**	**400 K**	**50 K**	**100 K**	**200 K**	**300 K**	**400 K**
0	g	g	g	g	g	g	g	g	g	g
0.1	g	g	g	s	g	g	g	g	g	g
0.25	g	s	s	s	s	g	g	g	s	s
0.5	g	s	s	s	s	g	g	s	s	s

In the literature, for the hydrogen-free lattice, the dislocation velocity as a function of applied and critical stress, drag coefficient and burgers vector is typically written as Eq.4.1, denoted as the mobility law [146]. In eq. 4.1, v is the dislocation velocity, τ is the resolved shear stress, that is the difference between applied shear stress and critical stress ($\tau = \tau_{app} - \tau_{critical}(T, c)$), b is burgers vector and B(T) is the drag coefficient, where T is the temperature and c is the hydrogen concentration [99]. Critical stress is the very first stress that activates the dislocation motion. For a hydrogen-free lattice, the lattice resistance for an edge dislocation is very low and the applied stress can be regarded as the resolved stress consistent with a phonon drag mechanism. Therefore, the mobility law for a hydrogen-free lattice has been formulated using $B(T) = B_0 + B_1 T$ in the equation. According to our pure α-iron simulation results, B_0 is 10^{-4} [Pa*s] and B_1 is $4*10^{-9}$ [Pa*s/K]. These constants are quite close to the values that are reported by G. Po, et al [99] who determined B_0 as $4.26*10^{-4}$ [Pa*s] and B_1 as $8.7*10^{-7}$ [Pa*s/K] and S. Queyreau, et al, where B(T) value was determined as $6.7*10^{-7}*T$ [Pa*s] [146].

$$v = \frac{\tau b}{B(T)} \tag{4.1}$$

In the current study, the drag coefficient depends on both temperature and the hydrogen content and the resolved stress is not equal to the applied stress for the lattice containing hydrogen, and mobility law was formulated using Eq.4.2 and Eq.4.3 below. Critical stresses were determined from stress-time responses for all conditions and the drag coefficients of hydrogen-induced lattices were calculated by dividing the difference between applied stress and critical stress by the dislocation velocity (Figure 4.4) by means of Eq.4.3 for all hydrogen concentrations at different temperatures. Supplementary Figures 27 represent the relationship of difference between applied and critical stress and velocity of dislocation at different temperatures. These figures were used to derive drag coefficients for hydrogen-induced lattices. The results are given on a logarithmic scale.

Figure 4.5a shows the relationship between temperature and the drag coefficient at different hydrogen concentration values. The drag coefficient increases with both temperature and hydrogen concentration. Since there is an approximately linear relationship, the hydrogen and temperature dependent drag coefficient can be formulated as Eq.4.2 and the phenomenological hydrogen induced dislocation mobility of an edge dislocation can be formulated as Eq.4.3:

$$B(T,c) = B_0(c) + B_1(c) * T \tag{4.2}$$

$$v = \frac{(\tau_{app} - \tau_{critical}(T,c))b}{B(T,c)} \tag{4.3}$$

Figure 4.5b and 5c show hydrogen concentration vs B_0 and hydrogen concentration vs B_1 graphs, respectively. They are also linearly proportional with one another via straight line. Therefore, $B_0(c)$ and $B_1(c)$ can be expressed for low hydrogen concentrations as:

$$B_0(c) = B_2 * c + B_3 \tag{4.4}$$

$$B_1(c) = B_4 * c + B_5 \tag{4.5}$$

Here, the values for B_2-B_5 were calculated from linear fits to the plots in Figure 4.5b and 5c and are listed in Table 4.2. The drag coefficient of the hydrogen-containing lattice can be found for any hydrogen concentration and any temperature using these parameters (Table 4.2) and equations (Eqs.4.2, 4.4, 4.5).

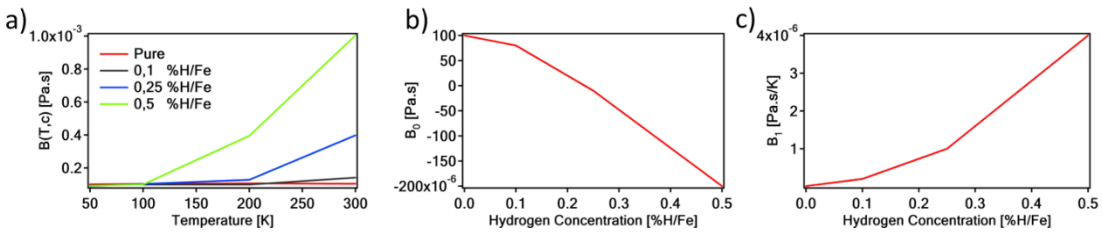

Figure 4.5 Temperature vs Drag coefficient change.

In order to complete the phenomenological description of the hydrogen induced dislocation mobility of an edge dislocation the dependence of the critical stress as function of hydrogen concentration and temperature should also be investigated and cast into a simple analytical expression. Figure 4.6a shows the change of the critical stress values according to the given hydrogen concentrations. The critical stress, that activates the dislocation motion, increases monotonically with both temperature and hydrogen concentration. As there is a roughly linear relationship between these two (Figure 4.6a), the hydrogen and temperature dependent drag coefficient can be described to a first approximation according to Eq.4.6.

$$\tau_{critical}(T, c) = A_0(T) + A_1(T) * c \tag{4.6}$$

Figure 4.6b presents the dependence of A_0, the critical shear stress at zero hydrogen concentration, on temperature. The change in A_0 is clearly not monotonic with respect to the employed temperature; therefore, it was considered constant in the temperature interval from 50K to 400K, where we computed the average value of $A_0(T)$ within for all temperatures and assigned this value to be the constant value A_0 in equation 4.6, given in Table 4.2. Figure 4.6c presents the dependence of A_1, the slope of hydrogen concentration – critical stress response, on temperature. Again, the increase with temperature is not monotonic, but shows a roughly overall increase. For the purpose of equation 4.6, A_1 was assumed to change linearly with the given temperature values and thus was essentially interpolated using Eq. 4.7. From the linear fit to Figure 4.6c, A2, the slope of the fit, and A3, the constant of the equation, were extracted and are given in Table 4.2.

$$A_1(T) = A_2 * T + A_3 \tag{4.7}$$

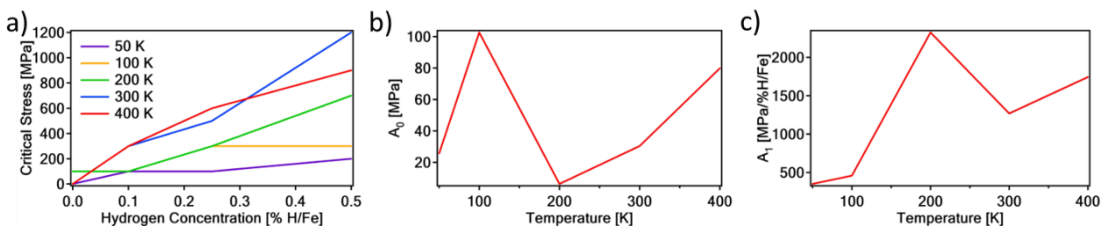

Figure 4.6 Hydrogen concentration vs critical stress values for the {110} glide plane. a) presents the change of critical stress value according to the given hydrogen concentration, b) presents the change of A_0 and c) presents the change of A_1 according to the given temperature.

Table 4.2 provides all the values necessary to determine the phenomenological hydrogen-induced ½<111>{110} edge dislocation mobility law.

Table 4.2 A and B values for the dislocation mobility of {110} glide plane.

B_2 [Pa*s/(%H/Fe)]	B_3 [Pa*s]	B_4 [Pa*s/(K*%H/Fe)]	B_5 [Pa*s/K]	A_0 [MPa]	A_2 [MPa/(K*%H/Fe)]	A_3 [MPa/%H/Fe]
$-6*10^{-4}$	$1*10^{-4}$	$8*10^{-6}$	$-4*10^{-7}$	48,97	3,8483	420,91

4.3.2 Edge Dislocation Mobility on (112) Plane

Figure 4.7 shows the time versus stress graph of the edge dislocation on the (112) plane at 100K for pure Fe and Fe with 0.1%, 0.25%, and 0.5% hydrogen concentrations. The applied stress was gradually increased from 0 MPa to the desired stress value within 0.5 ns and thereafter, a constant stress is applied to the system. According to the figure, with the presence of hydrogen and increasing hydrogen concentration, the dislocation motion initiates at higher stress values. Fluctuations in the time versus stress graphs are more pronounced when the stress is near the critical stress value, indicating a transition region. When the stress is just sufficient to induce the dislocation motion, stress fluctuations are more dominant. Conversely, when the stress is more than adequate, the fluctuations are reduced. This occurs because dislocation motion within the cell alters the cell's energy. Stress, being a form of energy applied to the system, undergoes stabilization, leading to stress fluctuations. As the stress value increases, this stabilization process occurs more quickly, resulting in a smoother process. Time versus stress graphs at other temperatures are provided in the Supplementary Figures 28 through 31.

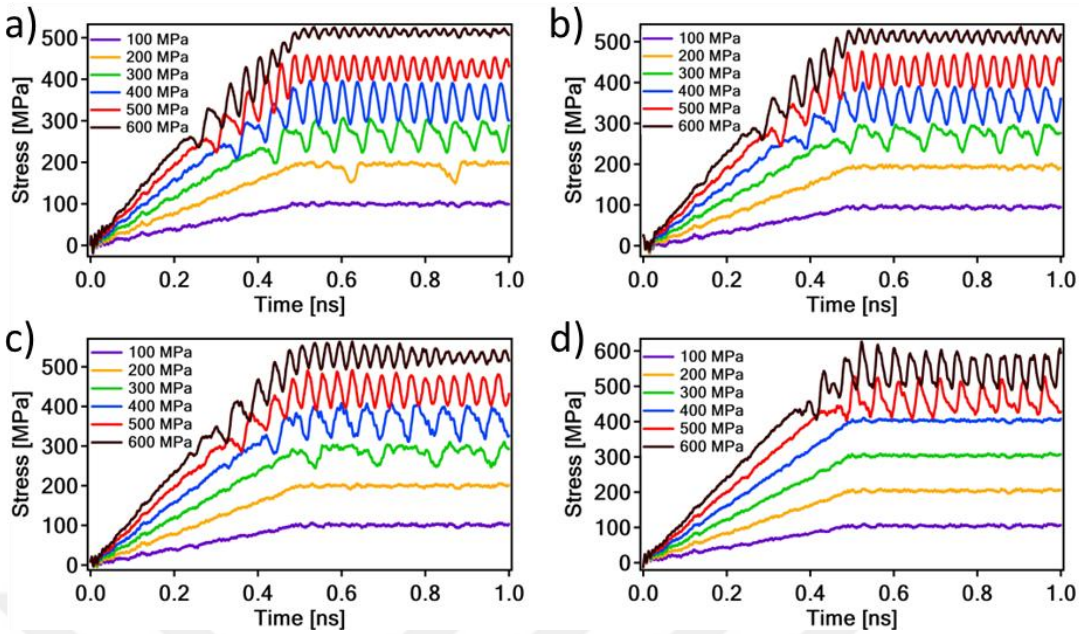

Figure 4.7 Stress versus time graphs at 100K for the {112} plane. Here, a) shows the pure iron case 0% H/Fe, b) shows 0.1% H/Fe concentration, c) shows 0.25% H/Fe concentration, and d) shows 0.5% H/Fe concentration.

Figure 4.8 presents the dislocation core displacement versus time graph for pure hydrogen-free simulations at temperatures of 100K, 200K, 300K, 400K, and 500K, while the results for hydrogen-containing lattices are given in Supplementary Figures 32 through 34. The lowest stress values, where the dislocation motion starts, cause core displacement fluctuations due to the stress being close to the critical stress value, similar to the observation in Figure 4.7. In addition, increasing the stress resulted in a greater core displacement at all temperatures. After applying linear fits to the dislocation time versus displacement graphs after 0.5 ns, the velocities of these dislocations have been calculated, as depicted in Figure 4.9.

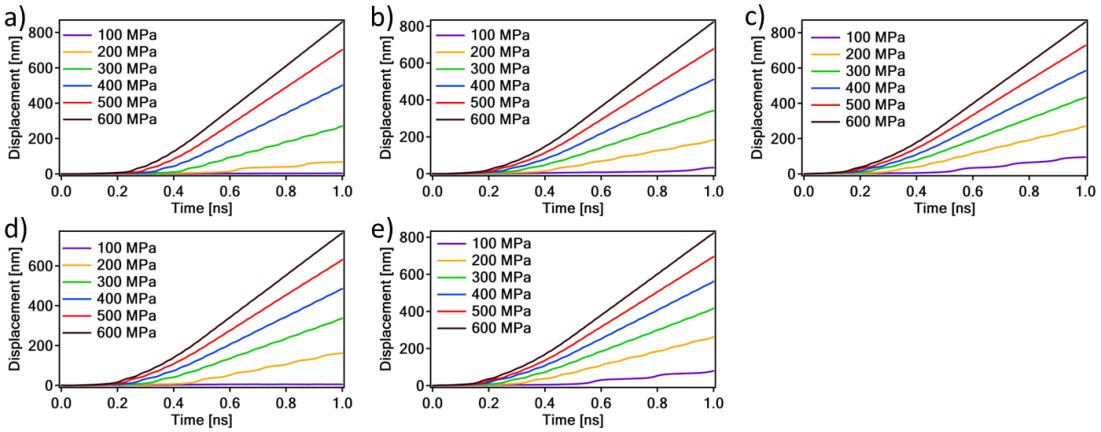

Figure 4.8 Dislocation displacement vs time graph of pure iron cases. Here, from a to e, graphs belong to 100K, 200K, 300K, 400K and 500K temperature values.

Figure 4.9a-e show the effect of hydrogen on the dislocation velocity in hydrogen-free and hydrogen-containing lattices at different temperatures and Figure 4.9f shows the comparison of {110} and {112} glide planes at 100 K. At all temperatures, the dislocation velocity increases monotonically with the applied stress. The simulation cells of pure iron exhibit higher dislocation velocities compared to those with hydrogen. In addition, increasing the hydrogen content resulted in lower dislocation velocities at all temperatures (Figure 4.9a-e) since hydrogen pins the dislocation and greater amount of energy is required to overcome this barrier. Our results correspond well with those in the literature [133]. Table 4.3 summarizes whether the dislocation is glissile or not at a given temperature and applied stress. Similar to the dislocation simulations on {110}, hydrogen also pinned the dislocation along the {112} plane due to the speed of dislocation. Changing the dislocation glide plane from {110} to {112} decreases the velocity of dislocation at the same applied stress (Figure 4.9f) and this result agrees well with those in the literature. It was reported that, dislocations on {110} glide planes have very low kink energies and exhibit faster kink pair formation and, furthermore, move according to the phonon drag mechanism [133]. Conversely, dislocations on {112} glide planes tend to advance through the nucleation of kink pairs in greater numbers and maintain kink formation for longer durations [133]. In addition, the ½ <111>{112} dislocation has an asymmetrical core structure, which is harder to move compared to the planar core structure. Therefore, the Peierls stress for the ½ <111>{112} dislocation is greater than the one for the ½ <111>{110} dislocation [133]. In addition, at low stress values, the motion of the ½ <111>{112} dislocation is governed by thermally activated mechanisms, while at higher stress values, viscous damping dynamics predominate, similar to the behavior observed in their ½ <111>{110} counterparts. Consequently, the glide of the dislocation {112} plane occurs significantly more slowly at low stress and temperature compared to the {110} plane. But this difference decreases at higher stress and temperature values (Figure 4.9f) and this result agrees well the previous studies [133,146,147]. This result, has also been attributed to the observation that the velocity response exhibits a directional asymmetry on the {112} plane, aligning with the twinning-anti twinning (TD-AT) asymmetry [146,147]. Simulations involving hydrogen have shown that, the hydrogen environment promotes kink pair nucleation, which is more pronounced on the {112} glide plane [133].

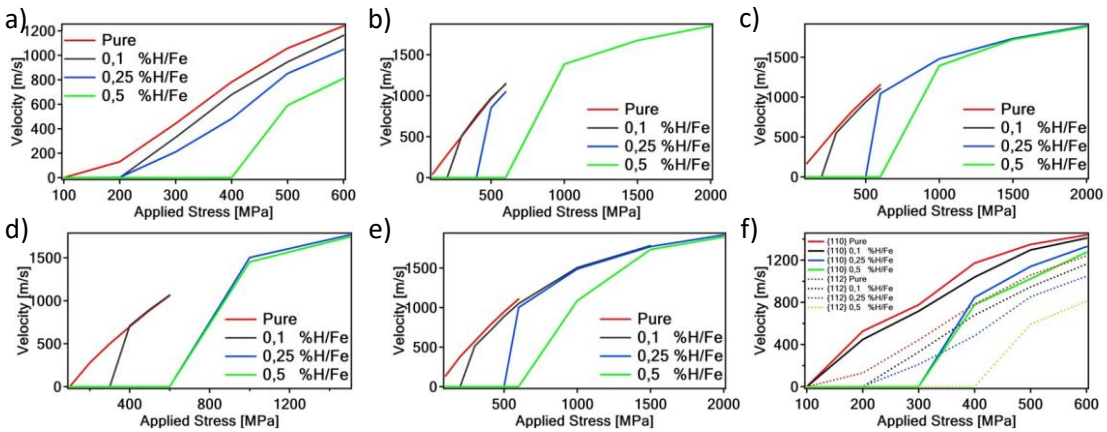

Figure 4.9 Stress vs dislocation velocity graphs of a) Hydrogen-induced lattice at 100K, b) Hydrogen-induced lattice at 200K, c) Hydrogen-induced lattice at 300K, d) Hydrogen-induced lattice at 400K, e) Hydrogen-induced lattice at 500K, f) ½ <111>{110} and ½ <111>{112} dislocations

Table 4.3 Effect of hydrogen on the dislocation mobility. g: glissile dislocation, s: sessile dislocation, N/A: Not available.

	100 MPa					**200 MPa**				
H/Fe (%)	**100 K**	**200 K**	**300 K**	**400 K**	**500 K**	**100 K**	**200 K**	**300 K**	**400 K**	**500 K**
0	s	g	g	s	g	g	g	g	g	g
0.1	s	s	s	s	s	s	s	s	s	s
0.25	s	s	s	s	s	s	s	s	s	s
0.5	s	s	s	s	s	s	s	s	s	s
	300 MPa					**400 MPa**				
H/Fe (%)	**100 K**	**200 K**	**300 K**	**400 K**	**500 K**	**100 K**	**200 K**	**300 K**	**400 K**	**500 K**
0	g	g	g	g	g	g	g	g	g	g
0.1	g	g	g	s	g	g	g	g	g	g
0.25	g	s	s	s	s	g	s	s	s	s
0.5	s	s	s	s	s	s	s	s	s	s

An analytical relation for the dislocation mobility on the {112} glide plane for pure α-iron simulation can again be cast in the formula $B(T) = B_0 + B_1 T$, similar to the formulation for the {110} glide plane. Here, the B_0 and B_1 values were determined as $9*10^{-5}$ [Pa*s] and 10^{-7} [Pa*s/K], respectively. These values were derived for hydrogen free case (c=0) in order to compare them with literature. In the literature, the mobility law for the {112} edge dislocation has been written as $v_{(112)}=5.5\tau_a-1307.0$ before [146] we note this expression would also fit well with our results.

In the current study, the drag coefficient (B) depends on both temperature and the hydrogen content. To extract a mobility law from the data, the same methodology presented above for the {110} case, was followed to derive the various parameters in the equations. The change in the drag coefficient B(T,c) according to the given temperature and hydrogen concentration is presented in Figure 4.10a. According to the figure, Eq. 4.2 can be utilized to describe the change in the drag coefficient for the {112} glide plane as well. Figure 4.10b and 10c show hydrogen concentration vs B_0 and hydrogen concentration vs B_1 graphs, respectively. The change in B_0 is not monotonic with respect to the hydrogen concentration (Figure 4.10b); therefore, as done for the {110} plane, $B_0(T)$ was considered constant and the mean value of $B_0(T)$ was taken as a constant B_0, to use in the equations. The change in B_1 with respect to the hydrogen concentration, shown in Figure 4.10c, shows a monotonic increase, and is roughly approximated by straight line, such that this dependence on hydrogen concentration can be expressed as:

$$B_1(c) = B_2 * c + B_3 \tag{4.8}$$

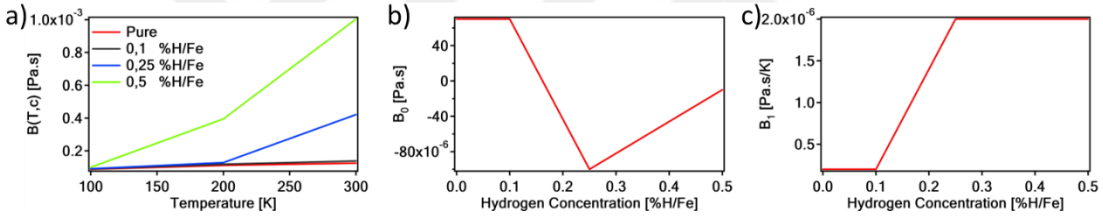

Figure 4.10 Graph illustrating the change in drag coefficient with temperature for pure iron and edge dislocation on the (112) glide plane.

Figure 4.11a shows the hydrogen concentration versus critical stress graphs for the edge dislocation on the {112} glide plane. The change in critical stress according to the given hydrogen concentration and temperature can also be formulated using Eq. 4.6. Here, the change in A_0 with respect to temperature is not monotonic (Figure 4.11b), and thus again the mean value of A_0 is used. On the other hand, the change in A_1 with respect to temperature is roughly linear (Figure 4.11c), as observed in the results for the {110} glide plane. Therefore, we perform a linear fit analogous to the one used for Eq. 4.7. The parameters for the description of the drag coefficients of ½ <111>{110} dislocation are given in Table 4.4.

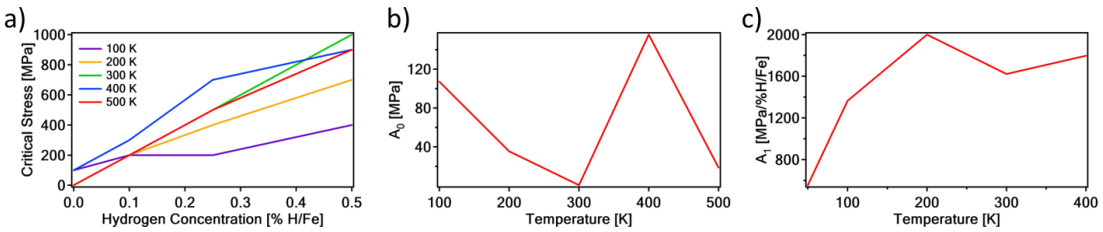

Figure 4.11 a) presents the hydrogen concentration versus critical stress graphs for the (112) glide plane. b) shows the change in A_0 according to the given temperature values. c) shows the change in A_1 according to the given temperature values.

Table 4.4 A and B values for the edge dislocation mobility on (112) glide plane.

B_0 [Pa*s]	B_2 [Pa*s/(K*%H/Fe)]	B_3 [Pa*s/K]	A_0 [MPa]	A_2 [MPa/(K*%H/Fe)]	A_3 [MPa]
$7,5*10^{-6}$	$4*10^{-6}$	$2*10^{-7}$	63,4257	2,7387	645,34

According to Table 4.1 and Table 4.3, on both the {110} and {112} glide planes, an analogous relationship between applied stress and dislocation mobility has been observed. This means that the dislocation mobility increases with stress. On the other hand, the dislocation mobility decreases with increasing temperature, which has been attributed to the phonon drag mechanism previously [146]. The A value, which pertains to the critical stress value calculations, is positive. This indicates that the critical stress value at which the dislocation starts to move increases with higher temperature and hydrogen concentration values.

4.4 Conclusion

In this study, the dependence of mobility for ½<111>{110} and ½<111>{112} edge dislocations on the presence of hydrogen was investigated and new phenomenological formulas for the analytical description of this relationship were proposed. To achieve this, molecular dynamics simulations were performed using the LAMMPS code to observe the dislocation dynamics in detail, with and without hydrogen in BCC iron, at different temperature and stress values. The following conclusions can be drawn from the study:

- Hydrogen decreases the mobility of both ½<111>{110} and ½<111>{112} edge dislocations via pinning effect.
- Kink pair formation and propagation is very fast for the edge dislocation along {110} plane so it moves with phonon drag mechanism, whereas, both thermally

activated mechanisms and viscous damping dynamics constitute the motion of the ½ <111>{112} dislocation.

- Peierls stress for the ½ <111>{112} dislocation is greater than that for the ½ <111>{110} dislocation.
- Hydrogen-induced mobility laws were proposed for both ½ <111>{110} and ½ <111>{112} edge dislocations. In particular, the closed form of the hydrogen-induced mobility laws of ½<111>{110} and ½<111>{112} edge dislocations are given is Eq. 4.9 and Eq. 4.10, respectively. One can easily calculate the velocity of dislocations at any given applied stress, temperature, and hydrogen concentration. As these mobility laws are derived using four different hydrogen concentrations (0% H/Fe, 0.1% H/Fe, 0.25% H/Fe, and 0.5% H/Fe) and five different temperatures (50 K, 100 K, 200 K, 300 K, and 400 K), more accurate results are expected via interpolation. However, different mechanics and dynamics might be observed when extrapolating these values. Nonetheless, these mobility laws will still provide a very useful basis for discussion during extrapolation.

$$v_{½<111>\{110\}} = \frac{(\tau_{app} - (48{,}97 + (3{,}8483 * T + 420{,}91) * c)) * b}{(-6 * 10^{-4} * c + 1 * 10^{-4}) + (8 * 10^{-6} * c + -4 * 10^{-7}) * T} \quad (4.9)$$

$$v_{½<111>\{112\}} = \frac{\left(\tau_{app} - (63{,}4257 + (2{,}7387 * T + 645{,}34) * c)\right) * b}{7{,}5 * 10^{-6} + (4 * 10^{-6} * c + 2 * 10^{-7}) * T} \quad (4.10)$$

Acknowledgements

This study was supported by Scientific and Technological Research Council of Turkey (TUBITAK) under the Grant Number 122M754. The authors thank to TUBITAK for their supports.

Chapter 5

Conclusions And Future Prospects

5.1 Conclusions

In this study, the hydrogen embrittlement phenomenon has been investigated at different strain rates, loading conditions, and materials, and the study includes experimental and computational contents. The first study [3] included strain rate sensitivity investigation of Al 7075 alloy under hydrogen effect. The strain rate range was chosen to investigate the material quasi-static and medium strain rates. According to the results, it was observed that, at higher strain rates, the HE is more dominant compared, this was contrary to what was underlined in the literature. This was attributed to the fact that, dislocation density can be greater after a level of strain rate. At medium strain rate, HEDE was more dominant compared to the quasi-static strain rate. At the second study [57], the ballistic behavior of Al 5083 was investigated under ballistic loading. According to the results, HE is present at ultra-high strain rates like ballistic loading. Also, the study included FEM part to investigate the HE, also in the FEM part, Johnson-Cook parameters were also studied, and the new parameters was able to be used for accurate prediction of ballistic behavior of hydrogen charged Al 5083 H131. In the third study [120], edge dislocation mobility in BCC iron material has been investigated with and without hydrogen using molecular dynamic simulations. A phenomenological model was constructed using the results. This new outcome which implements the hydrogen effect on edge dislocation mobility can be used in greater scale of simulations.

5.2 Societal Impact and Contribution to Global Sustainability

This study advances our understanding of hydrogen embrittlement (HE), a key barrier to the adoption of hydrogen as a clean, sustainable energy source. By investigating HE effects across various strain rates, materials, and loading conditions, the research provides critical insights for industries relying on hydrogen or lightweight metals. By improving our understanding of HE across various materials and strain conditions, the research directly contributes to making hydrogen safer and more viable for widespread applications, such as in transportation, energy storage, and aerospace. The findings, particularly regarding the behavior of aluminum alloys (Al 7075 and Al 5083) and BCC iron, have wide-ranging applications in sectors like aerospace, defense, and automotive manufacturing—industries poised to benefit from safer, more resilient materials under hydrogen-rich environments.

This study enhances the accuracy of HE predictions, helping engineers for design. For instance, the novel Johnson-Cook parameters developed here improve the predictive capabilities of ballistic simulations for hydrogen-charged materials, supporting the design of safer and more durable components in critical infrastructure and defense. Further, the phenomenological model developed for edge dislocation mobility in BCC iron can be used for future large-scale simulations of hydrogen effects in structural materials. This model not only contributes to the development of safer materials but also aids the material economy's shift toward sustainable, high-performance alloys that mitigate HE risks.

Utilizing hydrogen in a safer manner, can contribute to a reduced carbon footprint and the sustainable evolution of critical engineering applications. In line with global sustainability goals, this research promotes resource efficiency and material durability, helping reduce material waste and enhance the life of engineering components in hydrogen-rich applications. By addressing hydrogen embrittlement and expanding the feasibility of hydrogen as a clean energy source, the study not only contributes to a low-carbon future but also supports innovations in sustainable engineering, resource management, and reliable infrastructure.

5.3 Future Prospects

The insights gained from this study on HE open several avenues for further research and development. In the future works, the experimental and computational methods can be further extended in wider range of materials. This can give more insight into this phenomenon. Moreover, the phenomenological model can be further extended including wider range of materials, temperature, stress levels and hydrogen concentrations. The Johnson-Cook parameters can be further investigated of better understanding the HE at different conditions. All further investigations of HE can lead the industries to better anticipate material behavior under HE. This better understanding can lead to lower carbon emissions, production costs, increased safety and durability. Moreover, safer hydrogen energy can be possible with better understanding of HE.

BIBLIOGRAPHY

[1]D. Hauglustaine, F. Paulot, W. Collins, R. Derwent, M. Sand, and O. Boucher, “Climate benefit of a future hydrogen economy,” *Commun Earth Environ*, vol. 3, no. 1, Dec. 2022, doi: 10.1038/s43247-022-00626-z.

[2]A. Pradhan, M. Vishwakarma, and S. K. Dwivedi, “A review: The impact of hydrogen embrittlement on the fatigue strength of high strength steel,” *Mater Today Proc*, vol. 26, pp. 3015–3019, 2020, doi: 10.1016/j.matpr.2020.02.627.

[3]M. F. Baltacioglu, B. Cetin, and B. Bal, “The Effect of Strain Rate on the Hydrogen Embrittlement Susceptibility of Aluminum 7075,” *J Eng Mater Technol*, vol. 145, no. 2, Nov. 2022, doi: 10.1115/1.4056158.

[4]S. K. Dwivedi and M. Vishwakarma, “Hydrogen embrittlement in different materials: A review,” *Int J Hydrogen Energy*, vol. 43, no. 46, pp. 21603–21616, 2018, doi: 10.1016/j.ijhydene.2018.09.201.

[5]S. K. Dwivedi and M. Vishwakarma, “Effect of hydrogen in advanced high strength steel materials,” Oct. 22, 2019, *Elsevier Ltd*. doi: 10.1016/j.ijhydene.2019.08.149.

[6]P. Xu, C. Li, W. Li, M. Zhu, W. Li, and K. Zhang, “Effect of microstructure on hydrogen embrittlement susceptibility in quenching-partitioning-tempering steel,” *Materials Science and Engineering: A*, vol. 831, no. September 2021, p. 142046, 2021, doi: 10.1016/j.msea.2021.142046.

[7]F. Özen, A. İlhan, H. T. Sezan, E. İlhan, and S. Aslanlar, “Effect of the galvanization process on the fatigue life of high strength steel compression springs,” *Materials Testing*, vol. 63, no. 3, pp. 226–230, 2021, doi: doi:10.1515/mt-2020-0032.

[8]B. Bal, I. Sahin, A. Uzun, and D. Canadinc, “A New Venue Toward Predicting the Role of Hydrogen Embrittlement on Metallic Materials,” *Metall Mater Trans A Phys Metall Mater Sci*, vol. 47, no. 11, pp. 5409–5422, Nov. 2016, doi: 10.1007/s11661-016-3708-z.

[9]B. Bal, B. Okdem, F. C. Bayram, and M. Aydin, “A detailed investigation of the effect of hydrogen on the mechanical response and microstructure of Al 7075 alloy under medium strain rate impact loading,” *Int J Hydrogen Energy*, vol. 45, no. 46, pp. 25509–25522, 2020, doi: 10.1016/j.ijhydene.2020.06.241.

[10] E. P. Georgiou, J. P. Celis, and C. N. Panagopoulos, “The effect of cold rolling on the hydrogen susceptibility of 5083 aluminum alloy,” *Metals (Basel)*, vol. 7, no. 11, 2017, doi: 10.3390/met7110451.

[11] O. Gosheva, G. Andersohn, and M. Oechsner, “Comparative study of the testing approaches for the susceptibility of high-strength fasteners to environmental hydrogen embrittlement (EHE),” vol. 60, no. 3, pp. 251–256, 2018, doi: doi:10.3139/120.111147.

[12] D. Ashkenazi, “How aluminum changed the world: A metallurgical revolution through technological and cultural perspectives,” *Technol Forecast Soc Change*, vol. 143, pp. 101–113, Jun. 2019, doi: 10.1016/j.techfore.2019.03.011.

[13] N. M. Han, X. M. Zhang, S. D. Liu, D. G. He, and R. Zhang, “Effect of solution treatment on the strength and fracture toughness of aluminum alloy 7050,” *J Alloys Compd*, vol. 509, no. 10, pp. 4138–4145, Mar. 2011, doi: 10.1016/j.jallcom.2011.01.005.

[14] B. BAL, “DETERMINATION OF MATERIAL RESPONSE AND OPTIMIZATION OF JOHNSON-COOK DAMAGE PARAMETERS OF ALUMINIUM 7075 ALLOY,” *Selcuk University Journal of Engineering ,Science and Technology*, vol. 6, no. 2, pp. 343–354, Jun. 2018, doi: 10.15317/scitech.2018.137.

[15] Q. Sun, M. Yang, Y. Jiang, L. Lei, and Y. Zhang, “Achieving excellent corrosion resistance properties of 7075 Al alloy via ultrasonic surface rolling treatment,” *J Alloys Compd*, vol. 911, p. 165009, Aug. 2022, doi: 10.1016/j.jallcom.2022.165009.

[16] P. V. Kumar, G. M. Reddy, and K. S. Rao, “Microstructure, mechanical and corrosion behavior of high strength AA7075 aluminium alloy friction stir welds – Effect of post weld heat treatment,” *Defence Technology*, vol. 11, no. 4, pp. 362–369, Dec. 2015, doi: 10.1016/j.dt.2015.04.003.

[17] N. Takano, “Hydrogen diffusion and embrittlement in 7075 aluminum alloy,” *Materials Science and Engineering A*, vol. 483–484, no. 1-2 C, pp. 336–339, Jun. 2008, doi: 10.1016/j.msea.2006.08.144.

[18] A. Baradeswaran and A. E. Perumal, “Wear and mechanical characteristics of Al 7075/graphite composites,” *Compos B Eng*, vol. 56, pp. 472–476, 2014, doi: 10.1016/j.compositesb.2013.08.073.

[19] M. Tsurudome, H. Yamada, N. Ogasawara, and K. Horikawa, “Effect of Pre-Fatigue Deformation under Humid Environment on Impact Tensile Properties in 7075 Aluminum Alloys,” *Applied Mechanics and Materials*, vol. 566, pp. 128–133, Jun. 2014, doi: 10.4028/www.scientific.net/AMM.566.128.

[20] Y. Ogawa, D. Kim, H. Matsunaga, and S. Matsuoka, “EVALUATION OF THE COMPATIBILITY OF HIGH-STRENGTH ALUMINUM ALLOY 7075-T6 TO HIGH-PRESSURE GASEOUS HYDROGEN ENVIRONMENTS,” Prague, Czech Republic, Jul. 2018. [Online]. Available: http://proceedings.asmedigitalcollection.asme.org

[21] A. Rajabipour and R. E. Melchers, “Service life of corrosion pitted pipes subject to fatigue loading and hydrogen embrittlement,” *Int J Hydrogen Energy*, vol. 43, no. 17, pp. 8440–8450, 2018, doi: 10.1016/j.ijhydene.2018.03.063.

[22] M. B. Djukic, G. M. Bakic, V. Sijacki Zeravcic, A. Sedmak, and B. Rajicic, “The synergistic action and interplay of hydrogen embrittlement mechanisms in steels and iron: Localized plasticity and decohesion,” Jul. 01, 2019, *Elsevier Ltd*. doi: 10.1016/j.engfracmech.2019.106528.

[23] M. López Freixes *et al.*, “Revisiting stress-corrosion cracking and hydrogen embrittlement in 7xxx-Al alloys at the near-atomic-scale,” *Nat Commun*, vol. 13, no. 1, Dec. 2022, doi: 10.1038/s41467-022-31964-3.

[24] M. B. Djukic, V. Sijacki Zeravcic, G. M. Bakic, A. Sedmak, and B. Rajicic, “Hydrogen damage of steels: A case study and hydrogen embrittlement model,” *Eng Fail Anal*, vol. 58, pp. 485–498, Dec. 2015, doi: 10.1016/j.engfailanal.2015.05.017.

[25] M. Koyama, C. C. Tasan, E. Akiyama, K. Tsuzaki, and D. Raabe, “Hydrogen-assisted decohesion and localized plasticity in dual-phase steel,” *Acta Mater*, vol. 70, pp. 174–187, May 2014, doi: 10.1016/j.actamat.2014.01.048.

[26] B. N. Popov, J. W. Lee, and M. B. Djukic, “Hydrogen permeation and hydrogen-induced cracking,” in *Handbook of Environmental Degradation Of Materials: Third Edition*, Elsevier Inc., 2018, pp. 133–162. doi: 10.1016/B978-0-323-52472-8.00007-1.

[27] B. Bal, B. Çetin, F. C. Bayram, and E. Billur, “Effect of hydrogen on fracture locus of Fe–16Mn–0.6C–2.15Al TWIP steel,” *Int J Hydrogen Energy*, vol. 45, no. 58, pp. 34227–34240, Nov. 2020, doi: 10.1016/j.ijhydene.2020.09.083.

[28] M. Wasim and M. B. Djukic, “Hydrogen embrittlement of low carbon structural steel at macro-, micro- and nano-levels,” *Int J Hydrogen Energy*, vol. 45, no. 3, pp. 2145–2156, Jan. 2020, doi: 10.1016/j.ijhydene.2019.11.070.

[29] I. B. Tuğluca *et al.*, “Lowering Strain Rate Simultaneously Enhances Carbon- and Hydrogen-Induced Mechanical Degradation in an Fe-33Mn-1.1C Steel,” *Metall Mater Trans A Phys Metall Mater Sci*, vol. 50, no. 3, pp. 1137–1141, Mar. 2019, doi: 10.1007/s11661-018-5080-7.

[30] M. Safyari, T. Hojo, and M. Moshtaghi, “Effect of environmental relative humidity on hydrogen-induced mechanical degradation in an Al–Zn–Mg–Cu alloy,” *Vacuum*, vol. 192, Oct. 2021, doi: 10.1016/j.vacuum.2021.110489.

[31] J. T. Burns, J. J. Jones, A. D. Thompson, and J. S. (Warner) Locke, “Fatigue crack propagation of aerospace aluminum alloy 7075-T651 in high altitude environments,” *Int J Fatigue*, vol. 106, pp. 196–207, Jan. 2018, doi: 10.1016/j.ijfatigue.2017.09.017.

[32] K. Kariya, N. Kawagoishi, H. Maeda, Q. Chen, M. Goto, and Y. Nu, “Fatigue fracture mechanism of extruded Al alloy 7075-T6 in high humidity,” in *Key Engineering Materials*, Trans Tech Publications Ltd, 2012, pp. 45–48. doi: 10.4028/www.scientific.net/KEM.488-489.45.

[33] R. Yamada, G. Itoh, A. Kurumada, and M. Nakai, “Further study on the effect of environment on fatigue crack growth behavior of 2000 and 7000 series aluminum alloys,” in *Materials Science Forum*, Trans Tech Publications Ltd, 2017, pp. 2153–2157. doi: 10.4028/www.scientific.net/MSF.879.2153.

[34] H. Yamada, M. Tsurudome, N. Miura, K. Horikawa, and N. Ogasawara, “Ductility loss of 7075 aluminum alloys affected by interaction of hydrogen, fatigue deformation, and strain rate,” *Materials Science and Engineering A*, vol. 642, pp. 194–203, Aug. 2015, doi: 10.1016/j.msea.2015.06.084.

[35] W. J. Qi, R. G. Song, Y. Zhang, C. Wang, X. Qi, and H. Li, “Study on mechanical properties and hydrogen embrittlement susceptibility of 7075 aluminium alloy,” *Corrosion Engineering Science and Technology*, vol. 50, no. 6, pp. 480–486, Sep. 2015, doi: 10.1179/1743278215Y.0000000004.

[36] S. Deya, I. Chattoraja, and S. Sivaprasada, “Effect of Hydrogen on Mechanical Degradation and Fatigue in 7075 Aluminium Alloy with In-situ Hydrogenation,” in *Procedia Engineering*, Elsevier Ltd, 2015, pp. 461–469. doi: 10.1016/j.proeng.2015.08.093.

[37] P. Bałon, E. Rejman, R. Smusz, J. Szostak, and B. Kiełbasa, “Implementation of high speed machining in thin-walled aircraft integral elements,” *Open Engineering*, vol. 8, no. 1, pp. 162–169, Jun. 2018, doi: 10.1515/eng-2018-0021.

[38] S. Dey and I. Chattoraj, “Interaction of strain rate and hydrogen input on the embrittlement of 7075 T6 Aluminum alloy,” *Materials Science and Engineering A*, vol. 661, pp. 168–178, Apr. 2016, doi: 10.1016/j.msea.2016.03.010.

[39] G. Rotella, O. W. Dillon, D. Umbrello, L. Settineri, and I. S. Jawahir, “Finite element modeling of microstructural changes in turning of AA7075-T651 Alloy,” *J Manuf Process*, vol. 15, no. 1, pp. 87–95, 2013, doi: 10.1016/j.jmapro.2012.09.005.

[40] I. B. Tuğluca, M. Koyama, B. Bal, D. Canadinc, E. Akiyama, and K. Tsuzaki, “High-concentration carbon assists plasticity-driven hydrogen embrittlement in a Fe-high Mn steel with a relatively high stacking fault energy,” *Materials Science and Engineering A*, vol. 717, pp. 78–84, Feb. 2018, doi: 10.1016/j.msea.2018.01.087.

[41] A. Rusinek and J. A. Rodríguez-Martínez, “Thermo-viscoplastic constitutive relation for aluminium alloys, modeling of negative strain rate sensitivity and viscous drag effects,” *Mater Des*, vol. 30, no. 10, pp. 4377–4390, Dec. 2009, doi: 10.1016/j.matdes.2009.04.011.

[42] Y. Choi, J. Ha, M. G. Lee, and Y. P. Korkolis, “Observation of Portevin-le Chatelier effect in aluminum alloy 7075-w under a heterogeneous stress field,” *Scr Mater*, vol. 205, Dec. 2021, doi: 10.1016/j.scriptamat.2021.114178.

[43] P. Zhou, Y. Song, L. Hua, J. Lu, J. Zhang, and F. Wang, “Mechanical behavior and deformation mechanism of 7075 aluminum alloy under solution induced dynamic strain aging,” *Materials Science and Engineering A*, vol. 759, pp. 498–505, Jun. 2019, doi: 10.1016/j.msea.2019.05.071.

[44] B. Bal, M. Koyama, G. Gerstein, H. J. Maier, and K. Tsuzaki, “Effect of strain rate on hydrogen embrittlement susceptibility of twinning-induced plasticity steel pre-charged with high-pressure hydrogen gas,” *Int J Hydrogen Energy*, vol. 41, no. 34, pp. 15362–15372, Sep. 2016, doi: 10.1016/j.ijhydene.2016.06.259.

[45] T. Michler and J. Naumann, “Hydrogen environment embrittlement of austenitic stainless steels at low temperatures,” *Int J Hydrogen Energy*, vol. 33, no. 8, pp. 2111–2122, Apr. 2008, doi: 10.1016/j.ijhydene.2008.02.021.

[46] H. K. Birnbaum, “HYDROGEN EFFECTS ON DEFORMATION-RELATION BETWEEN DISLOCATION BEHAVIOR AND THE MACROSCOPIC STRESS-STRAIN BEHAVIOR,” 1994.

[47] H. Fan, Q. Wang, J. A. El-Awady, D. Raabe, and M. Zaiser, “Strain rate dependency of dislocation plasticity,” *Nat Commun*, vol. 12, no. 1, Dec. 2021, doi: 10.1038/s41467-021-21939-1.

[48] M. Barsanti, M. Beghini, F. Frasconi, R. Ishak, B. D. Monelli, and R. Valentini, “Experimental study of hydrogen embrittlement in Maraging steels,” in *Procedia Structural Integrity*, Elsevier B.V., 2018, pp. 501–508. doi: 10.1016/j.prostr.2017.12.049.

[49] Dawari A, Kashyap B, and Singh R, “Investigation of Adiabatic Heat Rise and its Effect on Flow Stresses and Microstructural Changes During High Strain Rate Deformation of Ti6Al4V Alloy,” in *Sustainable Industrial Processing Summit SIPS 2017 Volume 9. Iron and Steel, Metals and Alloys*, Oct. 2017, pp. 178–189.

[50] N. I. Vazquez-Fernandez *et al.*, “Adiabatic Heating of Austenitic Stainless Steels at Different Strain Rates,” *Journal of Dynamic Behavior of Materials*, vol. 5, no. 3, pp. 221–229, Sep. 2019, doi: 10.1007/s40870-019-00204-z.

[51] C. Sorini, ; Aditi Chattopadhyay, and R. K. Goldberg, “Effects of Adiabatic Heating on the High Strain Rate Deformation Response of Triaxially Braided Polymer Matrix Composites,” in *Earth and Space*, Cleveland, United States, Sep. 2018.

[52] S. S. Singh, C. Schwartzstein, J. J. Williams, X. Xiao, F. De Carlo, and N. Chawla, "3D microstructural characterization and mechanical properties of constituent particles in Al 7075 alloys using X-ray synchrotron tomography and nanoindentation," *J Alloys Compd*, vol. 602, pp. 163–174, Jul. 2014, doi: 10.1016/j.jallcom.2014.03.010.

[53] F. Dong *et al.*, "Effect of vanadium and rare earth microalloying on the hydrogen embrittlement susceptibility of a Fe-18Mn-0 . 6C TWIP steel studied using the linearly increasing stress test," *Corros Sci*, vol. 185, no. November 2020, p. 109440, 2021, doi: 10.1016/j.corsci.2021.109440.

[54] Y. C. Lin, X. H. Zhu, W. Y. Dong, H. Yang, Y. W. Xiao, and N. Kotkunde, "Effects of deformation parameters and stress triaxiality on the fracture behaviors and microstructural evolution of an Al-Zn-Mg-Cu alloy," *J Alloys Compd*, vol. 832, Aug. 2020, doi: 10.1016/j.jallcom.2020.154988.

[55] R. Yoshioka, S. Haruyama, K. Kaminishi, and S. Osaki, "A Comparison in Hydrogen-Environment Embrittlement Response Between T6 and T73 Tempers of 7075 Aluminum Alloy," *Proceedings of the 8th International Conference on Innovation & Management*.

[56] J. R. Scully, G. A. Young, and S. W. Smith, "Hydrogen embrittlement of aluminum and aluminum-based alloys," in *Gaseous Hydrogen Embrittlement of Materials in Energy Technologies: The Problem, its Characterisation and Effects on Particular Alloy Classes*, Elsevier Ltd., 2012, pp. 707–768. doi: 10.1533/9780857093899.3.707.

[57] M. F. Baltacioglu *et al.*, "Hydrogen susceptibility of Al 5083 under ultra-high strain rate ballistic loading," vol. 66, no. 10, pp. 1627–1643, 2024, doi: doi:10.1515/mt-2024-0056.

[58] M. C. Santos, A. R. Machado, W. F. Sales, M. A. S. Barrozo, and E. O. Ezugwu, "Machining of aluminum alloys: a review," Oct. 01, 2016, *Springer London*. doi: 10.1007/s00170-016-8431-9.

[59] E. Buray-Mihälyi, E. Czoboly, and Z. Buray, "Fracture behaviour and mechanical properties of aluminium alloy plates," vol. 17, no. 9, pp. 316–319, 1975, doi: doi:10.1515/mt-1975-170906.

[60] A. V. Jebaraj, K. V. V Aditya, T. S. Kumar, L. Ajaykumar, and C. R. Deepak, "Mechanical and corrosion behaviour of aluminum alloy 5083 and its weldment for marine applications," *Mater Today Proc*, vol. 22, pp. 1470–1478, 2020, doi: https://doi.org/10.1016/j.matpr.2020.01.505.

[61] K. Ozel, C. S. Cetinarslan, and M. Sahin, "Mechanical properties of friction stir welded 5083 aluminum alloys," vol. 59, no. 1, pp. 64–68, 2017, doi: doi:10.3139/120.110965.

[62] S. N. Patankar and T. M. Jen, "Strain Rate Insensitive Plasticity in Aluminum Alloy 5083," *Scr Mater*, vol. 38, no. 8, pp. 1255–1261, 1998, doi: https://doi.org/10.1016/S1359-6462(98)00017-7.

[63] J. Jaume, M. J. F. Marques, M. L. Délia, and R. Basséguy, "Surface modification of 5083 aluminum-magnesium induced by marine microorganisms," Jan. 01, 2022, *Elsevier Ltd*. doi: 10.1016/j.corsci.2021.109934.

[64] R. L. Holtz, P. S. Pao, R. A. Bayles, T. M. Longazel, and R. Goswami, "Corrosion-fatigue behavior of aluminum alloy 5083-H131 sensitized at 448 K (175 C)," in

Metallurgical and Materials Transactions A: Physical Metallurgy and Materials Science, Aug. 2012, pp. 2839–2849. doi: 10.1007/s11661-011-0866-x.

[65] K. Hirayama *et al.*, "Damage micromechanisms of stress corrosion cracking in Al-Mg alloy with high magnesium content," *Corros Sci*, vol. 184, May 2021, doi: 10.1016/j.corsci.2021.109343.

[66] J. H. Ai, M. L. C. Lim, and J. R. Scully, "Effective hydrogen diffusion in aluminum alloy 5083-H131 as a function of orientation and degree of sensitization," *Corrosion*, vol. 69, no. 12, pp. 1225–1239, 2013, doi: 10.5006/0987.

[67] C. N. Panagopoulos and E. P. Georgiou, "The effect of hydrogen charging on the mechanical behaviour of 5083 wrought aluminum alloy," *Corros Sci*, vol. 49, no. 12, pp. 4443–4451, Dec. 2007, doi: 10.1016/j.corsci.2007.03.047.

[68] E. P. Georgiou, J. P. Celis, and C. N. Panagopoulos, "The effect of cold rolling on the hydrogen susceptibility of 5083 aluminum alloy," *Metals (Basel)*, vol. 7, no. 11, Nov. 2017, doi: 10.3390/met7110451.

[69] S.-J. Kim, M.-S. Han, and S.-K. Jang, "Electrochemical characteristics of Al-Mg alloy in seawater for leisure ship: Stress corrosion cracking and hydrogen embrittlement," *Korean Journal of Chemical Engineering*, vol. 26, no. 1, pp. 250–257, 2009, doi: 10.1007/s11814-009-0042-9.

[70] S. J. Kim, S. K. Kim, and J. C. Park, "The corrosion and mechanical properties of Al alloy 5083-H116 in metal inert gas welding based on slow strain rate test," *Surf Coat Technol*, vol. 205, no. SUPPL. 1, Dec. 2010, doi: 10.1016/j.surfcoat.2010.04.039.

[71] T. Pinger, J. Riedel, A. Diehl, and R. Mayrhofer, "Investigation of the hydrogen embrittlement susceptibility of steel components during thin-film hot-dip galvanizing," *Materialpruefung/Materials Testing*, vol. 64, no. 5, pp. 667–677, May 2022, doi: 10.1515/mt-2022-2002.

[72] O. Gosheva, G. Andersohn, and M. Oechsner, "Comparative study of the testing approaches for the susceptibility of high-strength fasteners to environmental hydrogen embrittlement (EHE)," *Materials Testing*, vol. 60, no. 3, pp. 251–256, 2018, doi: doi:10.3139/120.111147.

[73] S. Hereñú, A. Armas, E. Brandaleze, and G. Mansilla, "Hydrogen Influence on the Mechanical Behaviour of High Strength Steel," *Materials Testing*, vol. 52, no. 9, pp. 610–614, 2010, doi: doi:10.3139/120.110168.

[74] B. Kroeger, H. Hetzner, S. G. Klose, T. Mehner, R. Holbein, and T. Lampke, "Mechanical test procedures for the evaluation of hydrogen-assisted damage in high-strength steel," *Materials Testing*, vol. 61, no. 11, pp. 1061–1071, 2019, doi: doi:10.3139/120.111432.

[75] S. Corsinovi, L. Bacchi, M. Mastroianni, N. Bigollo, and R. Valentini, "Hydrogen embrittlement in high strength fasteners: Comparison between bainitic and tempered martensitic steels," *Eng Fail Anal*, vol. 152, Oct. 2023, doi: 10.1016/j.engfailanal.2023.107474.

[76] L. Deconinck, M. T. Villa Vidaller, E. Bernardo Quejido, E. A. Jägle, T. Depover, and K. Verbeken, "In-situ hydrogen embrittlement evaluation of as-built and heat treated laser powder bed fused Ti-6Al-4V versus conventionally cold rolled Ti-6Al-4V," *Addit Manuf*, vol. 76, p. 103768, Aug. 2023, doi: 10.1016/j.addma.2023.103768.

[77] U. S. Meda, N. Bhat, A. Pandey, K. N. Subramanya, and M. A. Lourdu Antony Raj, "Challenges associated with hydrogen storage systems due to the hydrogen embrittlement of high strength steels," Jun. 01, 2023, *Elsevier Ltd*. doi: 10.1016/j.ijhydene.2023.01.292.

[78] C. Park, N. Kang, and S. Liu, "Effect of grain size on the resistance to hydrogen embrittlement of API 2W Grade 60 steels using in situ slow-strain-rate testing," *Corros Sci*, vol. 128, pp. 33–41, Nov. 2017, doi: 10.1016/j.corsci.2017.08.032.

[79] K. Takasawa, R. Ikeda, N. Ishikawa, and R. Ishigaki, "Effects of grain size and dislocation density on the susceptibility to high-pressure hydrogen environment embrittlement of high-strength low-alloy steels," *Int J Hydrogen Energy*, vol. 37, no. 3, pp. 2669–2675, Feb. 2012, doi: 10.1016/j.ijhydene.2011.10.099.

[80] F. Galliano, E. Andrieu, J. M. Cloué, G. Odemer, and C. Blanc, "Effect of temperature on hydrogen embrittlement susceptibility of alloy 718 in Light Water Reactor environment," *Int J Hydrogen Energy*, vol. 42, no. 33, pp. 21371–21378, Aug. 2017, doi: 10.1016/j.ijhydene.2017.06.211.

[81] B. Bal, M. Koyama, G. Gerstein, H. J. Maier, and K. Tsuzaki, "Effect of strain rate on hydrogen embrittlement susceptibility of twinning-induced plasticity steel pre-charged with high-pressure hydrogen gas," *Int J Hydrogen Energy*, vol. 41, no. 34, pp. 15362–15372, Sep. 2016, doi: 10.1016/j.ijhydene.2016.06.259.

[82] R. Matsumoto, S. T. Oyinbo, M. Vijendran, and S. Taketomi, "Hydrogen Effect on the Mobility of Edge Dislocation in α-Iron: A Long-Timescale Molecular Dynamics Simulation," *ISIJ International*, vol. 62, no. 11, pp. 2402–2409, 2022, doi: 10.2355/isijinternational.ISIJINT-2022-311.

[83] A. P. Newbery, S. R. Nutt, and E. J. Lavernia, "Multi-Scale Al 5083 for Military Vehicles with Improved Performance," *JOM*, vol. 58, no. 4, pp. 56–61, 2006, doi: 10.1007/s11837-006-0216-4.

[84] X. W. Chen, X. L. Huang, and G. J. Liang, "Comparative analysis of perforation models of metallic plates by rigid sharp-nosed projectiles," *Int J Impact Eng*, vol. 38, no. 7, pp. 613–621, Jul. 2011, doi: 10.1016/j.ijimpeng.2010.12.005.

[85] S. M. Aceves, G. D. Berry, J. Martinez-Frias, and F. Espinosa-Loza, "Vehicular storage of hydrogen in insulated pressure vessels," *Int J Hydrogen Energy*, vol. 31, no. 15, pp. 2274–2283, Dec. 2006, doi: 10.1016/j.ijhydene.2006.02.019.

[86] C. P. Fowler, A. C. Orifici, and C. H. Wang, "A review of toroidal composite pressure vessel optimisation and damage tolerant design for high pressure gaseous fuel storage," Dec. 21, 2016, *Elsevier Ltd*. doi: 10.1016/j.ijhydene.2016.10.039.

[87] S. Kural and M. Ayvaz, "The ballistic behavior of type 1 metallic pressurized hydrogen storage tanks against ballistic threats," *Int J Hydrogen Energy*, vol. 43, no. 44, pp. 20284–20292, Nov. 2018, doi: 10.1016/j.ijhydene.2018.06.126.

[88] Q. Zhao, X. Xiao, R. Ge, Y. Zhang, X. Chen, and B. Jia, "Experimental-numerical study on ballistic impact behavior of 316L austenitic stainless steel plates against blunt and ogival projectiles," *Int J Hydrogen Energy*, 2022, doi: 10.1016/j.ijhydene.2022.11.285.

[89] A. Dorogoy, D. Rittel, and A. Brill, "Experimentation and modeling of inclined ballistic impact in thick polycarbonate plates," *Int J Impact Eng*, vol. 38, no. 10, pp. 804–814, Oct. 2011, doi: 10.1016/j.ijimpeng.2011.05.001.

[90] H. W. Meyer and D. S. Kleponis, “Modeling the high strain rate behavior of titanium undergoing ballistic impact and penetration,” *Int J Impact Eng*, vol. 26, pp. 509–521, 2001, doi: https://doi.org/10.1016/S0734-743X(01)00107-5.

[91] R. Bobbili, B. Ramakrishna, and V. Madhu, “Dynamic compressive behavior and fracture modeling of Titanium alloy IMI 834,” *J Alloys Compd*, vol. 714, pp. 225–231, 2017, doi: 10.1016/j.jallcom.2017.04.228.

[92] S. Choudhary, P. K. Singh, S. Khare, K. Kumar, P. Mahajan, and R. K. Verma, “Ballistic impact behaviour of newly developed armour grade steel: An experimental and numerical study,” *Int J Impact Eng*, vol. 140, Jun. 2020, doi: 10.1016/j.ijimpeng.2020.103557.

[93] P. Ranaweera, M. R. Bambach, D. Weerasinghe, and D. Mohotti, “Ballistic impact response of monolithic steel and tri-metallic steel–titanium–aluminium armour to nonrigid NATO FMJ M80 projectiles,” *Thin-Walled Structures*, vol. 182, Jan. 2023, doi: 10.1016/j.tws.2022.110200.

[94] S. E. Alkhatib, S. Xu, G. Lu, A. Karrech, and T. B. Sercombe, “Dynamic constitutive behavior of LPBFed metal alloys,” *Journal of Materials Research and Technology*, vol. 25, pp. 581–592, Jul. 2023, doi: 10.1016/j.jmrt.2023.05.252.

[95] L. Chang, S. Yuan, X. Huang, and Z. Cai, “Determination of Johnson-Cook damage model for 7xxx laminated aluminum alloy and simulation application,” *Mater Today Commun*, vol. 34, Mar. 2023, doi: 10.1016/j.mtcomm.2022.105224.

[96] T. Hong, F. Ding, F. Chen, H. Zhang, Q. Zeng, and J. Wang, “Study on the Fracture Behaviour of 6061 Aluminum Alloy Extruded Tube during Different Stress Conditions,” *Crystals (Basel)*, vol. 13, no. 3, Mar. 2023, doi: 10.3390/cryst13030489.

[97] R. Rai, G. Kumar, S. Dagar, V. Somashekar, C. A. Mboreha, and P. Modi, “Numerical simulation of ballistic impact on aluminium 5083-H116 plate with Johnson cook plasticity model,” in *Materials Today: Proceedings*, Elsevier Ltd, 2021, pp. 10619–10627. doi: 10.1016/j.matpr.2021.01.373.

[98] T. Børvik, M. J. Forrestal, O. S. Hopperstad, T. L. Warren, and M. Langseth, “Perforation of AA5083-H116 aluminium plates with conical-nose steel projectiles - Calculations,” *Int J Impact Eng*, vol. 36, no. 3, pp. 426–437, Mar. 2009, doi: 10.1016/j.ijimpeng.2008.02.004.

[99] G. Po *et al.*, “A phenomenological dislocation mobility law for bcc metals,” *Acta Mater*, vol. 119, pp. 123–135, Oct. 2016, doi: 10.1016/j.actamat.2016.08.016.

[100] G. Yi, K. C. Littrell, J. D. Poplawsky, D. A. Cullen, E. Sundberg, and M. L. Free, “Characterization of the effects of different tempers and aging temperatures on the precipitation behavior of Al-Mg (5.25 at.%)-Mn alloys,” *Mater Des*, vol. 118, pp. 22–35, Mar. 2017, doi: 10.1016/j.matdes.2017.01.021.

[101] MIL-DTL-46027K(MR), “DETAIL SPECIFICATION ARMOR PLATE, ALUMINUM ALLOY, WELDABLE 5083, 5456, & 5059 Available at: http://assist.daps.dla.mil/.” [Online]. Available: http://assist.daps.dla.mil/.http://www.everyspec.com

[102] “MIL-DTL-46593B (MR), American Society for Quality, 6 July 2006. [Online]. Available at: www.asme.org.” [Online]. Available: www.asme.org

[103] M. A.-B. Ebrahim, “3D laser scanners’ techniques overview Available at: https://www.researchgate.net/publication/282753883.,” *Int J Sci Res*, pp. 323–331, 2015.

[104] G. R. Johnson and W. H. Cook, “Fracture characteristics of three metals subjected to various strains, strain rates, temperatures and pressures,” *Eng Fract Mech*, vol. 21, no. 1, pp. 31–48, Jan. 1985, doi: 10.1016/0013-7944(85)90052-9.

[105] J. W. Hancock and A. C. Mackenzie, “On the mechanisms of ductile failure in high-strength steels subjected to multi-axial stress-states,” *J Mech Phys Solids*, vol. 24, no. 2–3, pp. 147–160, Jun. 1976, doi: 10.1016/0022-5096(76)90024-7.

[106] R. Rai, G. Kumar, S. Dagar, V. Somashekar, C. A. Mboreha, and P. Modi, “Numerical simulation of ballistic impact on aluminium 5083-H116 plate with Johnson cook plasticity model,” *Mater Today Proc*, vol. 46, pp. 10619–10627, Jan. 2021, doi: 10.1016/J.MATPR.2021.01.373.

[107] T. J. Jang, J. B. Kim, and H. Shin, “Identification of plastic constitutive Johnson–Cook model parameters by optimization-based inverse method,” *J Comput Des Eng*, vol. 8, no. 4, pp. 1082–1097, Jul. 2021, doi: 10.1093/JCDE/QWAB033.

[108] J. Ning and S. Y. Liang, “Inverse identification of Johnson-Cook material constants based on modified chip formation model and iterative gradient search using temperature and force measurements,” *International Journal of Advanced Manufacturing Technology*, vol. 102, no. 9–12, pp. 2865–2876, Jun. 2019, doi: 10.1007/S00170-019-03286-0/METRICS.

[109] N. Ojal, H. P. Cherukuri, T. L. Schmitz, K. T. Devlugt, and A. W. Jaycox, “A combined experimental and numerical approach that eliminates the non-uniqueness associated with the Johnson-Cook parameters obtained using inverse methods,” *International Journal of Advanced Manufacturing Technology*, vol. 120, no. 3–4, pp. 2373–2384, May 2022, doi: 10.1007/S00170-021-08640-9/TABLES/12.

[110] J. Pujana, P. J. Arrazola, R. M’Saoubi, and H. Chandrasekaran, “Analysis of the inverse identification of constitutive equations applied in orthogonal cutting process,” *Int J Mach Tools Manuf*, vol. 47, no. 14, pp. 2153–2161, Nov. 2007, doi: 10.1016/J.IJMACHTOOLS.2007.04.012.

[111] G. Chen, C. Ren, W. Yu, X. Yang, and L. Zhang, “Application of genetic algorithms for optimizing the Johnson–Cook constitutive model parameters when simulating the titanium alloy Ti-6Al-4V machining process,” *Proc Inst Mech Eng B J Eng Manuf*, vol. 226, no. 8, pp. 1287–1297, Jun. 2012, doi: 10.1177/0954405412447735.

[112] A. V Bochkaryova, Y. V Li, S. A. Barannikova, and L. B. Zuev, “The effect of hydrogen embrittlement on the mechanical properties of aluminum alloy,” *IOP Conf Ser Mater Sci Eng*, vol. 71, no. 1, p. 012057, 2015, doi: 10.1088/1757-899X/71/1/012057.

[113] B. Bal, B. Çetin, F. C. Bayram, and E. Billur, “Effect of hydrogen on fracture locus of Fe–16Mn–0.6C–2.15Al TWIP steel,” *Int J Hydrogen Energy*, vol. 45, no. 58, pp. 34227–34240, Nov. 2020, doi: 10.1016/J.IJHYDENE.2020.09.083.

[114] E. Kosedag, M. Aydin, and R. Ekici, “Effect of stacking sequence and metal volume fraction on the ballistic impact behaviors of ARALL fiber-metal laminates: An experimental study,” *Polym Compos*, vol. 43, no. 3, pp. 1536–1545, Mar. 2022, doi: 10.1002/pc.26474.

[115] E. Kosedag and R. Ekici, “Low-velocity and ballistic impact resistances of particle reinforced metal–matrix composites: An experimental study,” *J Compos Mater*, vol. 56, no. 7, pp. 991–1002, Mar. 2022, doi: 10.1177/00219983211068101.

[116] J. Dean, C. S. Dunleavy, P. M. Brown, and T. W. Clyne, “Energy absorption during projectile perforation of thin steel plates and the kinetic energy of ejected fragments,” *Int J Impact Eng*, vol. 36, no. 10–11, pp. 1250–1258, Oct. 2009, doi: 10.1016/j.ijimpeng.2009.05.002.

[117] B. Dodd, B. Dodd, and F. Coghe, “Damage caused to metals by kinetic and chemical energy projectiles Security and Use of Innovative Technologies Against Terrorism Damage caused to metals by kinetic and chemical energy projectiles”, doi: 10.13140/RG.2.1.1667.0881.

[118] Rioja et al., “METHODS OF AGING ALUMINUM ALLOYS TO ACHIEVE IMPROVED BALLISTICS PERFORMANCE,” PATENT NO: US 8,758,530 B2, Jun. 24, 2014

[119] M. A. Khan *et al.*, “Microstructure characterization of 7055-T6, 6061-T6511 and 7A52-T6 Al alloys subjected to ballistic impact against heavy tungsten alloy projectile,” *Archives of Civil and Mechanical Engineering*, vol. 19, no. 4, pp. 1484–1496, Aug. 2019, doi: 10.1016/j.acme.2019.10.001.

[120] M. F. Baltacioglu, M. F. Kapci, J. C. Schön, J. Marian, and B. Bal, “A phenomenological hydrogen induced edge dislocation mobility law for bcc Fe obtained by molecular dynamics,” *Int J Hydrogen Energy*, vol. 87, pp. 917–927, 2024, doi: https://doi.org/10.1016/j.ijhydene.2024.08.509.

[121] S. Correa Marques, D. Lima Molter, L. dos S. Almeida, and D. Silva dos Santos, “The influence of the experimental methodology on evaluating the hydrogen embrittlement susceptibility of AISI 4340 steel manufactured by different routes,” *Eng Fail Anal*, vol. 162, Aug. 2024, doi: 10.1016/j.engfailanal.2024.108361.

[122] P. C. Okonkwo *et al.*, “A focused review of the hydrogen storage tank embrittlement mechanism process,” Apr. 26, 2023, *Elsevier Ltd*. doi: 10.1016/j.ijhydene.2022.12.252.

[123] G. Jia *et al.*, “Hydrogen embrittlement in hydrogen-blended natural gas transportation systems: A review,” Sep. 30, 2023, *Elsevier Ltd*. doi: 10.1016/j.ijhydene.2023.04.266.

[124] G. Lu *et al.*, “Hydrogen embrittlement prompt fracture in Ni-based single crystal superalloy,” *Journal of Materials Research and Technology*, vol. 25, pp. 2140–2151, Jul. 2023, doi: 10.1016/j.jmrt.2023.06.088.

[125] C. Huang and X. Gao, “Phase field modeling of hydrogen embrittlement,” *Int J Hydrogen Energy*, vol. 45, no. 38, pp. 20053–20068, Jul. 2020, doi: 10.1016/j.ijhydene.2020.05.015.

[126] M. F. Shehata and A. M. El-Shamy, “Hydrogen-based failure in oil and gas pipelines a review,” Jul. 01, 2023, *Elsevier B.V.* doi: 10.1016/j.jgsce.2023.204994.

[127] J. Venezuela *et al.*, “Hydrogen embrittlement of an automotive 1700 MPa martensitic advanced high-strength steel,” *Corros Sci*, vol. 171, Jul. 2020, doi: 10.1016/j.corsci.2020.108726.

[128] I. B. Tuğluca *et al.*, “Lowering Strain Rate Simultaneously Enhances Carbon- and Hydrogen-Induced Mechanical Degradation in an Fe-33Mn-1.1C Steel,” *Metall Mater Trans A Phys Metall Mater Sci*, vol. 50, no. 3, pp. 1137–1141, Mar. 2019, doi: 10.1007/s11661-018-5080-7.

[129] M. F. Kapci *et al.*, “Edge dislocation depinning from hydrogen atmosphere in α-iron,” *Scr Mater*, vol. 247, Jul. 2024, doi: 10.1016/j.scriptamat.2024.116094.

[130] B. Bal, B. Okdem, F. C. Bayram, and M. Aydin, “A detailed investigation of the effect of hydrogen on the mechanical response and microstructure of Al 7075 alloy under medium strain rate impact loading,” *Int J Hydrogen Energy*, vol. 45, no. 46, pp. 25509–25522, Sep. 2020, doi: 10.1016/j.ijhydene.2020.06.241.

[131] H. Najam, M. Koyama, B. Bal, E. Akiyama, and K. Tsuzaki, “Strain rate and hydrogen effects on crack growth from a notch in a Fe-high-Mn steel containing 1.1 wt% solute carbon,” *Int J Hydrogen Energy*, vol. 45, no. 1, pp. 1125–1139, Jan. 2020, doi: 10.1016/j.ijhydene.2019.10.227.

[132] A. Massone *et al.*, “Addressing h-material interaction in fast diffusion materials—a feasibility study on a complex phase steel,” *Materials*, vol. 13, no. 20, pp. 1–20, Oct. 2020, doi: 10.3390/ma13204677.

[133] M. F. Kapci, J. C. Schön, and B. Bal, “The role of hydrogen in the edge dislocation mobility and grain boundary-dislocation interaction in α-Fe,” *Int J Hydrogen Energy*, vol. 46, no. 64, pp. 32695–32709, Sep. 2021, doi: 10.1016/j.ijhydene.2021.07.061.

[134] H. K. Birnbaum and P. Sofronis, “Hydrogen-enhanced localized plasticity-a mechanism for hydrogen-related fracture,” *Materials Science and Engineering*, vol. 176, pp. 191–202, 1994, doi: https://doi.org/10.1016/0921-5093(94)90975-X.

[135] J. Liu, M. Zhao, and L. Rong, “Overview of hydrogen-resistant alloys for high-pressure hydrogen environment: on the hydrogen energy structural materials,” Feb. 01, 2023, *Oxford University Press*. doi: 10.1093/ce/zkad009.

[136] B. Bal, M. Koyama, G. Gerstein, H. J. Maier, and K. Tsuzaki, “Effect of strain rate on hydrogen embrittlement susceptibility of twinning-induced plasticity steel pre-charged with high-pressure hydrogen gas,” *Int J Hydrogen Energy*, vol. 41, no. 34, pp. 15362–15372, Sep. 2016, doi: 10.1016/j.ijhydene.2016.06.259.

[137] B. Bal, I. Sahin, A. Uzun, and D. Canadinc, “A New Venue Toward Predicting the Role of Hydrogen Embrittlement on Metallic Materials,” *Metall Mater Trans A Phys Metall Mater Sci*, vol. 47, no. 11, pp. 5409–5422, Nov. 2016, doi: 10.1007/s11661-016-3708-z.

[138] T. Schuler, F. Christien, P. Ganster, and K. Wolski, “Ab initio investigation of phosphorus and hydrogen co-segregation and embrittlement in α-Fe twin boundaries,” *Appl Surf Sci*, vol. 492, pp. 919–935, Oct. 2019, doi: 10.1016/j.apsusc.2019.04.025.

[139] P. A. T. Olsson, K. Kese, and A. M. Alvarez Holston, “On the role of hydrogen filled vacancies on the embrittlement of zirconium: An ab initio investigation,” *Journal of Nuclear Materials*, vol. 467, pp. 311–319, Dec. 2015, doi: 10.1016/j.jnucmat.2015.09.056.

[140] E. J. McEniry, T. Hickel, and J. Neugebauer, “Ab initio simulation of hydrogen-induced decohesion in cementite-containing microstructures,” *Acta Mater*, vol. 150, pp. 53–58, May 2018, doi: 10.1016/j.actamat.2018.03.005.

[141] V. Tuli, A. Claisse, and P. A. Burr, “Hydrogen solubility in Zr–Nb alloys,” *Scr Mater*, vol. 214, Jun. 2022, doi: 10.1016/j.scriptamat.2022.114652.

[142] J. Song and W. A. Curtin, “Mechanisms of hydrogen-enhanced localized plasticity: An atomistic study using α-Fe as a model system,” *Acta Mater*, vol. 68, pp. 61–69, Apr. 2014, doi: 10.1016/j.actamat.2014.01.008.

[143] M. A. Bhatia, S. Groh, and K. N. Solanki, “Atomic-scale investigation of point defects and hydrogen-solute atmospheres on the edge dislocation mobility in alpha iron,” *J Appl Phys*, vol. 116, no. 6, Aug. 2014, doi: 10.1063/1.4892630.

[144] M. Itakura, H. Kaburaki, M. Yamaguchi, and T. Okita, “The effect of hydrogen atoms on the screw dislocation mobility in bcc iron: A first-principles study,” *Acta Mater*, vol. 61, no. 18, pp. 6857–6867, Oct. 2013, doi: 10.1016/j.actamat.2013.07.064.

[145] C. R. Weinberger, B. L. Boyce, and C. C. Battaile, “Slip planes in bcc transition metals,” 2013, *Maney Publishing*. doi: 10.1179/1743280412Y.0000000015.

[146] S. Queyreau, J. Marian, M. R. Gilbert, and B. D. Wirth, “Edge dislocation mobilities in bcc Fe obtained by molecular dynamics,” *Phys Rev B Condens Matter Mater Phys*, vol. 84, no. 6, Aug. 2011, doi: 10.1103/PhysRevB.84.064106.

[147] G. Monnet and D. Terentyev, “Structure and mobility of the frac(1, 2) < 1 1 1 > {1 1 2} edge dislocation in BCC iron studied by molecular dynamics,” *Acta Mater*, vol. 57, no. 5, pp. 1416–1426, 2009, doi: 10.1016/j.actamat.2008.11.030.

[148] Yu N Osetsky and D J Bacon, “An atomic-level model for studying the dynamics of edge dislocations in metals,” *Model Simul Mat Sci Eng*, vol. 11, no. 4, p. 427, 2003, doi: 10.1088/0965-0393/11/4/302.

[149] Y. Gu and J. A. El-Awady, “Quantifying the effect of hydrogen on dislocation dynamics: A three-dimensional discrete dislocation dynamics framework,” *J Mech Phys Solids*, vol. 112, pp. 491–507, Mar. 2018, doi: 10.1016/j.jmps.2018.01.006.

[150] H. Yu, A. Cocks, and E. Tarleton, “Discrete dislocation plasticity HELPs understand hydrogen effects in bcc materials,” *J Mech Phys Solids*, vol. 123, pp. 41–60, Feb. 2019, doi: 10.1016/j.jmps.2018.08.020.

[151] M. Wen, “A new interatomic potential describing Fe-H and H-H interactions in bcc iron,” *Comput Mater Sci*, vol. 197, Sep. 2021, doi: 10.1016/j.commatsci.2021.110640.

[152] M. I. Mendelev, S. Han, D. J. Srolovitz, G. J. Ackland, D. Y. Sun, and M. Asta, “Development of new interatomic potentials appropriate for crystalline and liquid iron,” *Philosophical Magazine*, vol. 83, no. 35, pp. 3977–3994, Dec. 2003, doi: 10.1080/14786430310001613264.

[153] S. Peng *et al.*, “Influence of hydrogen volume/specimen surface area ratio on hydrogen embrittlement sensitivity of X52 pipeline steel,” *International Journal of Pressure Vessels and Piping*, vol. 209, p. 105217, 2024, doi: https://doi.org/10.1016/j.ijpvp.2024.105217.

[154] D. Zheng *et al.*, “Molecular dynamics investigations into the hydrogen permeation mechanism of polyethylene pipeline material,” *J Mol Liq*, vol. 368, p. 120773, 2022, doi: https://doi.org/10.1016/j.molliq.2022.120773.

[155] J. Shen, X. Shen, J. Zhou, W. Yue, and T. Zhang, “Molecular dynamics simulation of fatigue damage formation in single-crystal/polycrystalline aluminum,” *Mater Today Commun*, vol. 39, p. 109138, 2024, doi: https://doi.org/10.1016/j.mtcomm.2024.109138.

[156] Y. Jiao, W. Dan, and W. Zhang, “Effects of hydrogen on the deformation mechanism of face-centred cubic Fe–C single crystal with nanovoid: A molecular dynamics simulation,” *J Alloys Compd*, vol. 870, p. 159330, 2021, doi: https://doi.org/10.1016/j.jallcom.2021.159330.

[157] D. Zheng *et al.*, “Grand canonical Monte Carlo and molecular dynamics investigation of hydrogen solubility and diffusivity in nonmetallic polyvinyl chloride,

polyethylene and polyvinylidene fluoride pipes materials," *Fuel*, vol. 362, p. 130925, 2024, doi: https://doi.org/10.1016/j.fuel.2024.130925.

[158] T. H. Xu, Z. Q. Zhu, S. F. Geng, and H. Y. Song, "Molecular dynamics study of effect of hydrogen atoms on mechanical properties of α-Fe nanowires," *Phys Lett A*, vol. 381, no. 37, pp. 3222–3227, 2017, doi: https://doi.org/10.1016/j.physleta.2017.08.012.

[159] L. Li *et al.*, "Hydrogen behavior during high-temperature plastic deformation in low-alloy steels," *J Mater Process Technol*, vol. 302, p. 117487, 2022, doi: https://doi.org/10.1016/j.jmatprotec.2021.117487.

[160] H. Y. Song, L. Zhang, and M. X. Xiao, "Molecular dynamics simulation of effect of hydrogen atoms on crack propagation behavior of α-Fe," *Phys Lett A*, vol. 380, no. 48, pp. 4049–4056, 2016, doi: https://doi.org/10.1016/j.physleta.2016.10.019.

[161] R. Wang, L. Cheng, C. Yin, W. Lou, and K. Wu, "The effects of hydrogen and vacancy on the tensile deformation behavior of Σ3 symmetric tilt grain boundaries in pure fe," *Int J Hydrogen Energy*, vol. 48, no. 79, pp. 30930–30948, 2023, doi: https://doi.org/10.1016/j.ijhydene.2023.04.186.

[162] L. Wan *et al.*, "Hydrogen embrittlement controlled by reaction of dislocation with grain boundary in alpha-iron," *Int J Plast*, vol. 112, pp. 206–219, 2019, doi: https://doi.org/10.1016/j.ijplas.2018.08.013.

[163] A. Stukowski, "Visualization and analysis of atomistic simulation data with OVITO–the Open Visualization Tool," *Model Simul Mat Sci Eng*, vol. 18, no. 1, p. 015012, 2010, doi: 10.1088/0965-0393/18/1/015012.

[164] A. Stukowski, V. V Bulatov, and A. Arsenlis, "Automated identification and indexing of dislocations in crystal interfaces," *Model Simul Mat Sci Eng*, vol. 20, no. 8, p. 085007, 2012, doi: 10.1088/0965-0393/20/8/085007.

[165] D. J. Bacon, Y. N. Osetsky, and D. Rodney, "Chapter 88 Dislocation–Obstacle Interactions at the Atomic Level," in *Dislocations in Solids*, vol. 15, J. P. Hirth and L. Kubin, Eds., Elsevier, 2009, pp. 1–90. doi: https://doi.org/10.1016/S1572-4859(09)01501-0.

[166] W. Xie, X. Liu, W. Chen, and H. Zhang, "Hydrogen hardening effect in heavily deformed single crystal α-Fe," *Comput Mater Sci*, vol. 50, no. 12, pp. 3397–3402, Dec. 2011, doi: 10.1016/j.commatsci.2011.06.036.

[167] D. Sasaki, Y. Kusaba, and M. Koyama, "Hydrogen-assisted localized plasticity driven by dislocation pinning-depinning: Finite element simulations," *Int J Hydrogen Energy*, vol. 56, pp. 280–288, Feb. 2024, doi: 10.1016/j.ijhydene.2023.12.053.

[168] S. Wang, N. Hashimoto, and S. Ohnuki, "Hydrogen-induced change in core structures of {110}[111] edge and {110}[111] screw dislocations in iron," *Sci Rep*, vol. 3, 2013, doi: 10.1038/srep02760.

[169] D. N. Blaschke, L. Burakovsky, and D. L. Preston, "On the temperature and density dependence of dislocation drag from phonon wind," *J Appl Phys*, vol. 130, no. 1, Jul. 2021, doi: 10.1063/5.0054536.

[170] A. Y. Kuksin and A. V. Yanilkin, "Atomistic simulation of the motion of dislocations in metals under phonon drag conditions," *Physics of the Solid State*, vol. 55, no. 5, pp. 1010–1019, May 2013, doi: 10.1134/S1063783413050193.

[171] A. Hikata, R. A. Johnson, and C. Elbaum, “Interaction of Dislocations with Electrons and with Phonons,” *Phys Rev B*, vol. 2, no. 12, pp. 4856–4863, Dec. 1970, doi: 10.1103/PhysRevB.2.4856.

[172] R. Matsumoto, S. T. Oyinbo, M. Vijendran, and S. Taketomi, “Hydrogen Effect on the Mobility of Edge Dislocation in α-Iron: A Long-Timescale Molecular Dynamics Simulation,” *ISIJ International*, vol. 62, no. 11, pp. 2402–2409, 2022, doi: 10.2355/isijinternational.ISIJINT-2022-311.

[173] M. S. Hasan, M. F. Kapci, B. Bal, M. Koyama, H. Bayat, and W. Xu, “An atomistic study on the HELP mechanism of hydrogen embrittlement in pure metal Fe,” *Int J Hydrogen Energy*, vol. 57, pp. 60–68, Feb. 2024, doi: 10.1016/j.ijhydene.2023.12.274.

APPENDİX

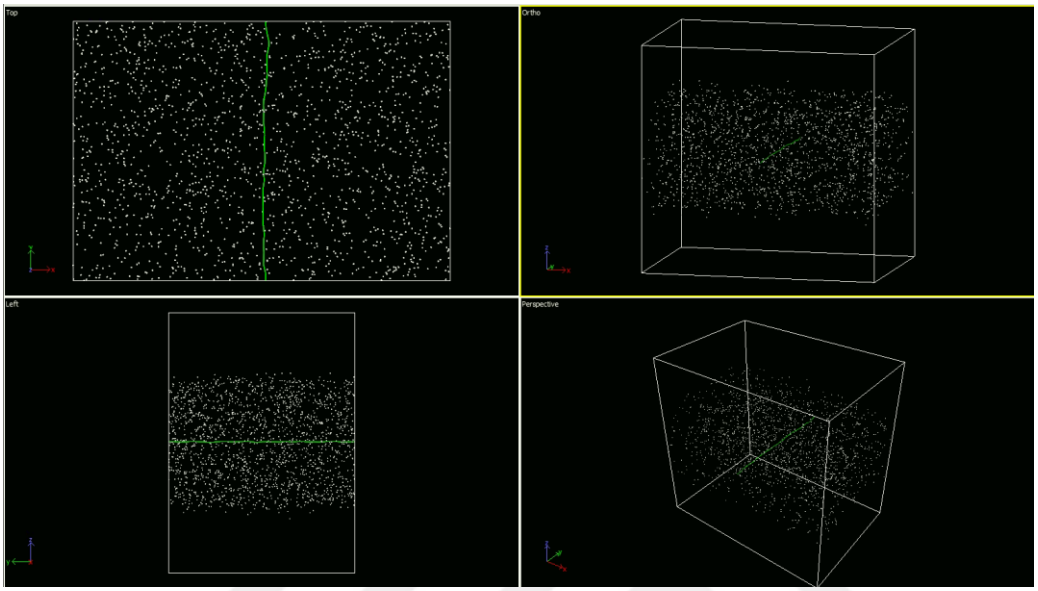

Supplementary Figure 1 Atom distribution in the simulation cell with a {110} glide plane at 100 K temperature and 0.25% H/Fe concentration. The simulation cell depicted here shows the relaxation condition at 0.2 ns. Green line represents the dislocation, while white points represent the hydrogen atoms [120].

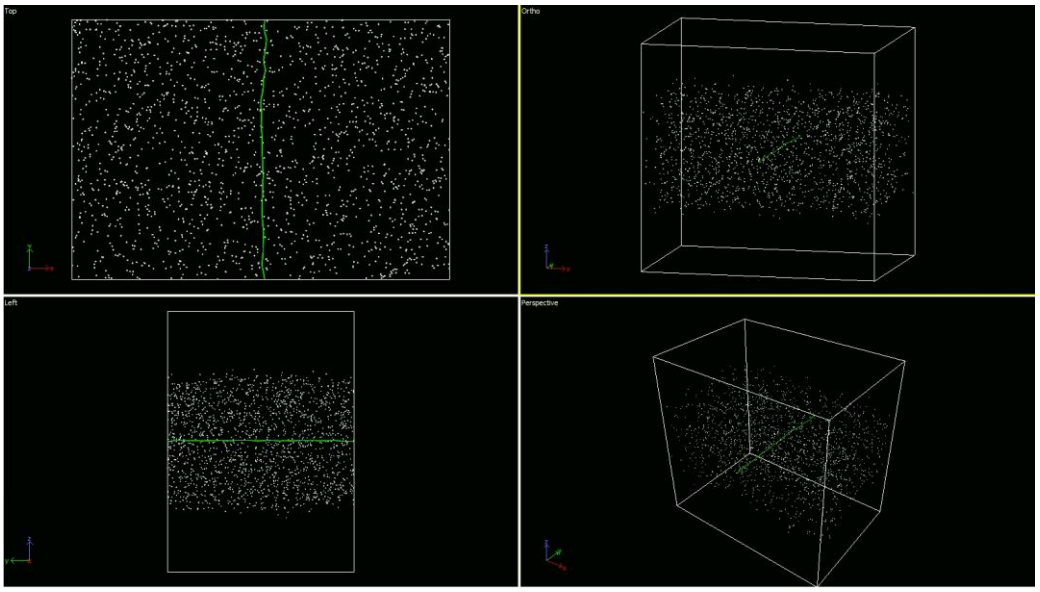

Supplementary Figure 2 Atom distribution in the simulation cell with a {110} glide plane at 100 K temperature and 0.25% H/Fe concentration. The simulation cell depicted here shows the relaxation condition at 0.3 ns. Green line represents the dislocation, while white points represent the hydrogen atoms [120].

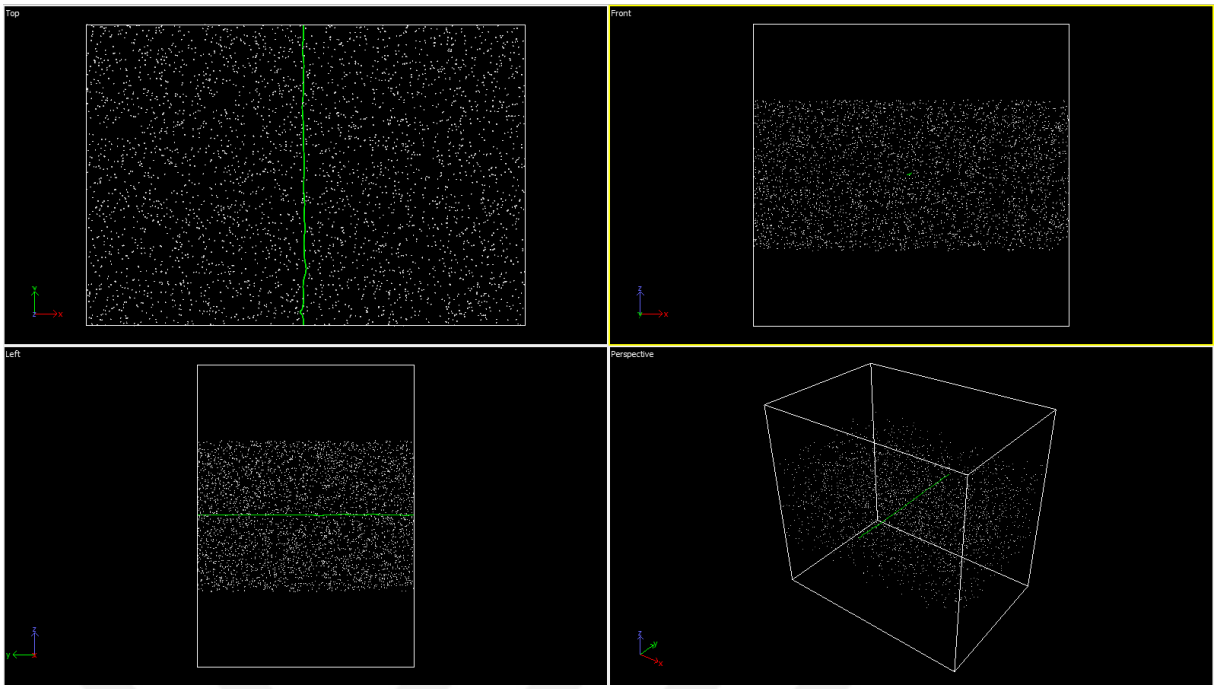

Supplementary Figure 3 Atom distribution in the simulation cell with a {110} glide plane at 100 K temperature and 0.5% H/Fe concentration. The simulation cell depicted here shows the configuration before relaxation. Green line represents the dislocation, while white points represent the hydrogen atoms [120].

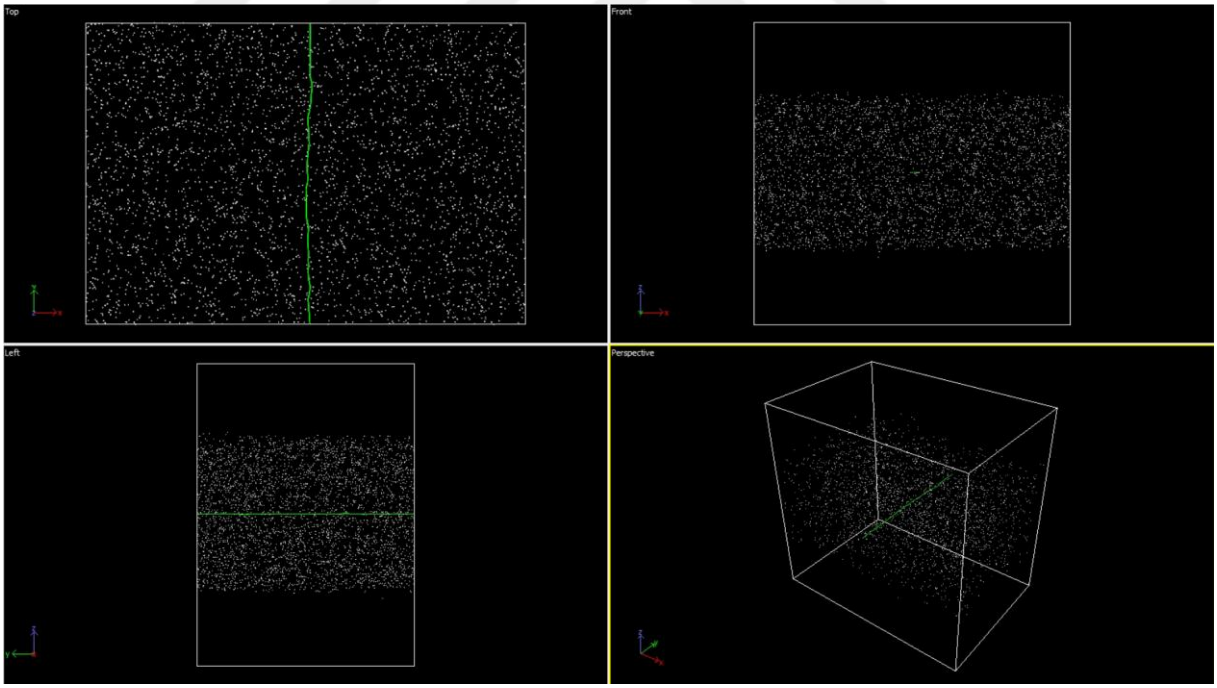

Supplementary Figure 4 Supplementary Figure 4. Atom distribution in the simulation cell with a {110} glide plane at 100 K temperature and 0.5% H/Fe concentration. The simulation cell depicted here shows the configuration after relaxation. Green line represents the dislocation, while white points represent the hydrogen atoms [120].

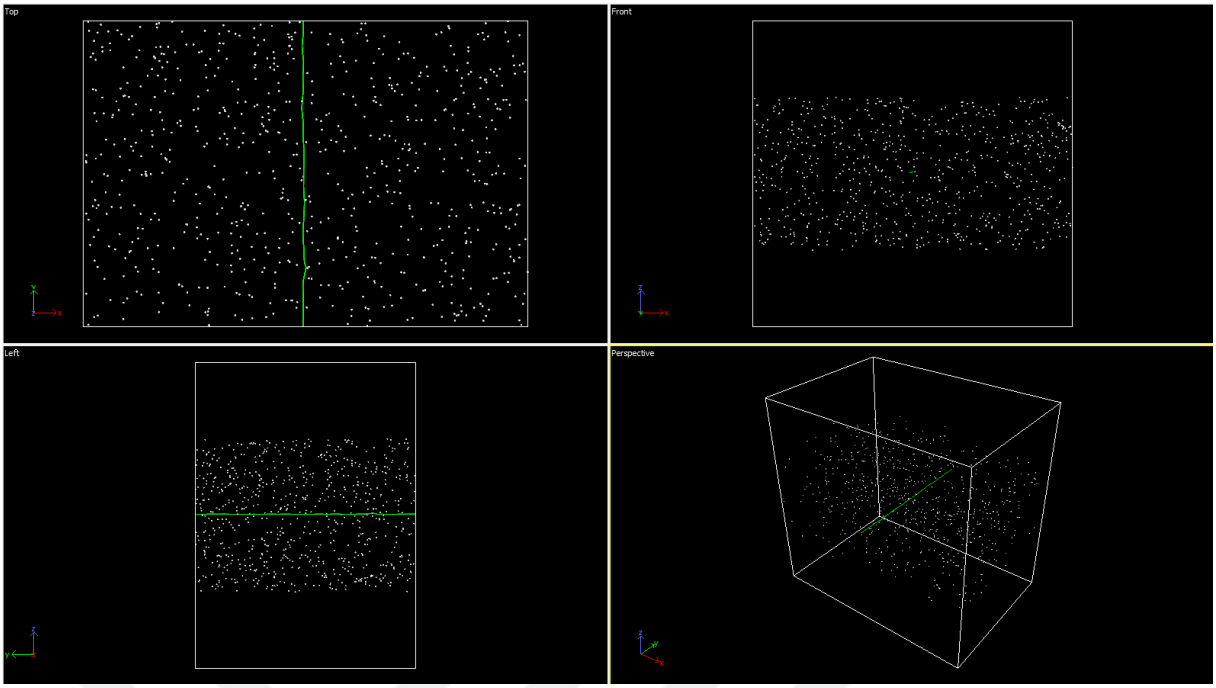

Supplementary Figure 5 Atom distribution in the simulation cell with a {110} glide plane at 50 K temperature and 0.1% H/Fe concentration. The simulation cell depicted here shows the configuration before relaxation. Green line represents the dislocation, while white points represent the hydrogen atoms [120].

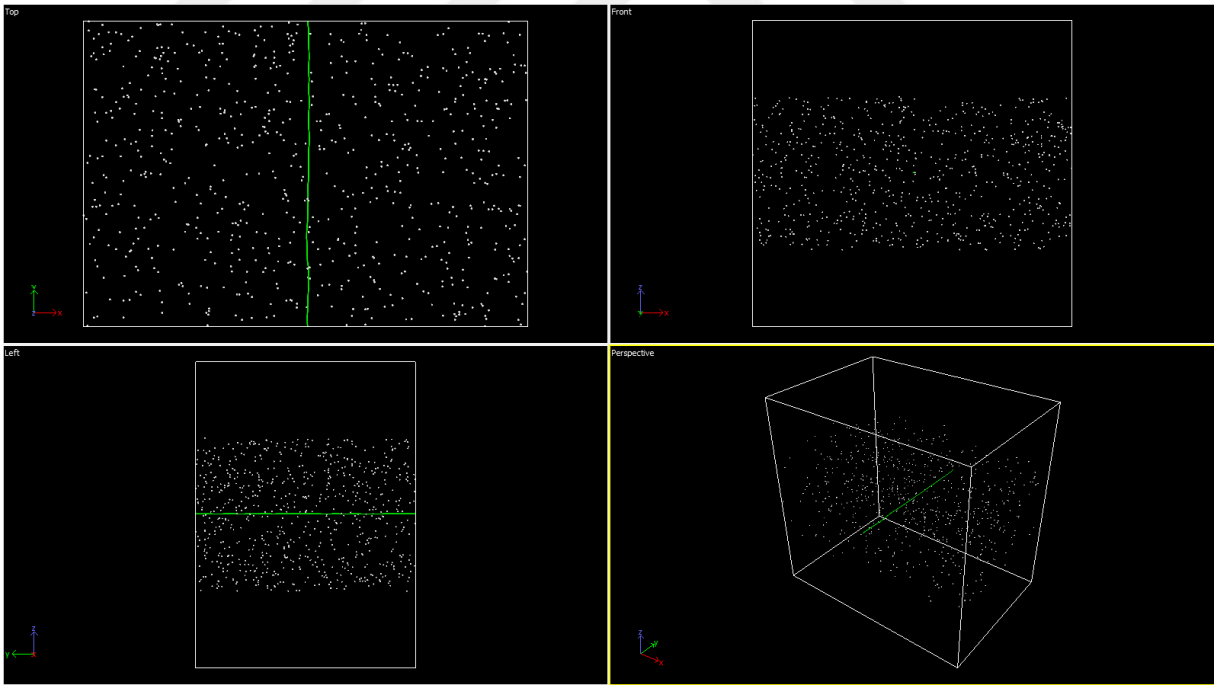

Supplementary Figure 6 Atom distribution in the simulation cell with a {110} glide plane at 50 K temperature and 0.1% H/Fe concentration. The simulation cell depicted here shows the configuration after relaxation. Green line represents the dislocation, while white points represent the hydrogen atoms [120].

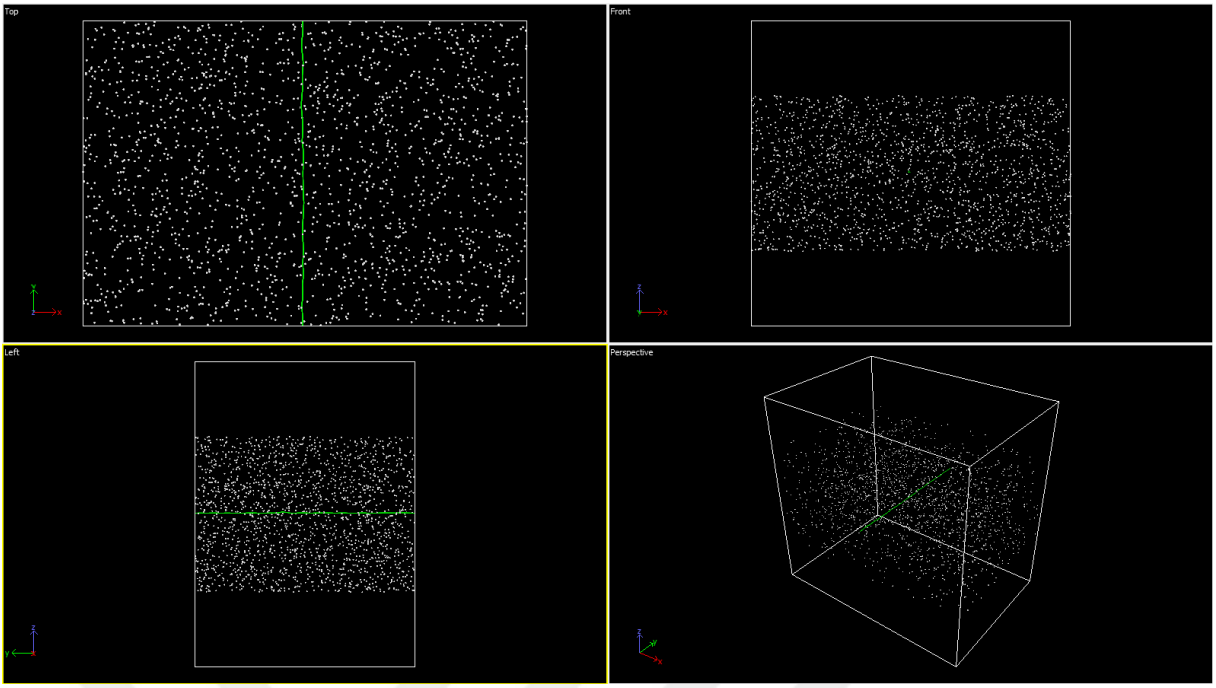

Supplementary Figure 7 Atom distribution in the simulation cell with a {110} glide plane at 50 K temperature and 0.25% H/Fe concentration. The simulation cell depicted here shows the configuration before relaxation. Green line represents the dislocation, while white points represent the hydrogen atoms [120].

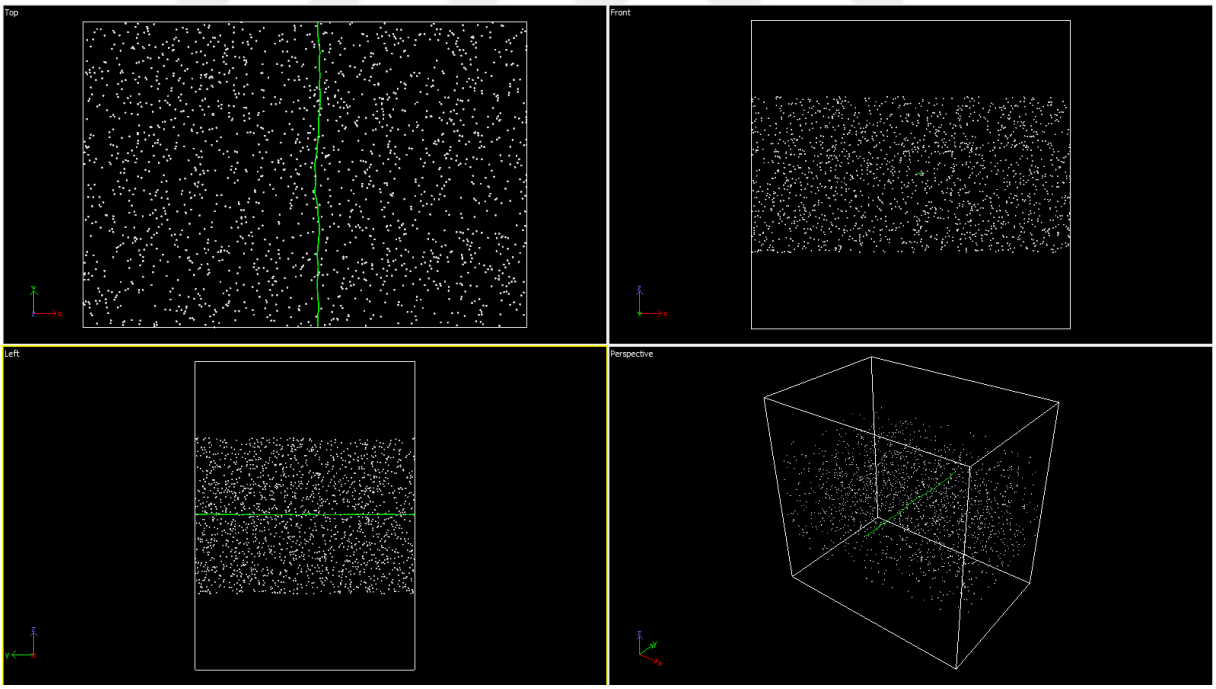

Supplementary Figure 8 Atom distribution in the simulation cell with a {110} glide plane at 50 K temperature and 0.25% H/Fe concentration. The simulation cell depicted here shows the configuration after relaxation. Green line represents the dislocation, while white points represent the hydrogen atoms [120].

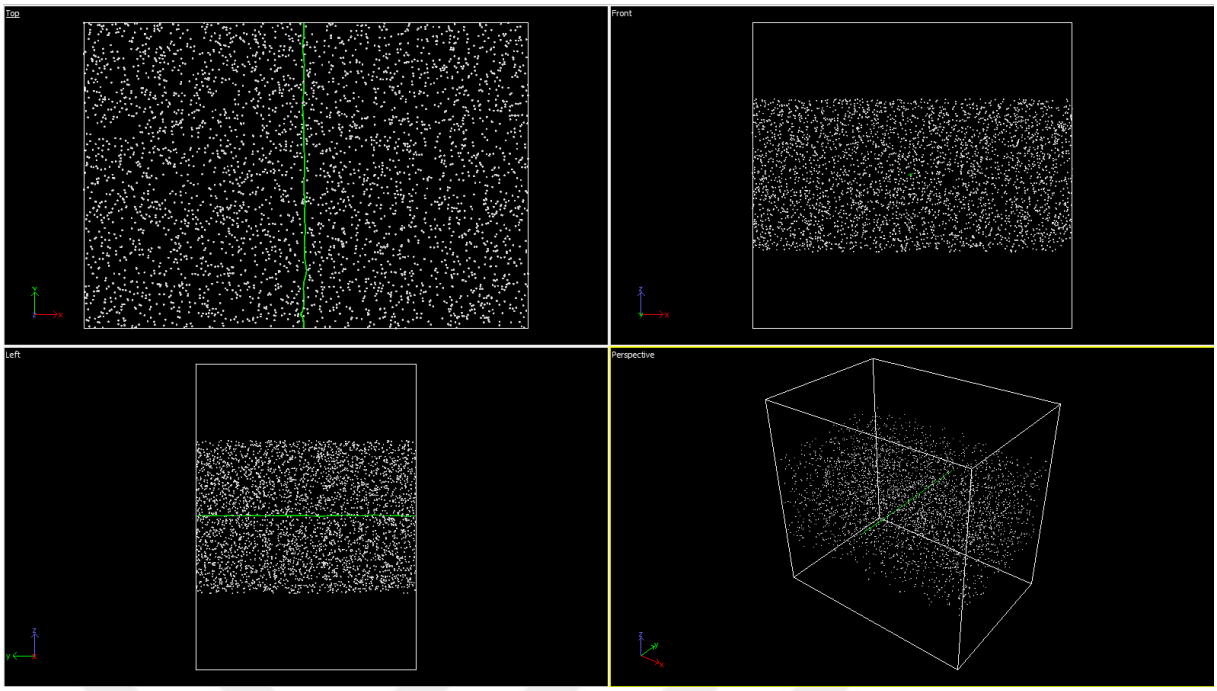

Supplementary Figure 9 Atom distribution in the simulation cell with a {110} glide plane at 50 K temperature and 0.5% H/Fe concentration. The simulation cell depicted here shows the configuration before relaxation. Green line represents the dislocation, while white points represent the hydrogen atoms [120].

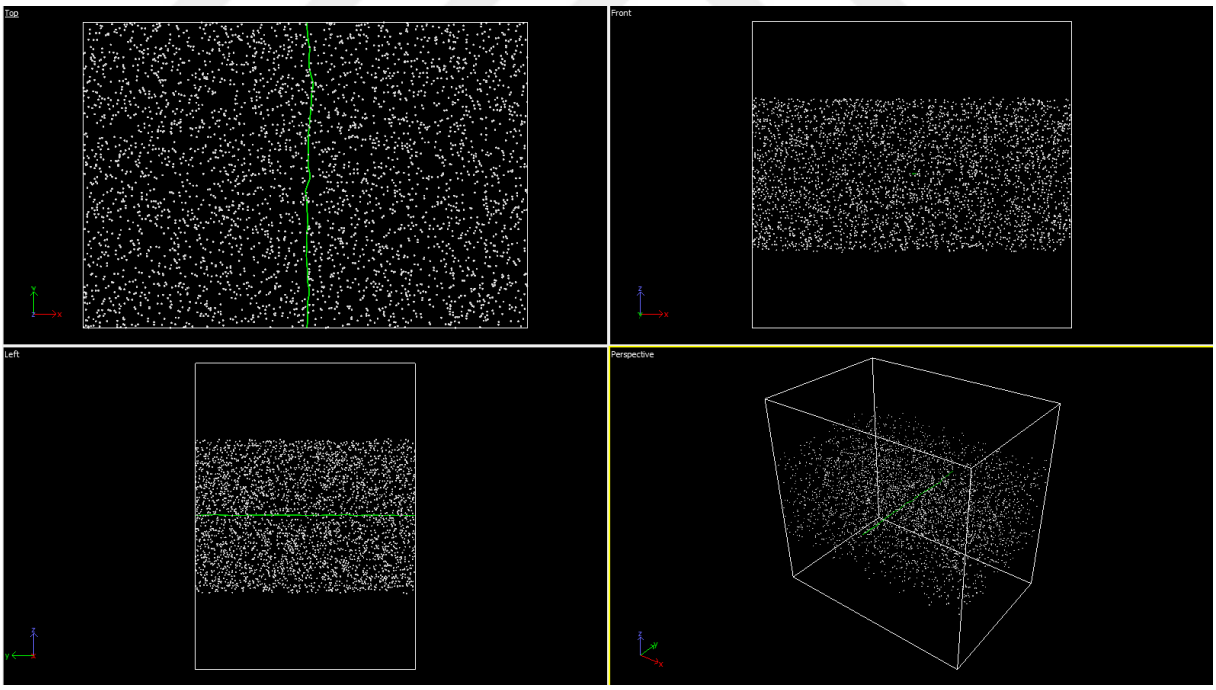

Supplementary Figure 10 Atom distribution in the simulation cell with a {110} glide plane at 50 K temperature and 0.5% H/Fe concentration. The simulation cell depicted here shows the configuration after relaxation. Green line represents the dislocation, while white points represent the hydrogen atoms [120].

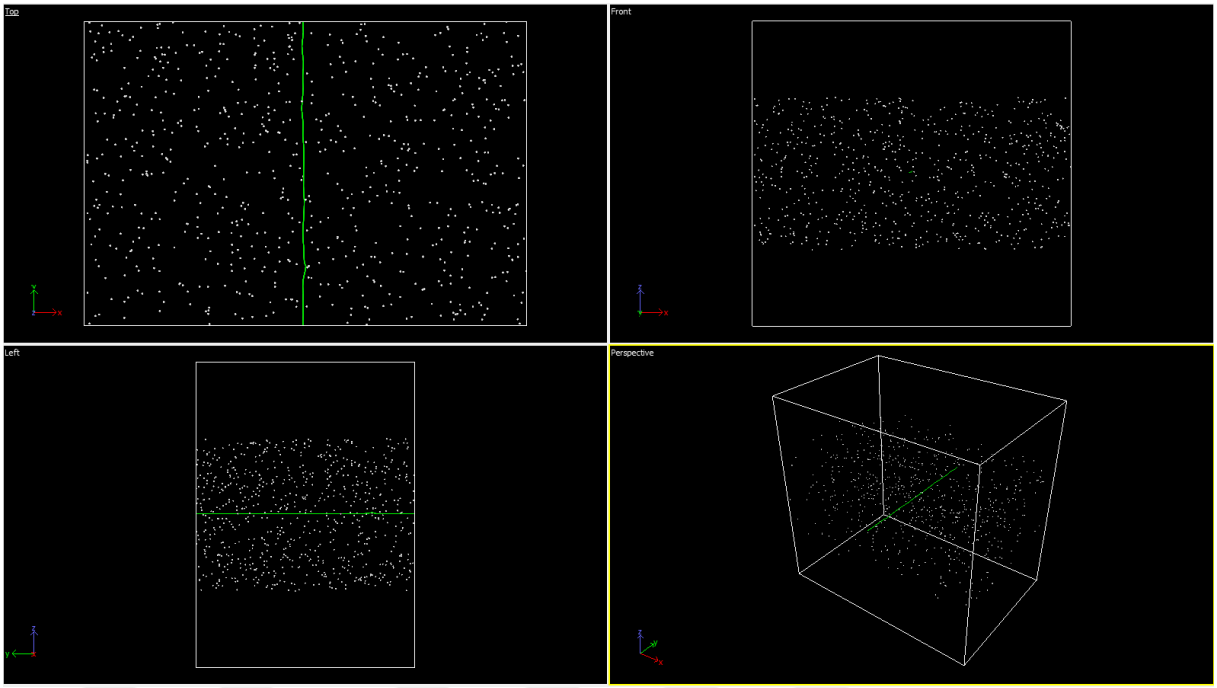

Supplementary Figure 11 Atom distribution in the simulation cell with a {110} glide plane at 400 K temperature and 0.1% H/Fe concentration. The simulation cell depicted here shows the configuration before relaxation. Green line represents the dislocation, while white points represent the hydrogen atoms [120].

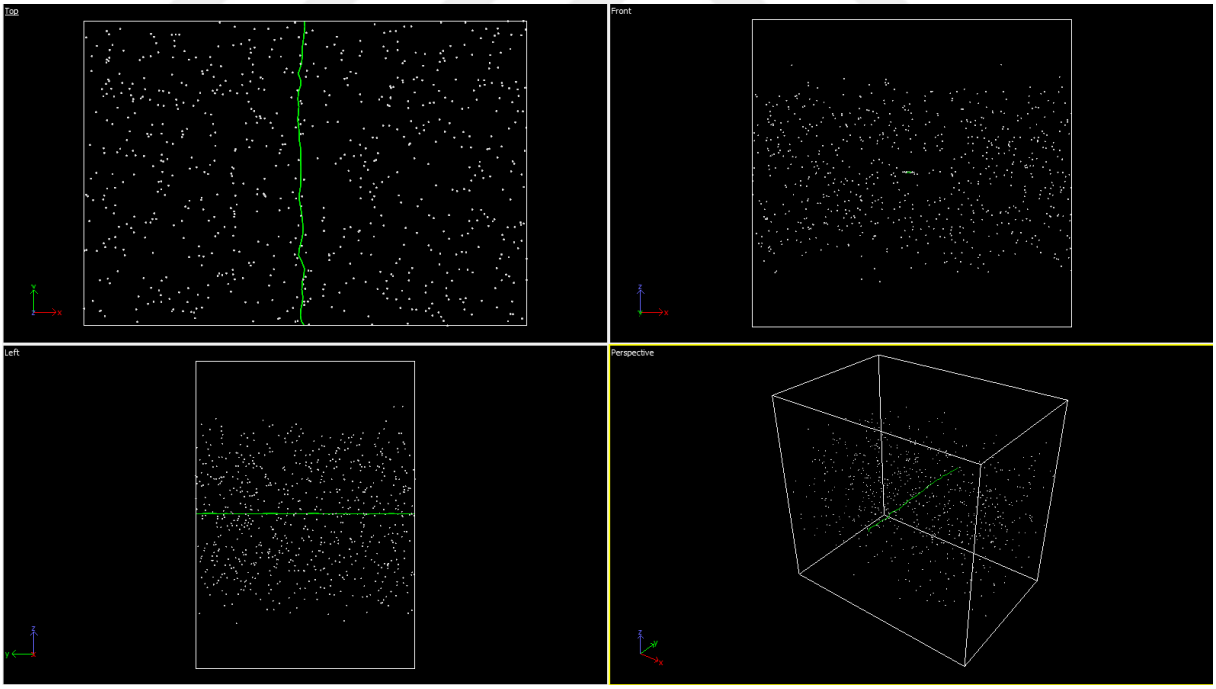

Supplementary Figure 12 Atom distribution in the simulation cell with a {110} glide plane at 400 K temperature and 0.1% H/Fe concentration. The simulation cell depicted here shows the configuration after relaxation. Green line represents the dislocation, while white points represent the hydrogen atoms [120].

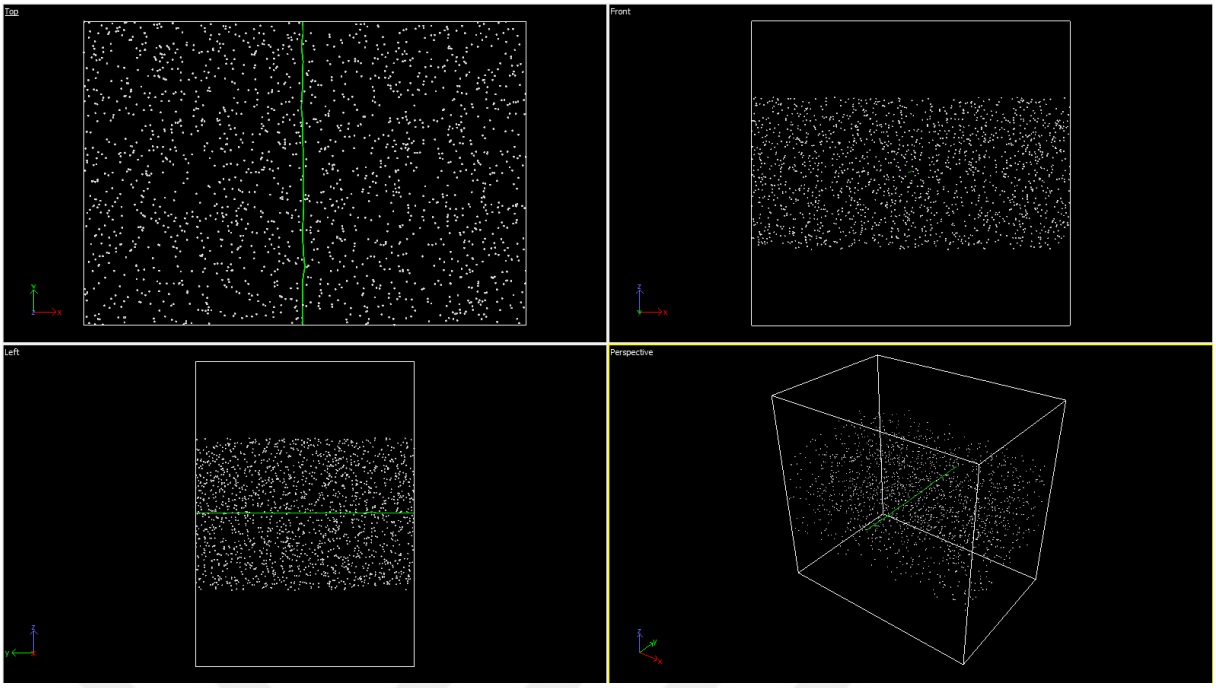

Supplementary Figure 13 Atom distribution in the simulation cell with a {110} glide plane at 400 K temperature and 0.25% H/Fe concentration. The simulation cell depicted here shows the configuration before relaxation. Green line represents the dislocation, while white points represent the hydrogen atoms [120].

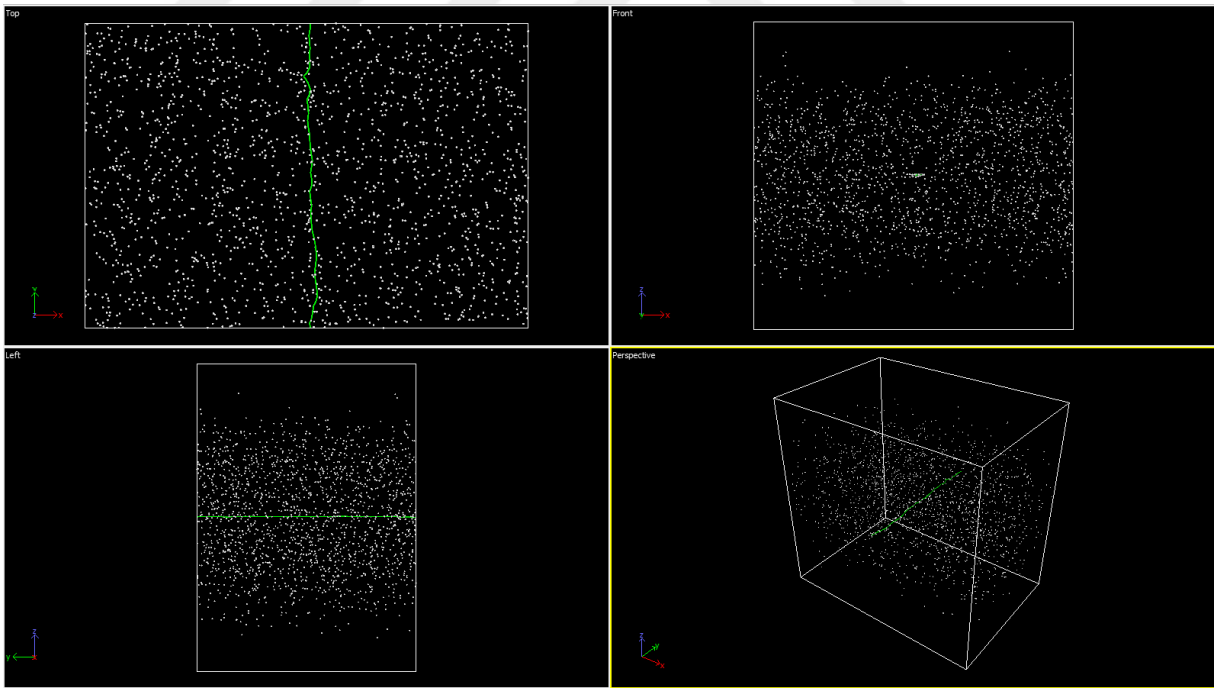

Supplementary Figure 14 Atom distribution in the simulation cell with a {110} glide plane at 400 K temperature and 0.25% H/Fe concentration. The simulation cell depicted here shows the configuration after relaxation. Green line represents the dislocation, while white points represent the hydrogen atoms [120].

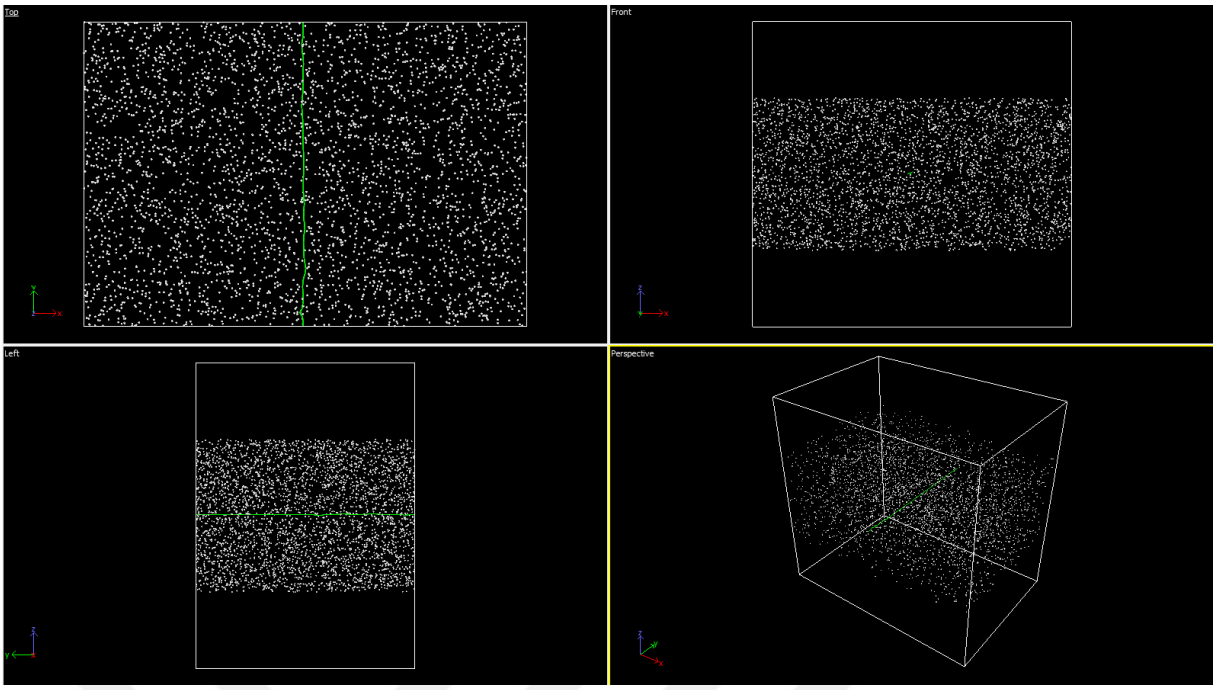

Supplementary Figure 15 Atom distribution in the simulation cell with a {110} glide plane at 400 K temperature and 0.5% H/Fe concentration. The simulation cell depicted here shows the configuration before relaxation. Green line represents the dislocation, while white points represent the hydrogen atoms [120].

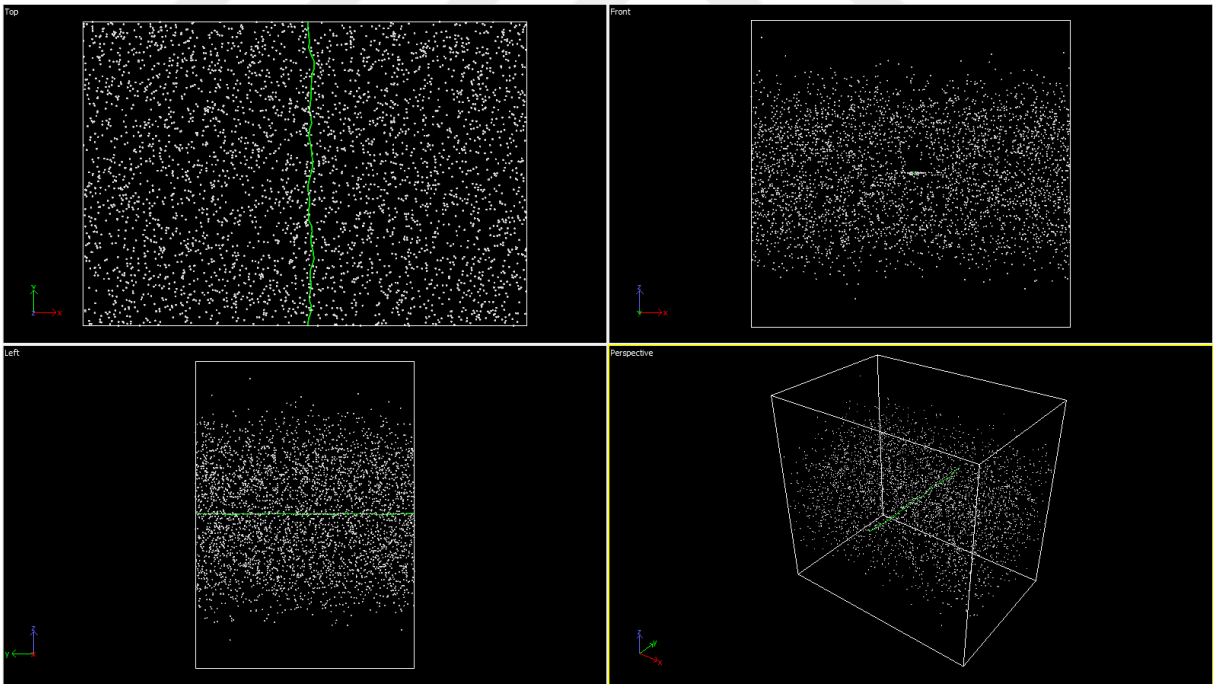

Supplementary Figure 16 Atom distribution in the simulation cell with a {110} glide plane at 400 K temperature and 0.5% H/Fe concentration. The simulation cell depicted here shows the configuration after relaxation. Green line represents the dislocation, while white points represent the hydrogen atoms [120].

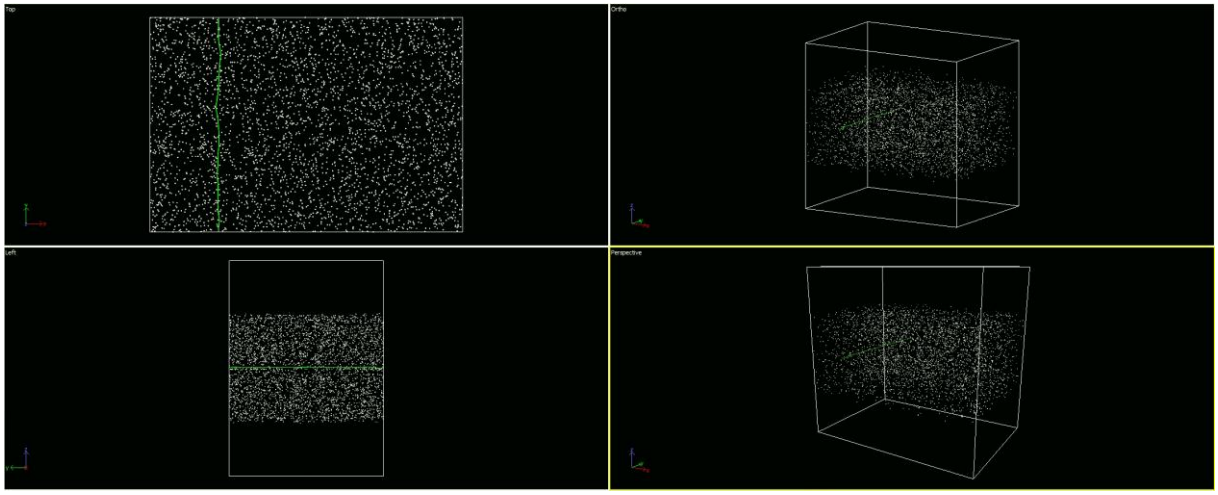

Supplementary Figure 17 The hydrogen distribution during dislocation movement on the {110} glide plane at 100K and 600 MPa with a 0.5% H/Fe concentration at 0.5 ns simulation time. Green line represents the dislocation and, white points represent the hydrogen atoms [120].

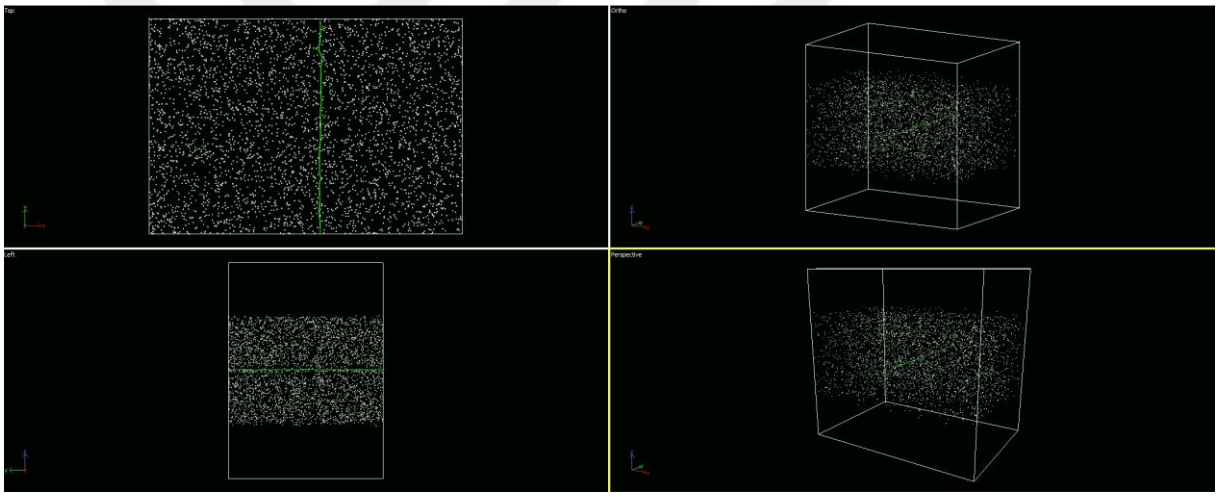

Supplementary Figure 18 The hydrogen distribution during dislocation movement on the {110} glide plane at 100K and 600 MPa with a 0.5% H/Fe concentration at 0.75 ns simulation time. Green line represents the dislocation and, white points represent the hydrogen atoms [120].

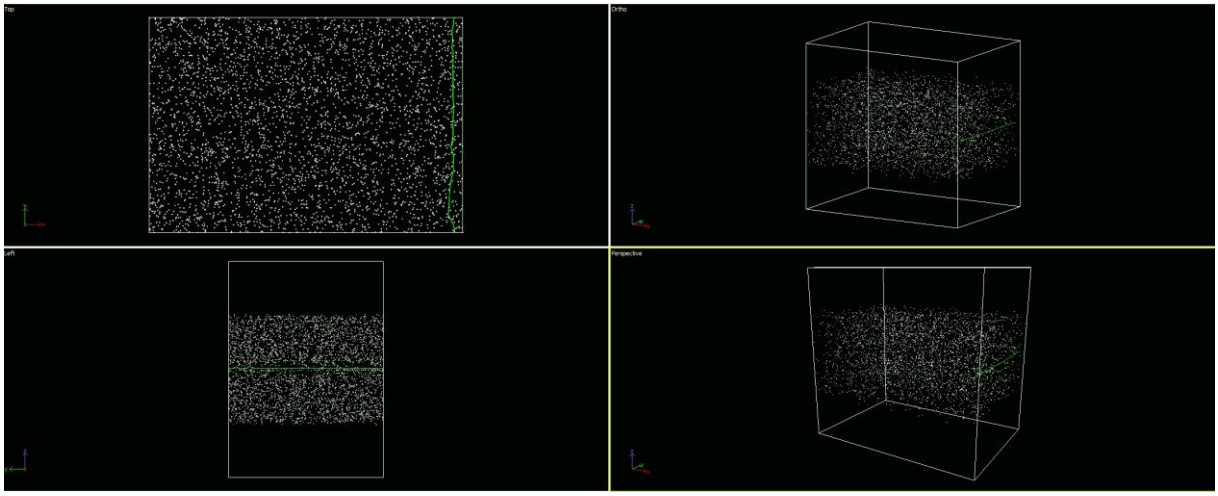

Supplementary Figure 19 The hydrogen distribution during dislocation movement on the {110} glide plane at 100K and 600 MPa with a 0.5% H/Fe concentration at 1 ns simulation time. Green line represents the dislocation and, white points represent the hydrogen atoms [120].

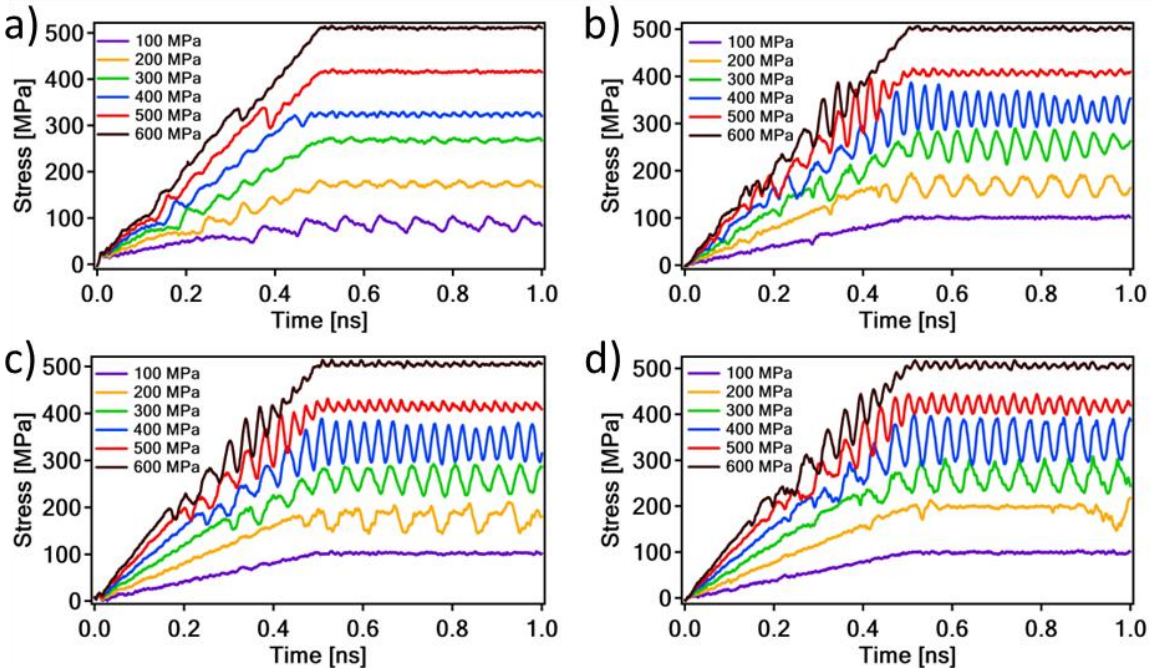

Supplementary Figure 20 Stress vs time graphs of 50K temperature for {110} plane. Here, a) shows the pure iron case (0% H/Fe), b) shows %0.1 H/Fe concentration, c) shows 0.25% H/Fe concentration d) shows 0.5% H/Fe concentration [120].

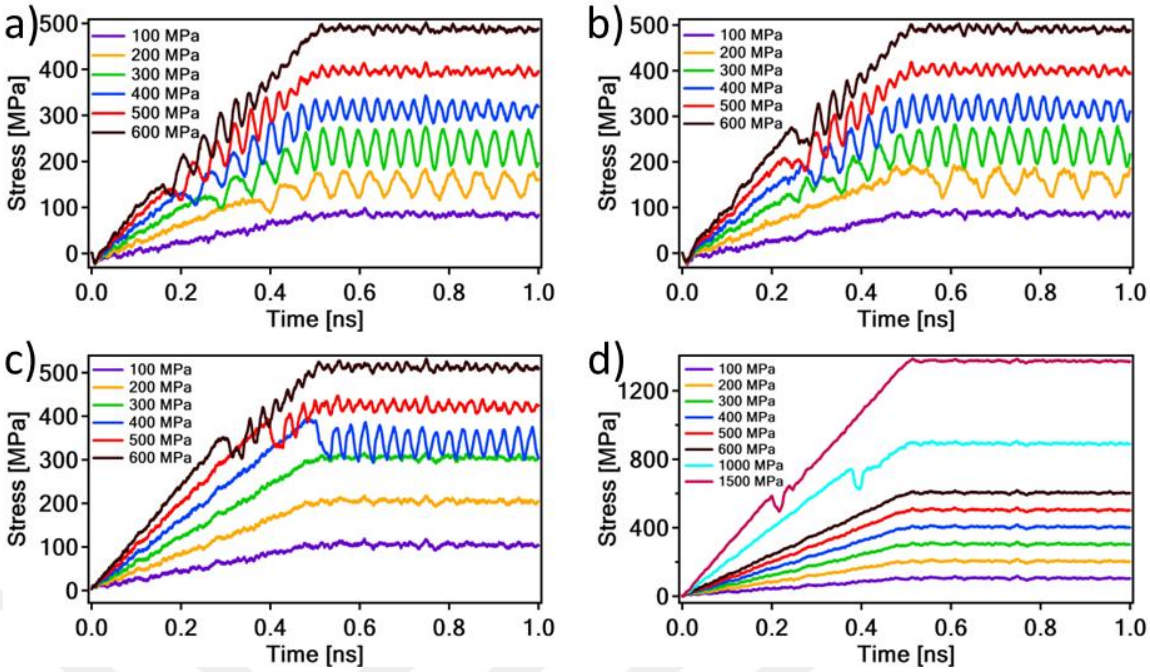

Supplementary Figure 21 Stress vs time graphs of 200K temperature for {110} plane. Here, a) shows the pure iron case (0% H/Fe), b) shows %0.1 H/Fe concentration, c) shows 0.25% H/Fe concentration d) shows 0.5% H/Fe concentration [120].

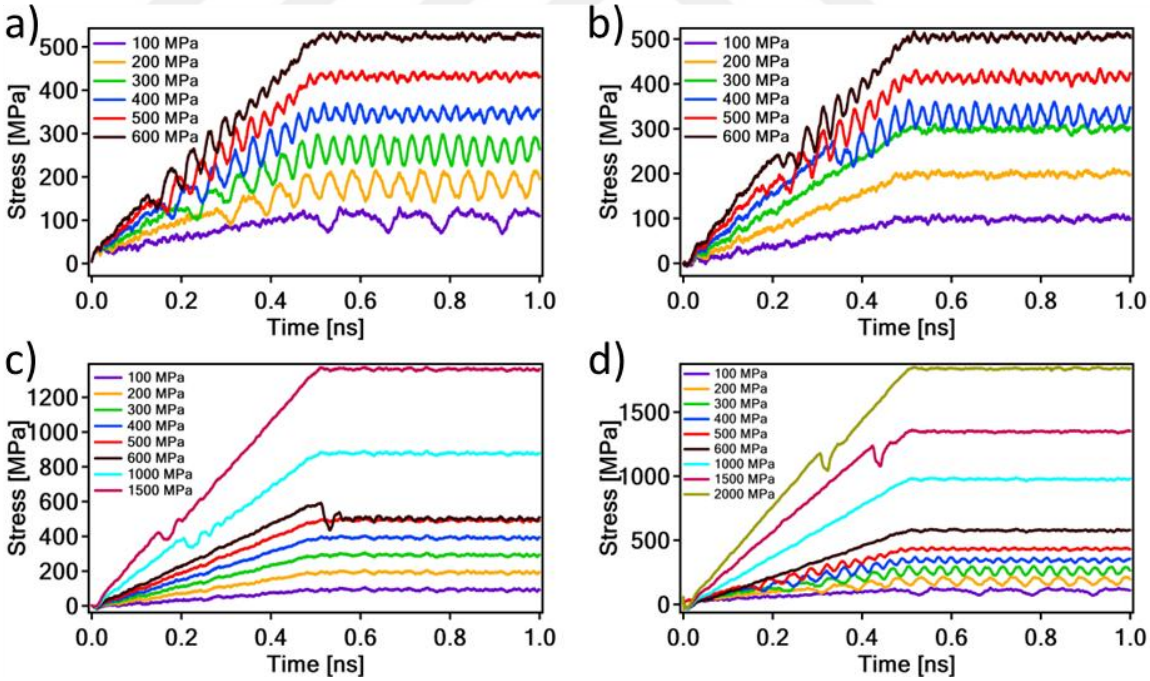

Supplementary Figure 22 Stress vs time graphs of 300K temperature for {110} plane. Here, a) shows the pure iron case (0% H/Fe), b) shows 0.1% H/Fe concentration, c) shows 0.25% H/Fe concentration d) shows 0.5% H/Fe concentration [120].

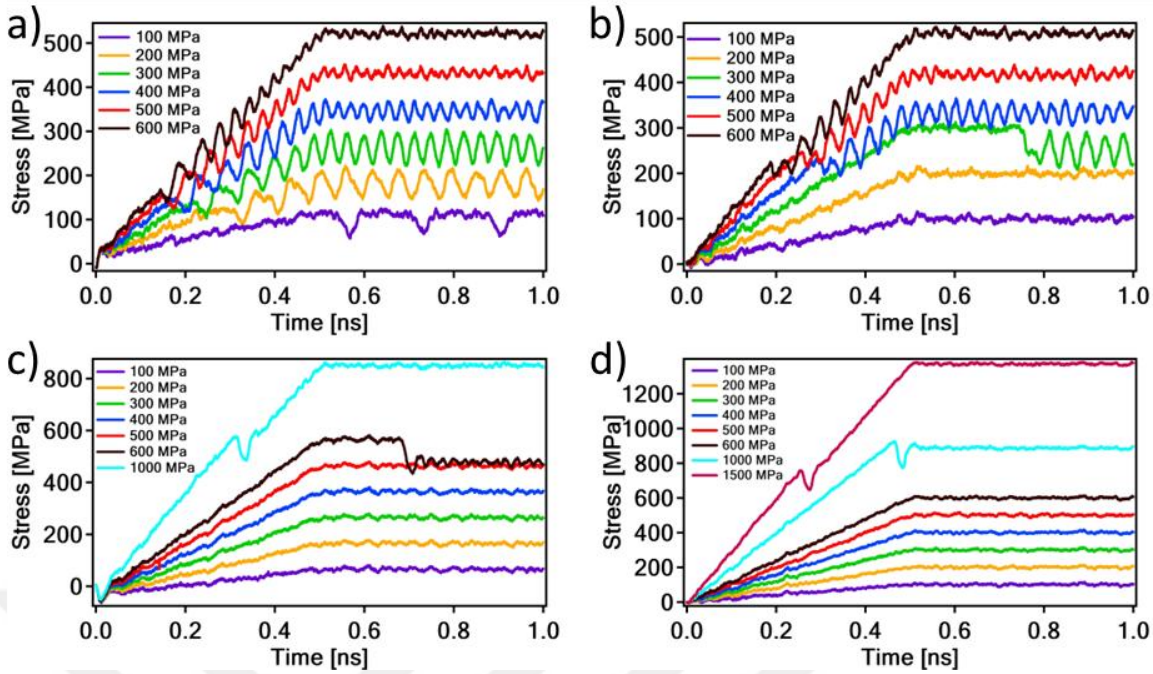

Supplementary Figure 23 Stress vs time graphs of 400K temperature for {110} plane. Here, a) shows the pure iron case (0% H/Fe), b) shows 0.1% H/Fe concentration, c) shows 0.25% H/Fe concentration d) shows 0.5% H/Fe concentration [120].

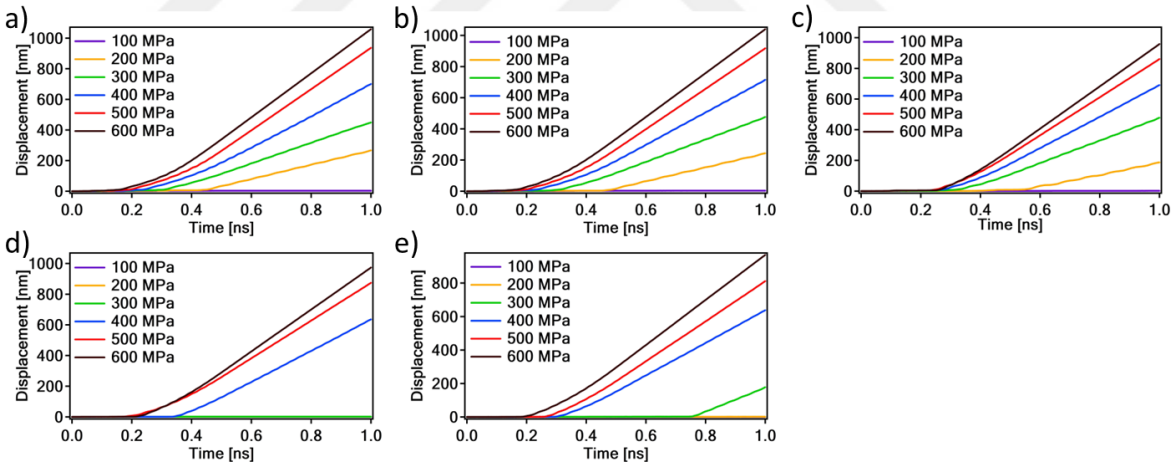

Supplementary Figure 24 Displacement vs time graphs of 0.1% H/Fe concentration cases. Here, starting from a) to e), graphs show the simulation results of 50K, 100K, 200K, 300K, 400K correspondingly [120].

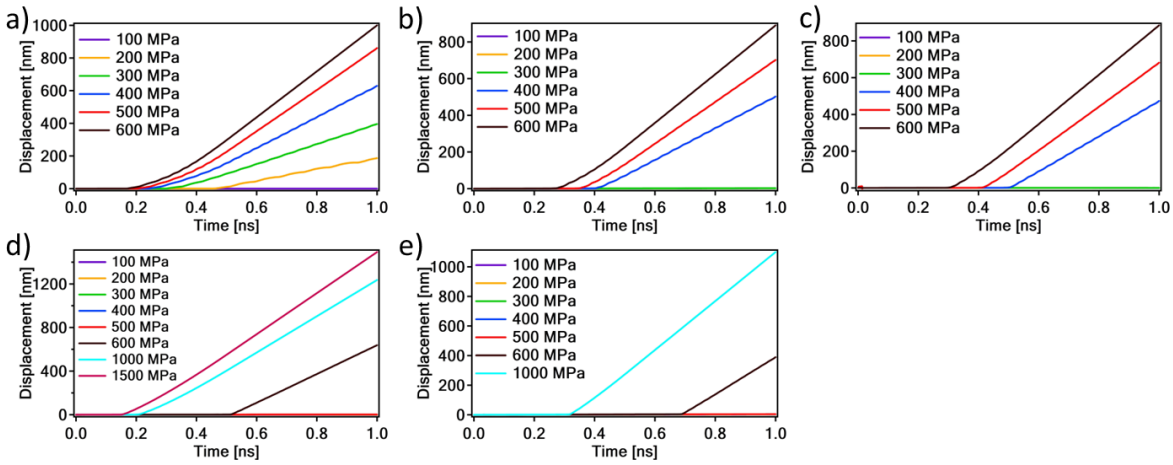

Supplementary Figure 25 Displacement vs time graphs of 0.25% H/Fe concentration cases. Here, starting from a) to e), graphs show the simulation results of 50K, 100K, 200K, 300K, 400K correspondingly [120].

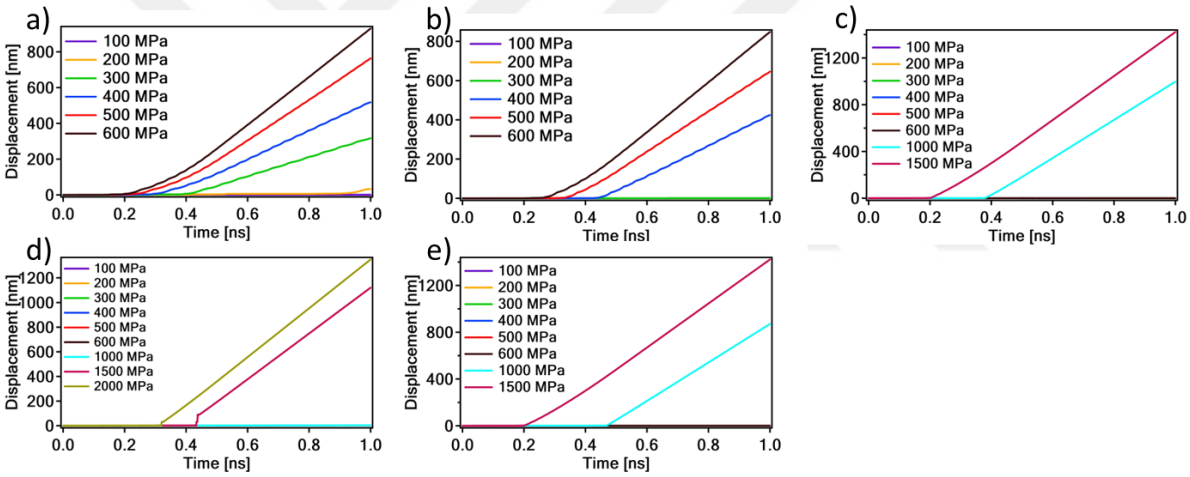

Supplementary Figure 26 Displacement vs time graphs of 0.5% H/Fe concentration cases. Here, starting from a) to e), graphs show the simulation results of 50K, 100K, 200K, 300K, 400K correspondingly [120].

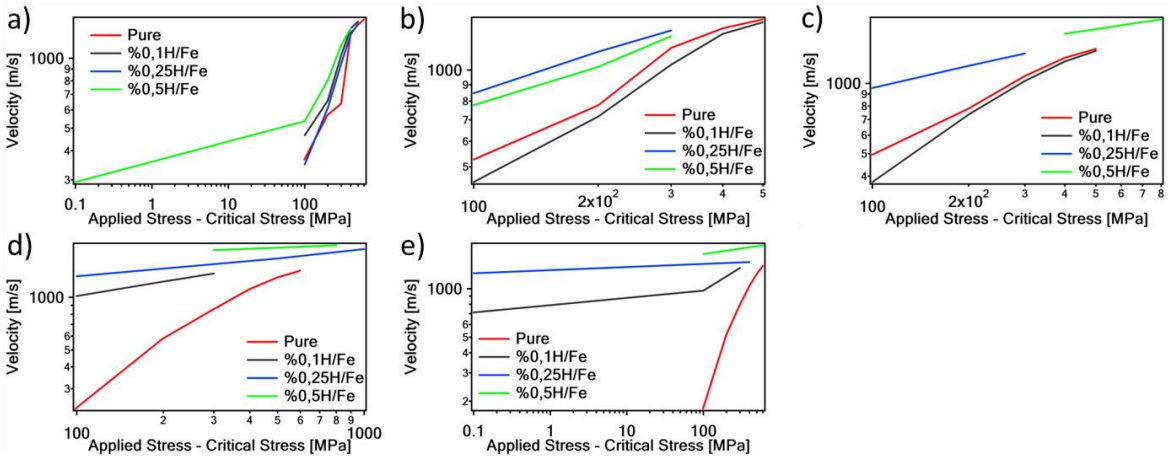

Supplementary Figure 27 Relationship of difference between applied and critical stress and velocity of dislocation at different temperatures. Here, starting from a) to e), graphs show the simulation results of 50K, 100K, 200K, 300K, 400K correspondingly [120].

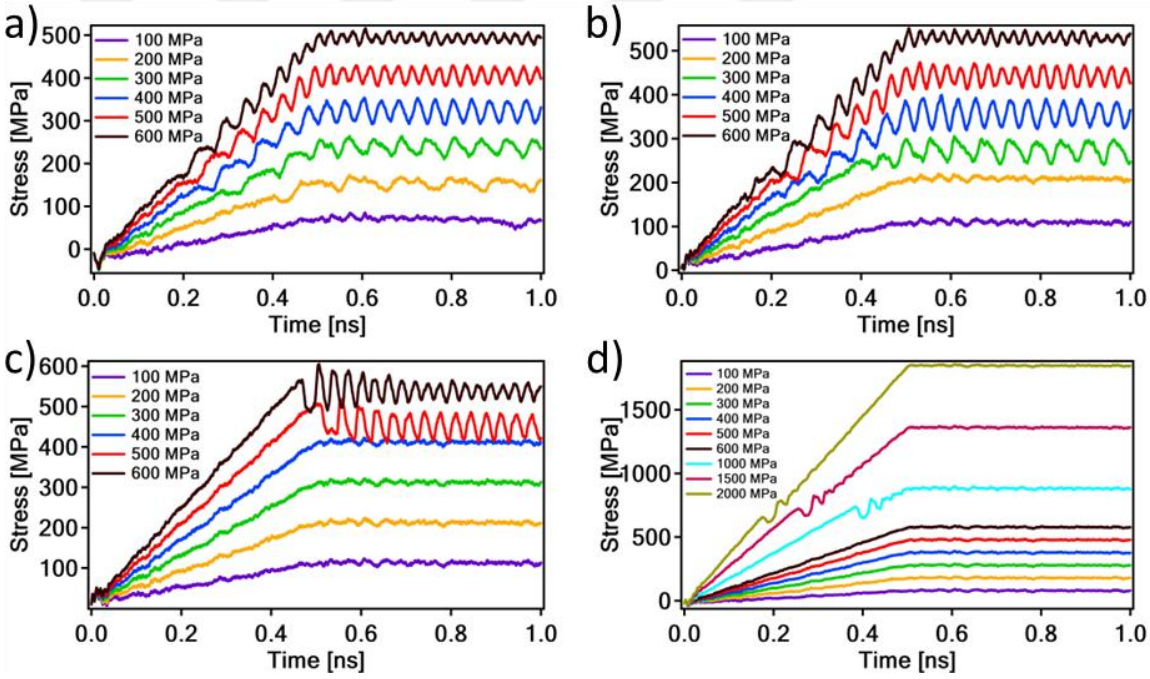

Supplementary Figure 28 Stress versus time graphs at 200K for the {112} plane. Here, a) shows the pure iron case 0% H/Fe, b) shows 0.1% H/Fe concentration, c) shows 0.25% H/Fe concentration, and d) shows 0.5% H/Fe concentration [120].

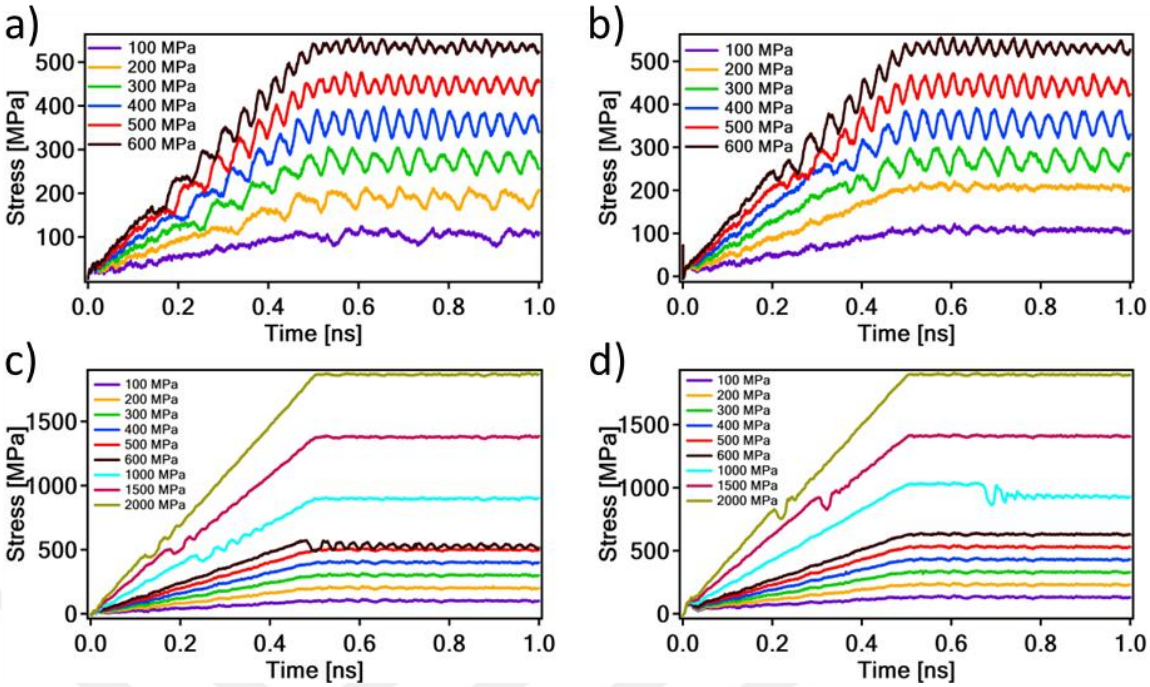

Supplementary Figure 29 Stress versus time graphs at 300K for the {112} plane. Here, a) shows the pure iron case 0% H/Fe, b) shows 0.1% H/Fe concentration, c) shows 0.25% H/Fe concentration, and d) shows 0.5% H/Fe concentration [120].

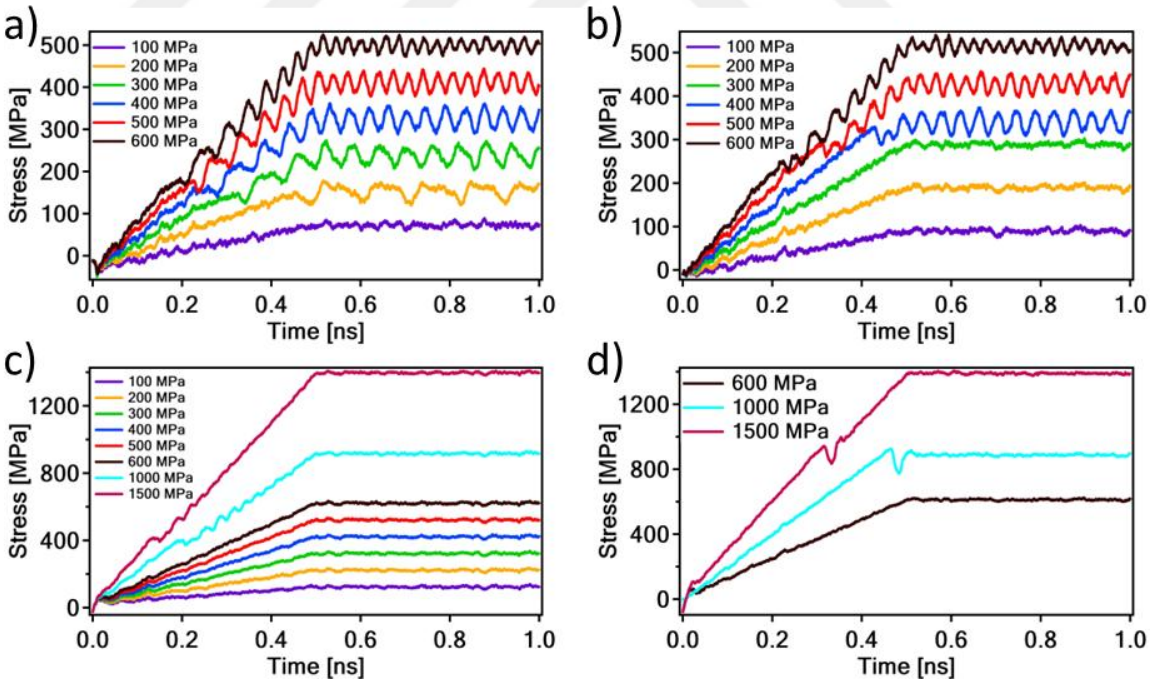

Supplementary Figure 30 Stress vs time graphs of 400K temperature for {112} plane. Here, a) shows the pure iron case (0% H/Fe), b) shows 0.1% H/Fe concentration, c) shows 0.25% H/Fe concentration d) shows 0.5% H/Fe concentration [120].

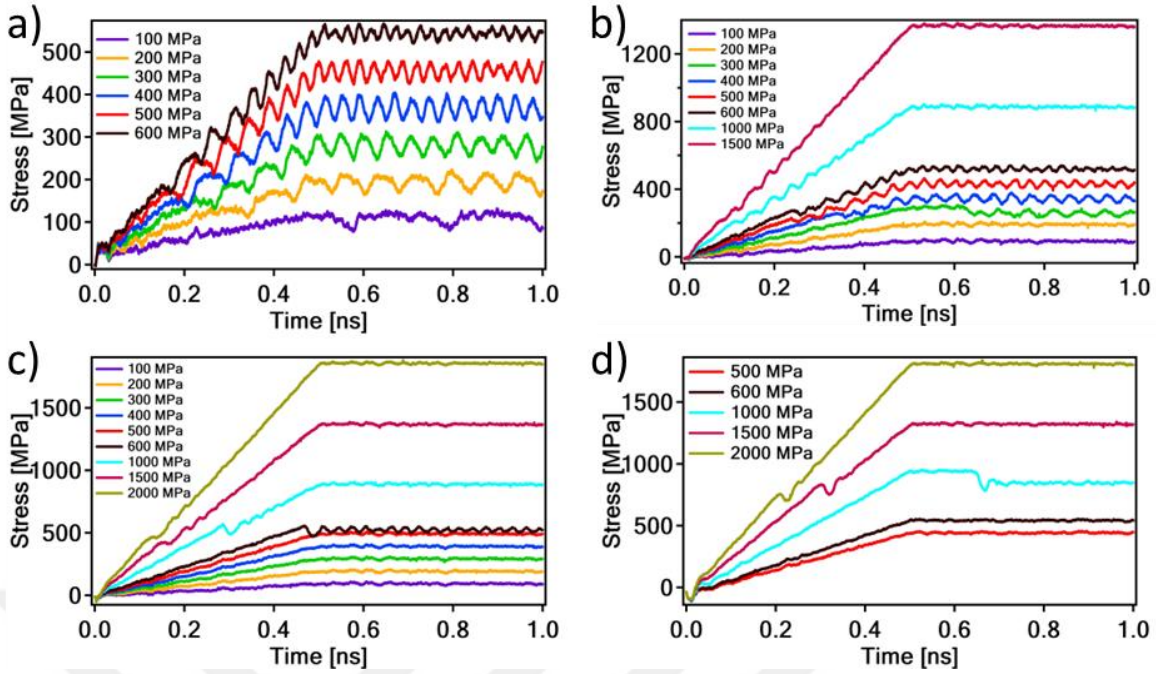

Supplementary Figure 31 Stress vs time graphs of 500K temperature for {112} plane. Here, a) shows the pure iron case (0% H/Fe), b) shows 0.1% H/Fe concentration, c) shows 0.25% H/Fe concentration d) shows 0.5% H/Fe concentration [120].

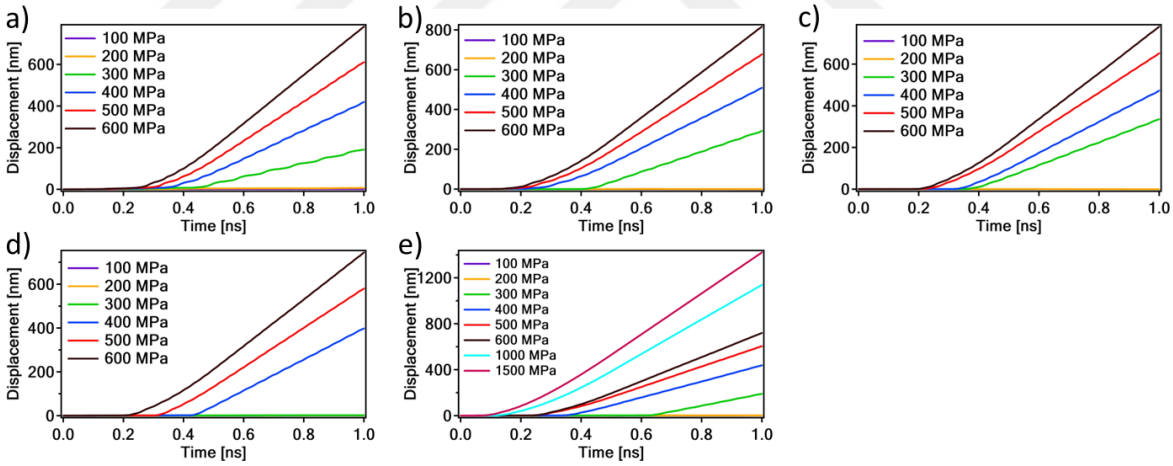

Supplementary Figure 32 Dislocation displacement vs time graph of 0.1% H/Fe concentration cases. Here, from a to e, graphs belong to 100K, 200K, 300K, 400K and 500K temperature values [120].

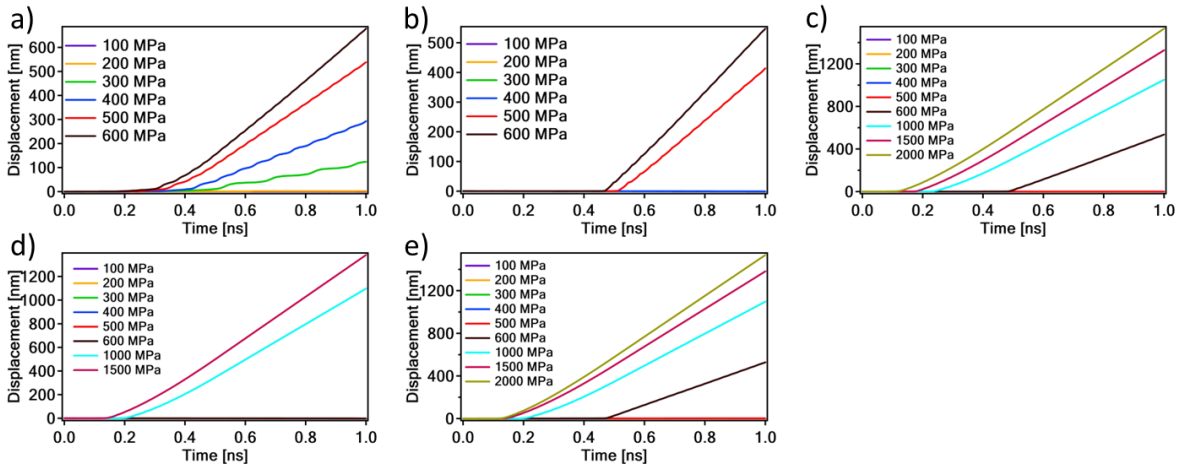

Supplementary Figure 33 Dislocation displacement vs time graph of 0.25% H/Fe concentration cases. Here, from a to e, graphs belong to 100K, 200K, 300K, 400K and 500K temperature values [120].

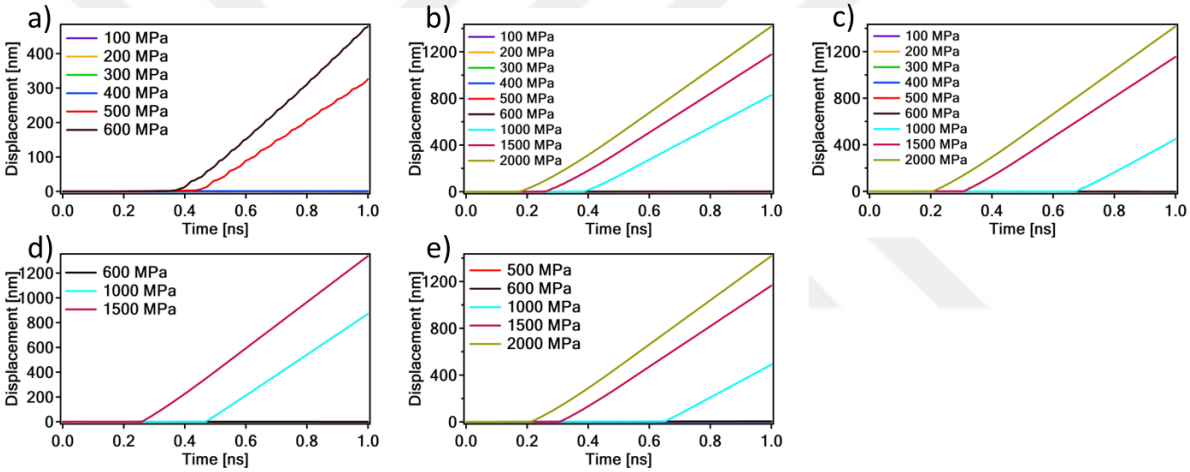

Supplementary Figure 34 Dislocation displacement vs time graph of 0.5% H/Fe concentration cases. Here, from a to e, graphs belong to 100K, 200K, 300K, 400K and 500K temperature values [120].

CURRICULUM VITAE

2008-2013	B.Sc., Mechanical Engineering, Atatürk University, Erzurum, TURKEY
2015-2018	M.Sc., Advanced Materials and Nanotechnology, Abdullah Gül University, Kayseri, TURKEY
2019-2014	Ph.D., Materials Science and Mechanical Engineering, Abdullah Gül University, Kayseri, TURKEY
2015-Present	Research Assistant, Mechanical Engineering, Abdullah Gül University, Kayseri, TURKEY

SELECTED PUBLICATIONS AND PRESENTATIONS

J1) M. F. Baltacioglu, B. Cetin, and B. Bal, "The Effect of Strain Rate on the Hydrogen Embrittlement Susceptibility of Aluminum 7075," J Eng Mater Technol, vol. 145, no. 2, Nov. 2022, doi: 10.1115/1.4056158.

J2) M. F. Baltacioglu et al., "Hydrogen susceptibility of Al 5083 under ultra-high strain rate ballistic loading," vol. 66, no. 10, pp. 1627–1643, 2024, doi: doi:10.1515/mt-2024-0056.

J3) M. F. Baltacioglu, M. F. Kapci, J. C. Schön, J. Marian, and B. Bal, "A phenomenological hydrogen induced edge dislocation mobility law for bcc Fe obtained by molecular dynamics," Int J Hydrogen Energy, vol. 87, pp. 917–927, 2024, doi: https://doi.org/10.1016/j.ijhydene.2024.08.509.

C1) M. F. Baltacıoğlu, B. Bal, How to Increase the Efficiency of Hydrogen Charging Setup, 2nd Latin American International Conference on Natural and Applied Sciences (April, 2022)

C2) M.F. Baltacıoğlu, B. Bal, Incorporating Hydrogen Atoms into Molecular Dynamic Simulation Cell Files, European Conference on Fracture 2024 (August, 2024)